Nanolithography on non-planar surfaces and self-assembly of metal salt-polymer nanomaterials

by

Celal Con

A thesis
presented to the University of Waterloo
in fulfillment of the
thesis requirement for the degree of
Doctor of Philosophy
in
Electrical and Computer Engineering (Nanotechnology)

Waterloo, Ontario, Canada, 2016

Author's Declaration

This thesis consists of material all of which I authored or co-authored: see Statement of Contribution included in the thesis. This is a true copy of the thesis, including any required final revisions, as accepted by my examiners.
I understand that my thesis may be made electronically available to the public.

Statement of Contributions

This thesis contains materials from several published or submitted papers, some of which resulted from collaboration with my colleagues in the group.
For the work on electron beam lithography on irregular surfaces using evaporated resist, covered in Chapter 3, Jian Zhang is the first author of the published paper and my contribution is on resist film preparation and electron beam lithography.

Abstract

This thesis is focused on fabrication of high aspect ratio nanostructures on non-planar surfaces using evaporated electron beam resist (Part I), and a novel fabrication method of high-resolution surface nanostructures using metal salt: polymer nanocomposites self-assembly (Part II).

Various top-down and bottom-up nanopatterning techniques are currently available with the rapid progress in instrumentation and material engineering. However, patterning on non-planar surfaces of various materials still remains an overwhelming challenge because the conventional resist coating method, spin-coating, works well for only planar surfaces such as a flat wafer. On the other hand, the ability to pattern any given surface at the nanoscale, in particular surfaces with high inherent roughness or with pre-patterned micro-scale features, opens new perspectives in various fields from multi-scale biomimetics to optoelectronics. Part I (Chapter 1-4) of the present thesis aims to address this issue using evaporated electron beam resist. Electron beam lithography (EBL) is a versatile technique for creating arbitrary patterns on substrates with sub-10 nm resolution. Contrary to conventional lithography techniques, EBL was previously shown to be able to pattern non-planar surfaces using modified lithography system to adjust the beam position along z-axis, spray coating of the resist, and evaporation of the resist. Among them, evaporation of the resist is more favorable as it can be done on any irregular surface using commonly available thermal evaporation equipment. Yet, previous evaporated resist materials suffer from low resolution and sensitivity, as well as poor dry etching resists for subsequent pattern transfer to the sub-layer. Here, evaporation of polystyrene electron beam resist is studied which was used to pattern on irregular surfaces such as the cantilever of atomic force microscope and side surface of an optical fiber. Furthermore, in order to drastically increase the resist's dry

etching resistance, chromium that is a hard etching mask material was successfully incorporated into the resist by co-evaporating or Cr and polystyrene. This nanocomposite resist enabled the fabrication of very high aspect ratio structures by electron beam lithography followed by dry plasma etching. As this material can be evaporated on any substrate, including non-planar surfaces, it can open new era to spectroscopy and bio-sensing techniques.

Part II (Chapter 5-6) presents a low-cost bottom-up fabrication technique for creating dense surface nanostructures without long-range ordering. Recently, micro- and nano-structured surfaces have become a hot topic in nanotechnology where performance of devices is enhanced due to such surface nanostructuring. Such structures are often called "smart" coating on the surfaces where they could provide wetting/de-wetting, adhesion, thermal and/or electrical conductivity, super-hydrophobicity, self-cleaning, anti-icing, anti-reflectivity, etc. Bottom-up techniques, such as self-assembly lithography, are undoubtedly much more cost-effective than top down lithography techniques for applications that do not need long range ordering. Block co-polymer lithography, colloidal lithography, sol-gel processing, wet/dry etching are some commonly used techniques of bottom-up fabrication. However, fabrication of those structures with low costs as well as high performance is still challenging. Here a novel fabrication method is introduced, which involves spin-coating of metal salt: polymer composite followed by its phase-separation upon thermal annealing. Both spin-coating and thermal annealing are very low-cost processes. With this method, after pattern transfer to the substrate using the self-formed metal salt islands as mask, dense and high-resolution nanostructures over large area without long-range ordering is achieved, which offer greatly enhanced super-hydrophobic and anti-reflective properties.

Acknowledgements

It is a great pleasure to thank those who made this thesis possible.

This thesis would not have been possible without the contributions of the following people, all of whom I feel extremely lucky to have had the opportunity to work with:

I would like to thank Professor Bo Cui for supervising my thesis, and his priceless insights into this project.

I owe my deepest gratitude to Professor Bo Cui for his trust, encouragement, helpful advice and valuable discussions. His enthusiasm, immense knowledge and guidance helped me in the research and writing of this thesis. He supported me not only for my study but also for my life, thank you again for being beside me during my hardest times.

I am grateful to Professor Karim Karim, Professor Guo-xing Miao, Professor Boxin Zhao and Professor Jesse Greener for being members of my thesis committee, and for their advice, assistance, and insightful comments and feedback on this thesis.

Special thanks to Dr. Jian Zhang. He was a great friend, and was always willing to help me no matter the time or day of the week. His assistance was priceless when I was in trouble with atomic force microscopy and scanning electron microscopy.

I would like to thank the lab managers in cleanroom and other laboratories that I worked at, Richard Barber, Vito Logiudice, Nathan Nelson Fitzpatrick, Brian Gordon, and Nina Heinig for their friendly support over these years.

I would like to acknowledge the financial support from Ministry of Education of Turkey.

I would also like to thank my friends that worked together with me in cleanroom.

Special thanks to all of our group members, Dr. Ripon Kumar Dey, Ferhat Aydinoglu, Dr. Xiangcheng Sun, Dr. Mehrdad Irannejad, and all other current and past members, for their support and assistance. I will never forget their kindness and enthusiasm towards their research.

I would like to thank to all of my friends that were with me during my study. I am proud to have such wonderful friends beside me; Ali Yurtalan, Ahmet Camlica, thank you for sharing your happiness with me.

A special thanks to my family. Words cannot express how grateful I am to my mother, my father, my sisters and brother for all of the sacrifices that you've made. Your prayer for me was what sustained me thus far.

There is no word to show my love and feelings to my beloved wife, rest in peace, Emel. You are my source of motivation for always giving me strength and hope throughout my life. My love, my world became my heaven with you. I know you have never left me and I always feel your soul beside me.

Finally, I thank my God, Er-Rahman, Er-Rahim, for letting me through all the difficulties. I have experienced Your guidance day after day. You are the one who let me finish my degree. I will keep on trusting You for my future. Thank you.

Dedication

To my family, and to my beloved Emelim

Table of Contents

List of Figures

List of Tables

Part I Top-down fabrication techniques: electron beam lithography

Chapter 1 Introduction to nanofabrication

1.1. Introduction to nanotechnology

Nanotechnology is a range of emerging technologies in which the structure and property of matter are controlled at the nanometer scale, scale of one-billionth of a meter. For instance, when the structure size is smaller than optical wavelength, novel optical properties will appear respectively. For electronic materials, new phenomena such as Coulomb blockade will emerge when the size is small enough for quantum effect to dominate. In biology, for example, DNA will be stretched when passing through a nanoscale fluidic channel. Apparently, one key factor to the fast growth in nanotechnology is the ever-growing capability in nanofabrication techniques. Although the first creator of nanostructures is nature itself, the history of nanofabrication starts with the famous talk given by Richard Feynman in 1959 entitled "There is plenty of room at the bottom: an invitation to enter a new field of physics" at the annual meeting of the American Physical Society at the California Institute of Technology (Caltech).[1] With his visionary talk, he brought all attention to a large spectrum of the fields of nanotechnology in which physical and chemical properties of elements will be different than the microscale. And now, with the advancements in nanotechnology which uses well-established techniques of fabrication, we are able to not only mimic nature for anti-reflecting, self-cleaning, self-healing, etc., but also to detect the cells for cancer detection, single photons, or detect single atom by using microelectromechanical systems (MEMs), and so on.

1.2. Introduction to nanofabrication

Nanofabrication is a technology for producing nanoscale structures with dimensions lower than 100 nm. From microfabrication to nanofabrication, the technology has been continually pushed by the semiconductor industry. Nanofabrication is vital to all nanotechnology fields, especially for the realization of nanotechnology involving traditional areas across engineering and science. Known as Moore's Law, the statement of doubling the number of transistors on ICs in every 18 months is a conclusion from the advancements and achievements in the technology. With the invention of deep-UV lithography, critical dimension of ICs was down to 500 nm from 1 μm in 1982, and sub-100 nm in early 2000s, and now it is announced as 14 nm.[2]

Many of the devices and systems used in modern industry are becoming progressively smaller and have reached the nanoscale domain. Nanofabrication aims at building nanoscale structures, which can act as components, devices, or systems, in large quantities at potentially low costs.

While semiconductor industry used the improvements and developments in lithography techniques such as deep-UV lithography, various new nanofabrication techniques are being developed recently. Such techniques are used to fabricate the nanostructures and nano-devices to map the body, to mimic nature, to detect light, to clean water, and to store energy, etc. Broadly speaking, there are two types of nanofabrication techniques, namely bottom-up and top-down (as shown in Figure 1.1). Bottom-up (Figure 1.1a and b) is mainly focused on developing materials in the form of particles and molecules, films and tubes or molecular devices. For this purpose, chemical synthesis, self-assembly of blocks into ordered array of structures such as nano-sphere lithography, self-assembly of block copolymers, etc. are the methods that have been used. Top-down fabrication methods (Figure 1.c), in other words, top-down lithography technique, is the

process that involves nanolithography such as photolithography, electron beam lithography, nanoimprint lithography, and thin film deposition and etching.

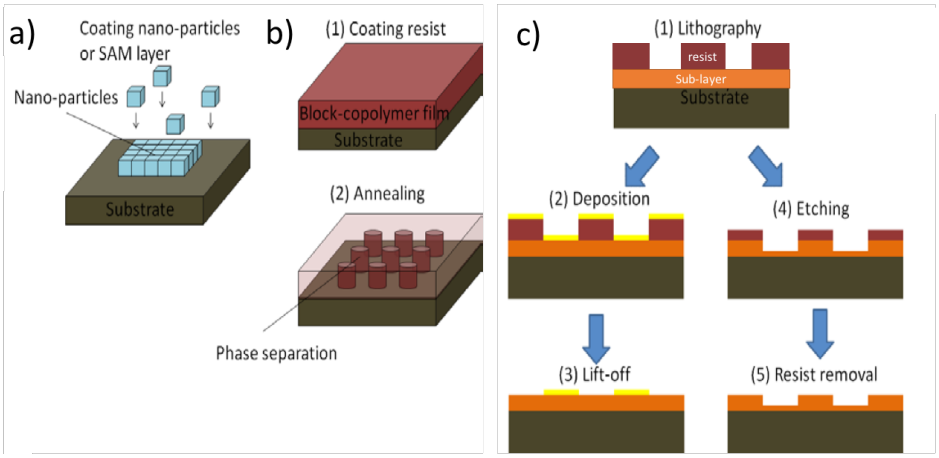

Figure 1.1. Schematic diagram of (a)&(b) bottom-up the and (c) the top-down approaches. In the bottom-up approaches, method (a) is coating synthesized nano-particles or self-assembled mono layer (SAM) layer; (b) is block-copolymer self-assembly lithography. In the top-down approaches, (1) the resist is patterned by lithography, and then the pattern is transferred by (2) deposition followed by (3) liftoff, or the pattern is transferred by (4)&(5) direct etch.

1.3 Thesis outline

In the first part of this thesis, several nanofabrication techniques, mainly electron beam lithography, were investigated, and new strategies were developed for the fabrication process and for patterning on non-planar surfaces. Chapter 2 describes the literature review on lithography techniques, and Chapter 3 and Chapter 4 explore nanofabrication techniques for non-planar surfaces with high aspect ratio structures using electron beam lithography. In the second part, fabrication of high-resolution nanostructures, for use as anti-reflective/hydrophobic coatings by self-assembly techniques, are discussed. Low-cost fabrication method and properties of dense nanostructures without long-range ordering are discussed in Chapter 5, and high resolution surface nanostructures using phase separation of polymer and metal salts are discussed in Chapter 6.

Chapter 2 Top-down fabrication techniques: Electron beam lithography

2.1. Overview of nanolithography

Lithography has its roots in ancient times. In Greek language, *lithos* means stones and *graphia* means to write. Literally it means writing on stone, whereas in semiconductor lithography the stones are silicon wafers and writing is done by advanced fabrication tools. It is critical that design and fabrication of structures and devices at nanometer scale are the key factors for the applications in nanotechnology. Since the booming of nanolithography in 1990s, numerous nanolithography techniques have been developed not only to control the size and geometry of these structures for proposed applications but also to reduce the cost of fabrication process.[3] In lithography, the most important parameter is to achieve highest resolution, which means to be capable of producing smallest dimension patterning. Bottom-up lithography techniques are more favorable than top-down techniques when considering the cost of fabrication. These techniques can be listed as self-assembly of nanostructures, nano-sphere lithography, colloidal lithography, block co-polymer lithography, and template-based methods that exploit nanoporous membranes.[4,5,6,7,8,9] However, these techniques can only produce periodic structure without long range ordering. Top-down techniques such as photolithography, electron beam lithography, and nanoimprint lithography are popular with periodic patterning with high resolution as well as arbitrary structures. Among them, electron beam lithography is the most popular top-down fabrication technique for R&D because it is capable of high resolution and can work with a variety of materials for creating almost infinite number of structures with arbitrary pattern.[10] In

this chapter, top-down lithography techniques, specifically electron beam lithography, will be discussed.

2.2. Top-down lithography techniques

2.2.1. Introduction

Top-down lithography techniques can be divided into two categories: the ones using pre-designed and fabricated mask for pattern duplication, and the ones with direct write on resists for pattern creation. The first type uses the pre-designed and fabricated mask with nanostructures and duplicates these structures onto materials, which are mostly resists. Optical lithography, charged particle projection lithography, x-ray lithography, extreme ultra-violet lithography, and nanoimprint lithography are examples of these techniques that duplicate the structures on the mask or mold onto resist to the substrate. The second type of top-down technique is a direct patterning technique that generates pattern on substrate or resists, including electron beam lithography, focused ion beam lithography, helium ion beam lithography, scanning probe lithography, etc.[7,11,12]

2.2.2. Optical lithography

Optical lithography, or photolithography, schematic in Figure 2.1, is extensively used for fabricating integrated circuits in the semiconductor industry. It is the most widespread top-down fabrication technique because of its high yield, high throughput and low operating costs when implemented for large scale industrial applications.[13,14] In this technique, the pattern from the mask is transferred to a photoresist by ultraviolet light exposure where unmasked area is exposed.[15] A photomask is an opaque plate (usually made from fused silica) with sub-micron sized structures made with chrome metal-absorbing film that allows the light to shine through in a defined pattern. Generally speaking, these masks are used for photolithography purposes with

wavelengths of 436 nm (g-line), 405 nm (h-line), 365 nm (i-line), 248 nm (deep UV) and 193 nm (deep UV). For shorter wavelengths such as 13.5 nm (extreme UV light) that result in higher resolution, entirely new materials such as Si/Mo thin film substrate are used as a reflective mask. In photolithography, chemicals called photoresists are used as a pre-patterning layer on the substrate. These photoresists are categorized as positive and negative tone resists. For positive resists, the resist is exposed to UV light wherever the underlying material is to be removed. In this type of resists, exposure to the UV light changes the chemical structure of the resist so that it becomes more soluble in the developer. In negative type photoresist, this exposure causes the resist to become polymerized and hence difficult to dissolve in the developer solvent. Hence, the resist is exposed to UV light wherever the underlying material is to be kept.

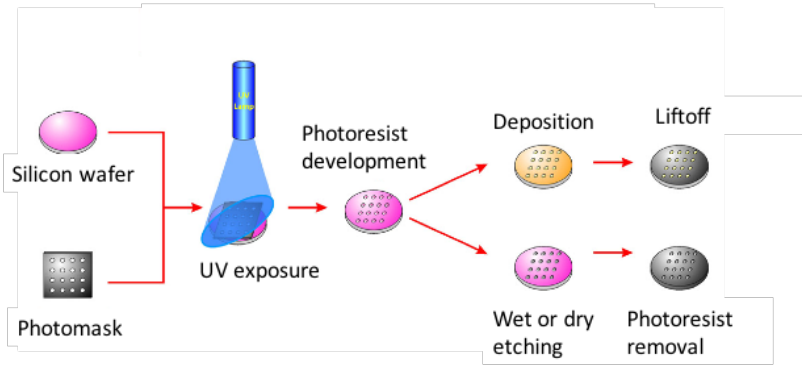

Figure 2.1. Schematic representation of the photolithography process with two potential pattern transfer paths using either deposited or etched features.[13]

After exposing the photoresist, development of the resist is carried out using solvent that will reveal the photoresist pattern on the substrate. Then, the pattern is transferred to the substrate by different etching (e.g. wet chemical etching, dry etching, reactive ion etching, etc.) or deposition (e.g. evaporation, sputtering, electro- chemical deposition, etc.) processes. Resolution of optical lithography is determined by the wavelength of the light (i.e. source), its intensity, time and type of exposure (i.e. projection or contact mode) and the etching method. In photolithography, the

resolution is defined as $R = k_1.\lambda/NA$ where k_1 is a constant number depending on the resist material, λ is radiation wavelength, and NA is the numerical aperture of the optical system. Limitation of photolithography can be due to diffraction of the light. That is once the light passes through the single slit, it diffracts into many directions where constructive/destructive interferences occur and hence exposes on the substrate. One way to decrease this limitation is to use different (smaller) wavelength source of light or use a different lens having smaller diffraction. Recently, to be able to increase the resolution from 100s nm to 10s nm, light source of ArF excimer laser (wavelength of 193 nm) is embedded in the lithography system. It is also called deep-UV lithography due to shorter wavelength. While resolution is comparable with wavelength size in larger wavelength sources, within excimer laser it is less than wavelength as this source k_1 values is smaller than others. Through the combination of other resolution enhancement techniques such as immersion lithography, optical proximity correction, off-axis illumination, phase-shift mask, and double processing, the resolution is enhanced to sub-10 nm scale.[16] In immersion technique, the lithography is done in environment such that refractive index (n) of it is higher than air, water for instance where n is 1.44 where in this case NA is increased and hence smaller features can be achieved. This is because in a dense environment more light can be collected and hence more light can be focused at certain point with less diffraction. This technique is further improved and now 13.5 nm wavelength source can be used in industrial applications where entirely new materials such as Si/Mo thin film substrate are used as a reflective mask. Although the state of art is 14 nm node (14 nm resolution transistor), fabrication cost became a serious issue, with an industrial EUV lithography system costing up to $50M USD.[2,13] These high costs exclude many universities and world-wide companies from using those state-of-art optical lithography systems.

2.2.3. X-ray lithography

X-ray lithography (XRL), schematically represented in Figure 2.2, where the source with 0.1 nm (called 'hard' X-rays) to 10 nm (called 'soft' X-rays) wavelength is used to expose the resist, is another manufacturing process in which patterning is done using synchrotron radiation through an x-ray mask.[17] X-rays are very energetic waves and they cannot be reflected/refracted similar to UV- and visible light but reflected off smooth metallic surfaces at very shallow angles. In principle, XRL is not as complex as optical lithography, as there are no x-ray optics because of absence of a material that can refract the x-rays.

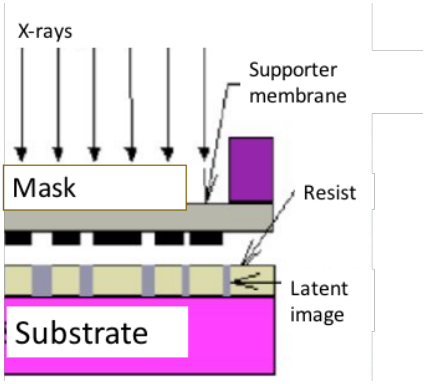

Figure 2.2. Schematic representation of the X-ray lithography.[17]

XRL has two main components: x-ray source and the mask which is used to absorb the x-rays. For XRL, the mask has to be fabricated using materials that can absorb x-rays, and it is typically gold supported by thin membranes made of silicon nitride, titanium, or graphite.[18,19] The source wavelength spans from 1 nm ('soft' x-rays) to 0.1 nm ('hard' x-rays) where resolution is limited by Fresnel diffraction and secondary electrons generated in the resist. Although very fine features with vertical sidewalls can be fabricated by XRL, fabrication and maintenance of x-ray mask is a serious issue because the thin membrane is very fragile. Local stress caused by heavy

absorption and internal stress of the membrane can also affect the resolution of the pattern. Furthermore, x-ray source has to be strong and collimated synchrotron radiation source. The cost of setting up and maintaining the X-ray light source is extremely high which affects its popularity.

2.2.4. Interference lithography

Interference lithography (IL) is a parallel patterning method for which a minimum of two coherent laser beams are used to create the interference pattern on the resist film.[13,20,21] When two laser beams from the same source coincide, an interference pattern is created as illustrated in Figure 2.3. It is a promising top-down lithography technique with high-throughput and well-defined features at nanoscale.[13] The period of the resulting periodic structure is given by:

$$\Lambda = \frac{\lambda}{\sin(\theta_1)+\sin(\theta_2)} \tag{2.1}$$

where Λ is periodicity, λ is wavelength of two coherent light waves, θ_1 and θ_2 are the angles between the normal of the exposed surface and the beams 1 and 2. The idea is, creating constant phase difference between two waves and hence the two laser beams will only interfere over a distance.

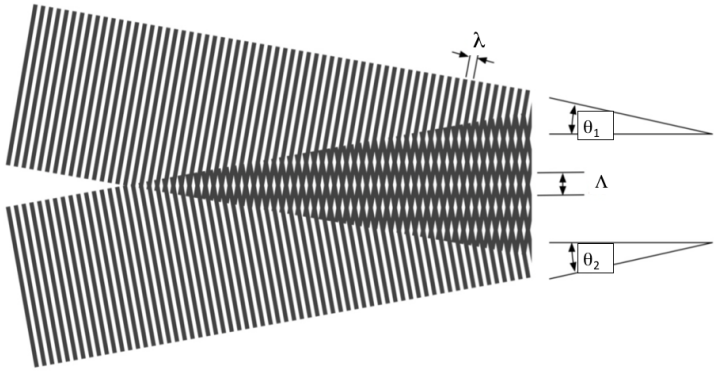

Figure 2.3. Schematic representation of the interference lithography setup with two coherent laser beams.

The intensity of the grating is sinusoidal and can be used for different applications such as creating hole array, grating array, etc. Currently, IL is extensively used in industry to fabricate diffraction gratings, field-emission displays, nano-imprint lithography molds, etc. due to its affordable prices (around $50 K USD).[13,20] However, major drawback of IL is that it can only be used to fabricate periodic structures and not suitable for arbitrary designs.[20]

2.2.5. Nanoimprint lithography

Instead of creating a pattern by masking and exposure, nanoimprint lithography (NIL) is a method for fabricating micro-nano structures with low cost, high throughput and high resolution.[22] Compared with other aforementioned lithography techniques, the most prominent advantage of NIL is its ability to pattern 3D and large-area structures with low cost.[22]

NIL is capable of sub-10 nm resolution.[22,23,24] NIL is based on the principle of mechanical modification of a thin polymer film by thermo-mechanical or UV curing process using a mold which contains nanopatterns (shown in Figure 2.4). Hence, unlike optical lithography technique, NIL does not require expensive and complex optics. As it is the duplication of the nanopatterns on the mold to the substrate, the resolution of NIL is limited by the mold used in the process

itself and hence it is beyond the limitations set by light diffractions, which makes it a popular technique to apply in many areas such as nano-electronics, nano-optoelectronics, data storage, electromechanical systems (MEMS/NEMS), LEDs (light emitting diodes), quantum electronic devices, photodetectors, optical and biological devices.[25,26,27,28,29,30]

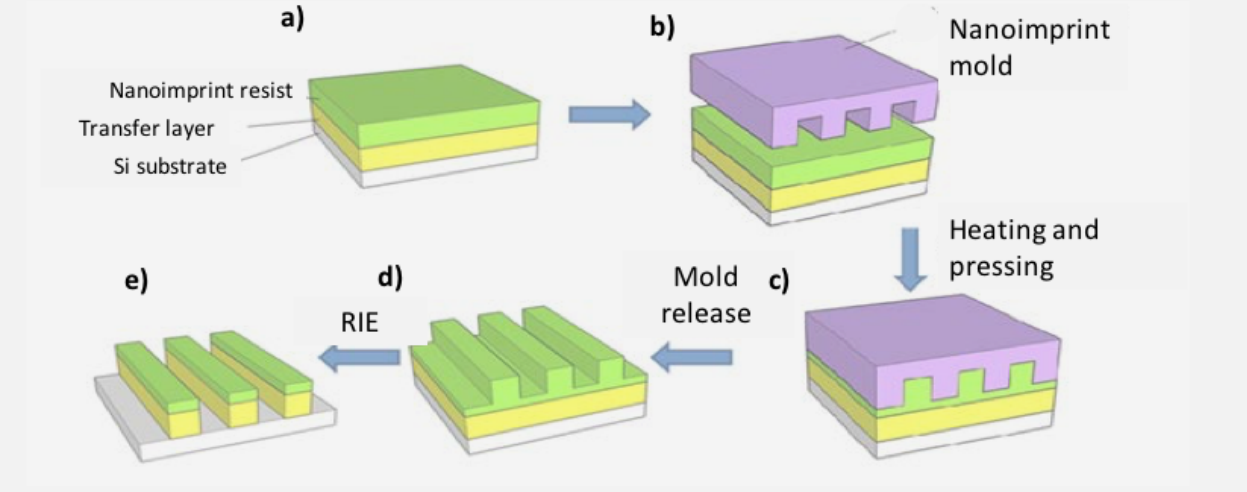

Figure 2.4. Schematic representation of the nanoimprint lithography process. a) Nanoimprint resist is coated on top of substrate coated with transfer layer; b) imprint mold with sub-micron sized features is brought to contact with the sample; c) subsequent heat and mechanical force is applied to get the reverse-structures on the resist; d) upon releasing the mold, reverse-pattern is obtained on the resist; e) by proper reactive ion etching, this pattern is transferred onto transfer layer and hence the substrate.

After first demonstration by Stephen Chou in 1995,[31] there have been great efforts to achieve sub-10 nm resolution on large area quickly and cost-effectively; and now there are varieties of NIL process types such as laser assisted NIL, step-and-flash NIL, roll-to-roll NIL, etc. As its resolution is limited by the mold, it is also the major drawback since the mold has to be fabricated using other lithography techniques such as interference lithography and electron beam lithography. Also, the mold is usually made from silicon, SiO_2, diamond, quartz or metals due to

their hardness.[32] As they are brittle and thus hard to use for many times, there are polymeric materials used for mold which are called soft materials, and the technique is generally called soft lithography. Such materials include Polydimethylsiloxane (PDMS), Polyvinyl chloride (PVC), Polyvinyl alcohol (PVA), Perfluoropolyether (PFPE), Ethylene tetrafluoroethylene (ETFE), and Teflon AF 2400.[25,33,34] Recently, Con et al. used Fluorolink MD-700 polymer, which is a PFPE-based and Teflon-like polymer, as a mold material for NIL. It is capable of sub-100 nm resolution with higher elastic modulus near the film surface than deep inside the film (300 vs. 50 MPa) that is desirable for an imprint mold.[35]

2.2.6. Scanning probe lithography

Another strategy for fabricating nanostructures using top-down technique is to use small scanning tips/probes to "machine" the surface of the substrates, which is called scanning probe lithography (SPL). Although SPL is a slow process compared to optical lithography, it can generate sub-10 nm resolution features with arbitrary profiles.[14] Its imaging resolution reaches atomic level, and as a patterning tool it depends on the probe that is generally less than 50 nm in size.[13] One fabrication technique using these probes is achieved by moving/scanning the probe wetted by solution containing molecules of the material to be transferred to the substrate, in which any arbitrary structure can be patterned. This technique is known as dip-pen lithography (DPL). This method can also be used to etch metals such as gold, silver and palladium.[13]

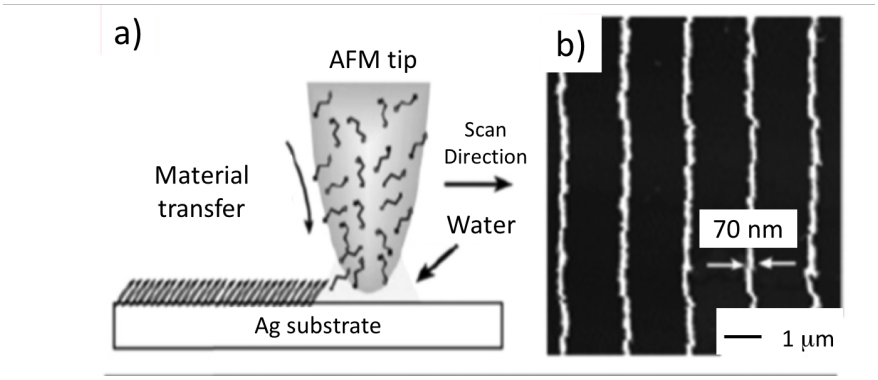

Figure 2.5. Schematic diagram and image of scanning probe lithography approach: a) AFM nanolithography by deposition of SAMs on a silver substrate, b) Direct deposition of SAMs of 16- mercaptohexadecanoic acid by an AFM tip on a silver substrate.[13]

Another technique is the application of the tip to contact physically with the substrate surface to remove the materials or molecules, which is called the force-induced pattern transfer method (Figure 2.5). Patterning self-assembled monolayers (SAMs), polymers and particles are examples of this technique. SPL is atomic level resolution technique along with the ability of creating arbitrary shaped structures, however, SPL is a very slow technique.[36]

2.2.7. Focused ion beam lithography

Focused ion beam (FIB) lithography is one of the top-down fabrication lithography techniques that typically uses Ga^+ ions that can be operated at low beam currents for imaging or high beam currents for site specific sputtering or milling. FIB is capable of patterning directly on the substrate or on the resist to make 3D patterning possible.[37] Unlike other lithography techniques, FIB lithography is a maskless lithography technique, where focused Ga^+ ion beam is scanned over the substrate surface, and hence capable of creating arbitrary shaped structures on the surface. This process is known as milling as it physically removes the material from the substrate

surface (Figure 2.6a). It uses high energetic ions rather than photons and electrons, and ions have high momentum, and short wavelengths thus without any diffraction limitations ($\lambda=h/p$).

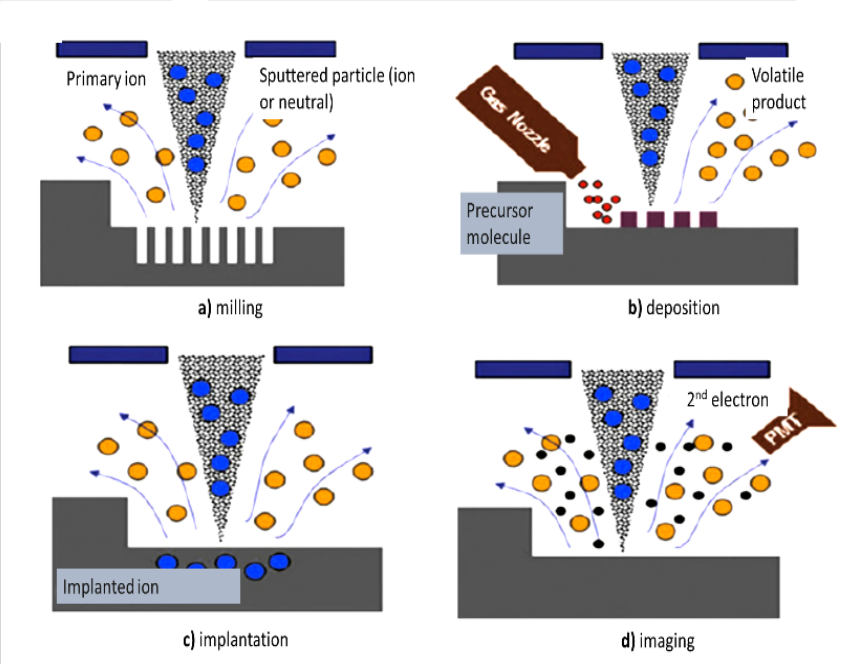

Figure 2.6. Basic four functions of FIB processing: (a) milling, (b) deposition, (c) implantation and (d) imaging.[37]

Besides physical sputtering (Figure 2.6a), FIB is capable of depositing materials (i.e. additive lithography) using gases (Figure 2.6b), implanting ions (Figure 2.6c) for fabrication of etching masks and directly modifying materials by ion-induced mixing. Yet it is an expensive and slow process compared with the optical lithography techniques though it offers sub-10 nm resolution.[38]

Ga^+ are more favorable than other ionic sources for FIB ion source due to its low melting point, low volatility, low vapor pressure, excellent mechanical, electrical and vacuum properties, where its emission characteristics enable high angular intensity with a small energy spread. However, the major drawback of Ga^+ ions is that due to their mass, ions can displace and scatter atoms in

the substrate and hence reduce the performance. Microscopes with noble gases are now replacing Ga^+ FIB systems as they are lighter than Ga^+ ions but heavier than electrons and hence creating less damage on the substrate.[38] The first commercial helium ion microscope was introduced in 2006,[39] and by now it has reached a maturity such that resolution of 5 nm features has been reported.[40,41]

2.3. Electron beam lithography

2.3.1. Definition and historical perspective

Electron beam lithography (EBL) has its roots in scanning electron microscopy (SEM) which was first developed in late 1960s.[42] EBL is the main direct writing technique which provides sub-10 nm resolution due to the small wavelength, and can work with a variety of materials.[43] EBL, with the ability to form arbitrary two dimensional patterns, is a maskless lithography technique that uses highly focused electron beam to modify the radiation sensitive materials' property to make it soluble/insoluble during a subsequent development step, see Figure 2.7.

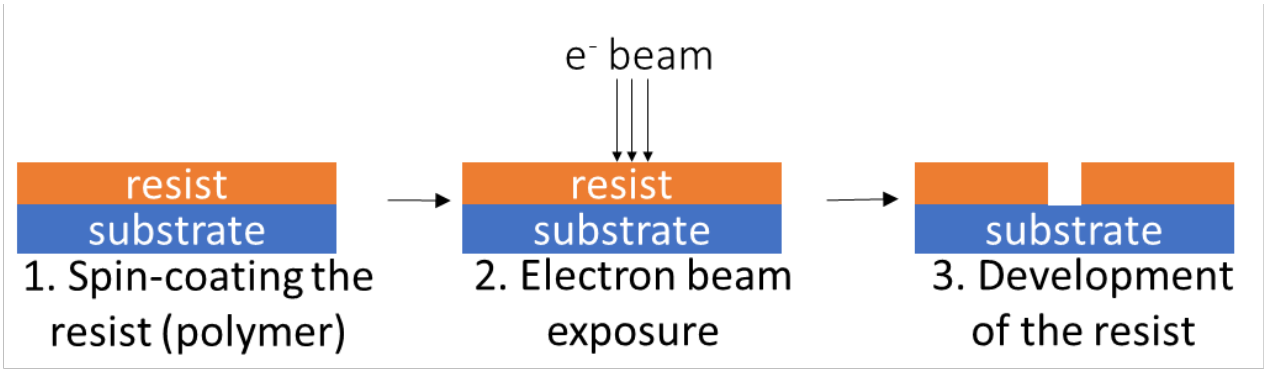

Figure 2.7. Representation of electron beam lithography process: spin coating the resist, electron beam exposure, and development of the resist.

EBL has three main steps, which are spin coating of the radiation sensitive material (resist),

exposure of the resist by electrons, and development of the resist. The pattern transfer should not be considered independently as the final resolution and the quality of the pattern is a result of the combination of each process. The first popular electron-beam (e-beam) sensitive material is known as polymethylmethacrylate (PMMA) which was developed in 1960s, that is earlier than the development of optical lithography. As EBL system uses SEM where electron optics enable fine beam focusing, using PMMA for EBL demonstrated much higher resolution capability at that time, and during 1970s the resolution capability was down to sub-60 nm.[44]

The main features of the EBL are:

1. Capable of high resolution, down to 2.5 nm,[18] high pattern density, and high reliability,
2. Capable of generating arbitrary patterns and ability and applicable to a variety of materials,
3. Slow writing technique for volume production,
4. Expensive and complex system requirements.[10]

In this part of my thesis, e-beam resists and fabrication of nanostructures on non-planar surfaces using EBL will be discussed after introducing the principles and elements of EBL system.

2.3.2. Electron Optics

The power of EBL system that has high resolution capability at nanometer scale arises from short wavelength of electrons. The de Broglie wavelength of the electrons λ_e can be expressed as

$$\lambda_e = \frac{h}{p} = \frac{h}{\sqrt{2mE}} = \frac{h}{\sqrt{2meV}} = \frac{1.226}{\sqrt{V}}\ (nm) \qquad (2.2)$$

where h is the Planck's constant (4.135×10^{-15} eV.s), p is the momentum of the electron, m is the mass of the electron, e is the charge of the electron, E is the energy of the electron, and V is the

acceleration voltage. For instance, if an electron is accelerated with 10 keV, then the wavelength of the e-beam will be 0.012 nm, which is a huge advantage over optical lithography where the wavelength of the light is much larger. Knowing that current state of art EBL is operating at higher voltages (100 keV), the diffraction limited resolution can be, in principle, at atomic scale. Yet, most high-resolution EBL has a resolution limited by the beam spot size because diffraction of electrons increases the spot size and hence the resolution.

2.3.3. Instrumentation

Figure 2.8 depicts the direct EBL system which was originally developed using SEM by inserting pattern generator and beam blanker to the system. A modern dedicated EBL tool employs high brightness electron sources for higher throughput and high-resolution mechanical stages for exposure of large substrates.

EBL system consists of three parts: lithography control system notably pattern generator/design and operator software, electron optics control system including electron gun and column, and the chamber where the exposure takes place at high vacuum.[14,45] In this section, electron optics system will be discussed.

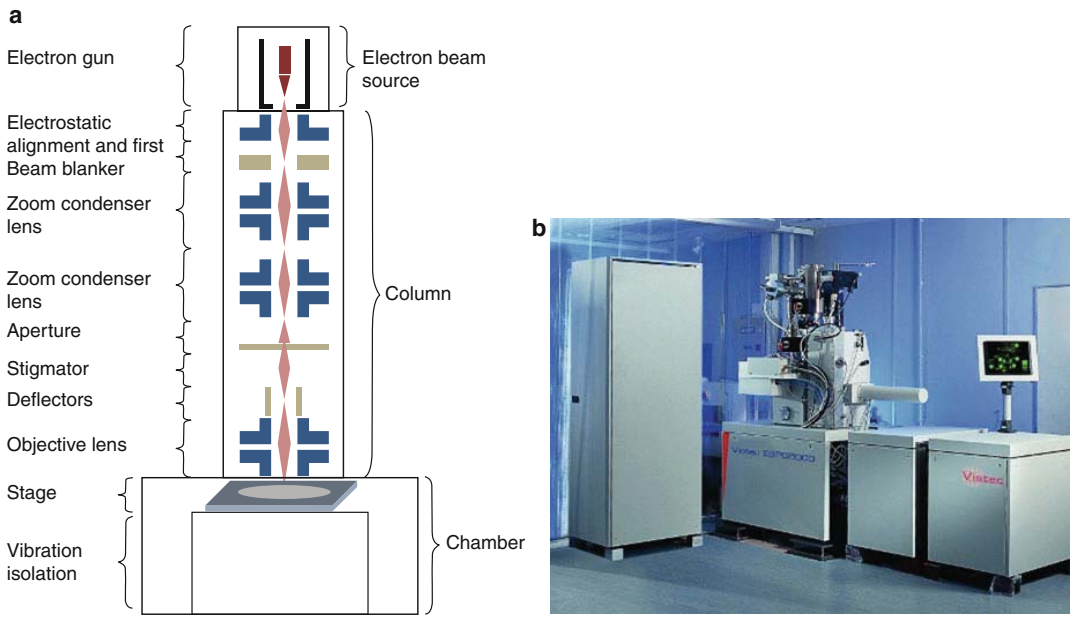

Figure 2.8. (a) Schematic of a typical electron beam lithography system. (b) A typical EBL system (Courtesy of Vistec Electron Beam Lithography Group).[45]

2.3.3.1. Electron gun

Electron gun, or the electron source, is the most essential part of the system as it is the place where the electrons are generated by either heating the cathode, called thermionic emission, or by applying a large electric field, called cold field emission; or sometimes the combination of two field-assisted thermal emission, commonly called Schottky emission.

Important features of the beam source include high intensity, high uniformity and durability, small spot size, and long life. Spot size for most EBL sources is less than 10 nm while this number is 500 nm for light sources for photolithography. Brightness is a measure of the current emitted per unit area per solid angle, equivalent to intensity in optics. Higher brightness is desired to have shorter exposure time and higher throughput.

Some of the materials for these emissions are given in Table 2.1[14] with their brightness and operating conditions and specific parameters.

Table 2.1. Characteristics of different types of filaments.[14]

Source type	Material	Brightness (A/cm^2rad)	Source size	Energy dispersion (eV)	Vacuum level (Torr)	Emitter Temp. (K)
Tungsten Thermionic	W	~ 10^5	25 μm	2-3	10^{-6}	~3000
LaB, Thermionic	LaB_6	~ 10^6	10 μm	2-3	10^{-8}	~2000-3000
Thermal field aided emission (Schottky)	Zr/O/W	~ 10^8	20 nm	0.9	10^{-9}	~1800
Cold field emission	W	~ 10^9	5 nm	0.22	10^{-10}	Ambience

In thermionic emission sources, the filament is heated by passing current through it and electrons are emitted thermionically from a sharp tip. Sharp tips are required in order to provide the extremely high fields necessary for electron extraction from the tip apex. One popular material for thermionic emission source is tungsten (W). However, its low current density results in low brightness ($2x10^4$ A/cm^2rad). Another disadvantage of these filaments is their high operating temperatures which needs high energy. Beside tungsten-based filaments, Lanthanum hexaboride (LaB_6) is another source which can achieve higher current density (over 20 mA/cm^2), resulting in higher brightness. It can also work at lower temperature (2000 K), yet it requires high vacuum (10^{-8} Torr). The major problem with the thermionic sources is the large beam crossover size (10-25 μm). This is because small beam size is preferable for high resolution SEM, as less demagnification is needed to attain a given probe size.

Field emission sources, or cold field emission sources, operate at room temperature. In this type of guns, electrons are tunneled out from the tungsten tip due to high electric field obtained using a very sharp tip (100 nm) and high voltage (Figure 2.9).

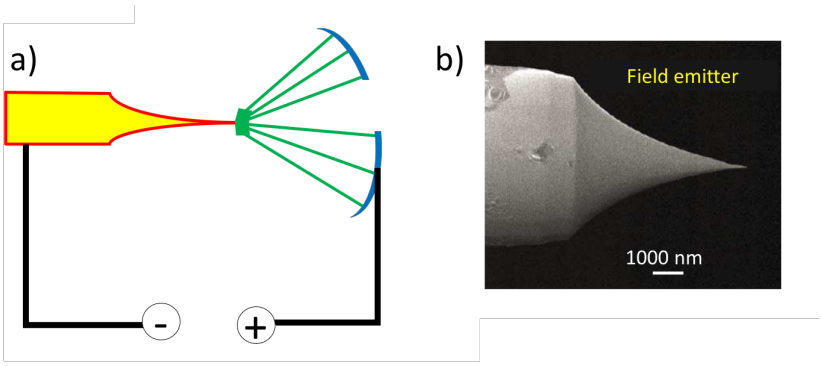

Figure 2.9. Field emission gun: a) representation of emitting from the gun; b) SEM image of field emitter made from tungsten where tip apex size is 100 nm.

Current density of the emitted electrons is independent of the tip temperature since it is a tunneling process of electrons pulled out by the electric field. Small beam spot size (2 nm) can be achieved by field emission gun which gives higher brightness (10^9 A/cm^{2}rad) and hence better performance for focusing on the material. However, it is not a suitable gun for EBL since there is a short-term noise at the beam while contamination gas molecules are randomly absorbing-adsorbing onto the tip during the emission process. This problem can be partially overcome by using ultra-high vacuum systems.

Field assisted thermionics emission (Schottky) sources are the best sources for EBL systems as they provide higher current density and stability. Operating at lower temperature (1800 K), it has longer lifetime than thermionic sources. W/ZrO type tip gives spot size around 2 nm and hence results in better performance with high brightness. One drawback is that they require constant operating vacuum level (10^{-8} Torr) yet it is achievable with present systems.

2.3.3.2. Beam shaping column

The part that gives shape to the electron beam is referred to as the beam column. Beam column has components such as column lenses, apertures, beam deflectors and beam blanker, stigmator, and objective lenses.

Electrons can be focused either by electrostatic forces or magnetic forces, meaning that electrostatic or magnetic lenses can be used in EBL system. However, magnetic lenses are preferable since there is less aberration. A magnetic lens is formed from two circularly symmetric iron pole-pieces that can converge the beam in a magnetic field. In EBL system, normally there are four magnetic lenses. Figure 2.10 below shows a cross-section of a typical magnetic lens, along with some magnetic flux lines.[46]

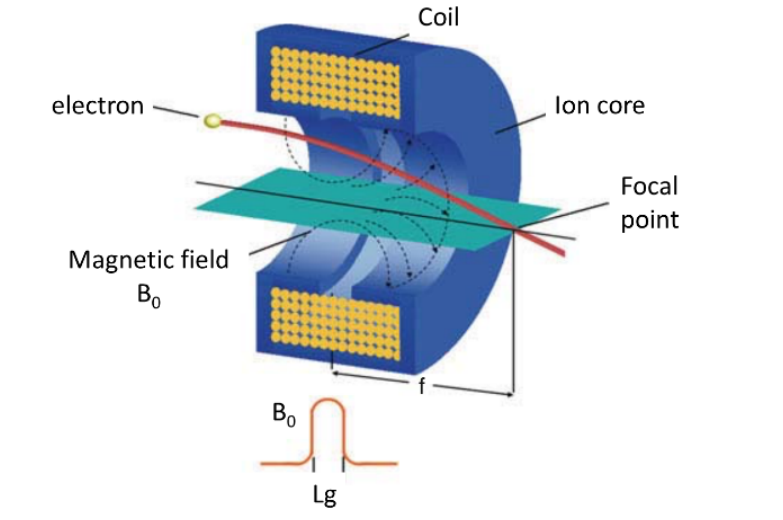

Figure 2.10. Cross-sectional view of a magnetic electron lens.[46]

The radial magnetic field causes electrons to experience rotation about the optical axis upon entering the lens and have a velocity in tangential component. This component interacts with the axial magnetic field, conveying a force on the electrons toward the optical axis, and bringing them close to the axis.

Beam deflectors are responsible for scanning the electron beam over the specimen within the scan field. It can be done by electric or magnetic field and has to be linear deflection in order to precisely pattern ultra-small features. Yet, problems in the linearity of the deflection can be fixed

by the software. Within the column, there are also types of apertures, such as blanking and beam-limiting apertures. The former deflects the beam away from the aperture hole, turning beam on and off; while the latter sets the beam at a convergence angle which controls the effect of lens aberrations and resolution as well as beam current. A typical beam blanker works by applying a voltage to the upper plate of the blanker, which will deflect the electron beam away from the center of the column.

Stigmator is another component of the column that has a critical role in beam shaping.[25] There is astigmatism because of the imperfections of the lenses. These imperfections come from the fabrication and assembly of the lenses which causes imperfectly shaped e-beam. Hence, it affects the lithography where the pattern to be transferred is distorted from the original design. An example of imaging with/without stigmation is shown in Figure 2.11. The stigmator lens has four or eight poles that surround the optical axis to adjust the beam shape to be circular again.

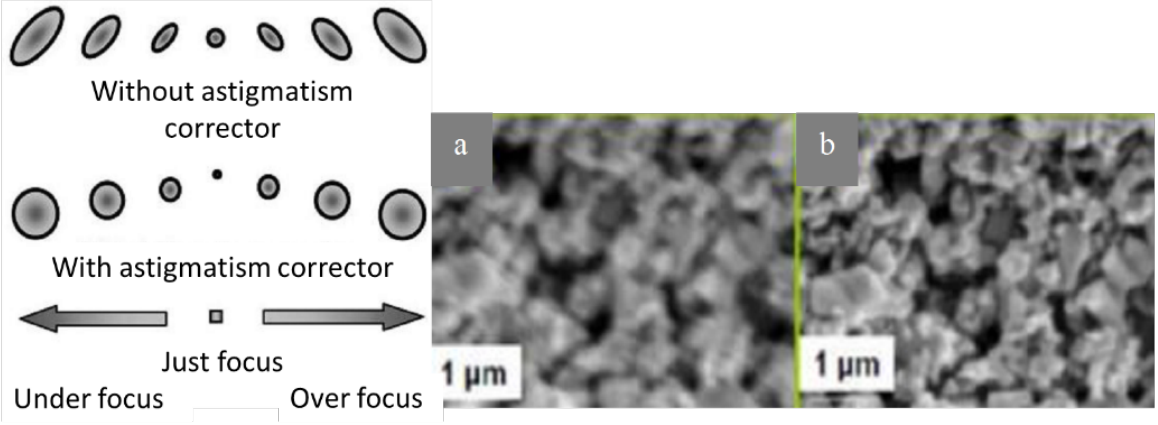

Figure 2.11. Comparisons of beam-forms on the sample and resulted SEM images; a) before stigmation correction, and b) after stigmation correction.[25]

Aberrations, on the other hand, are the result of the converging angle (numerical aperture) of the lenses which are critical for EBL. Spherical aberration occurs when outer zones of the lens focus

more strongly than the inner zones, and chromatic aberrations occur when electrons of slightly different energies get focused at different image planes. These aberrations can be minimized by reducing the convergence angle of the system so that electrons are confined to the center of the lenses.

Theoretically, effective beam spot size can be expressed as the quadratic sum of each contribution including chromatic aberration, spherical aberration, perfect beam diameter if without aberration, and diffraction of the beam, which can be expressed as

$$d^2 = {d_s}^2 + d_c^2 + d_0^2 + d_d^2 \tag{2.3}$$

where d_s is the spherical aberration, d_c is the chromatic aberration due to non-zero energy distribution, d_0 is the perfect beam diameter and d_d is the diffraction limit. In order to get high-resolution patterns for high voltage, low beam current, and small working distance, the beam diameter can be controlled by adjusting the beam current, accelerating voltage, and lens-to-sample spacing and working distance.[47]

2.3.4. Electron-solid interaction and proximity effect

Although electron beam diameter can be in sub-nanometer range, minimum resolution is far away from that value because the energetic electrons undergo interaction with the resist and substrate during exposure. Typically, electron beam lithography systems use 10-100 keV energy per electron, which gives electrons ~10 μm long mean free path that is at least one order of magnitude higher than the typical resist thickness. Hence, the electron beam penetrates into the resist and hits the substrate during exposure, and experiences elastic (results in backward scattering) and inelastic (results in forward scattering) collisions with the resist and the substrate atoms and molecules. Electron trajectories in resist and substrate are modeled by Rutherford

scattering and simulated by Monte Carlo simulation techniques. By Monte Carlo simulation techniques, it can be predicted how deep electrons can go inside the substrate and its relation with the applied voltage. As an example, it is shown in Figure 2.12 with 500 nm thick polystyrene film on silicon substrate.[48] As seen, electron beam with 1 keV energy cannot reach the bottom of the resist while 20 keV penetrates into it and reaches the substrate and scatters along the resist and the substrate.

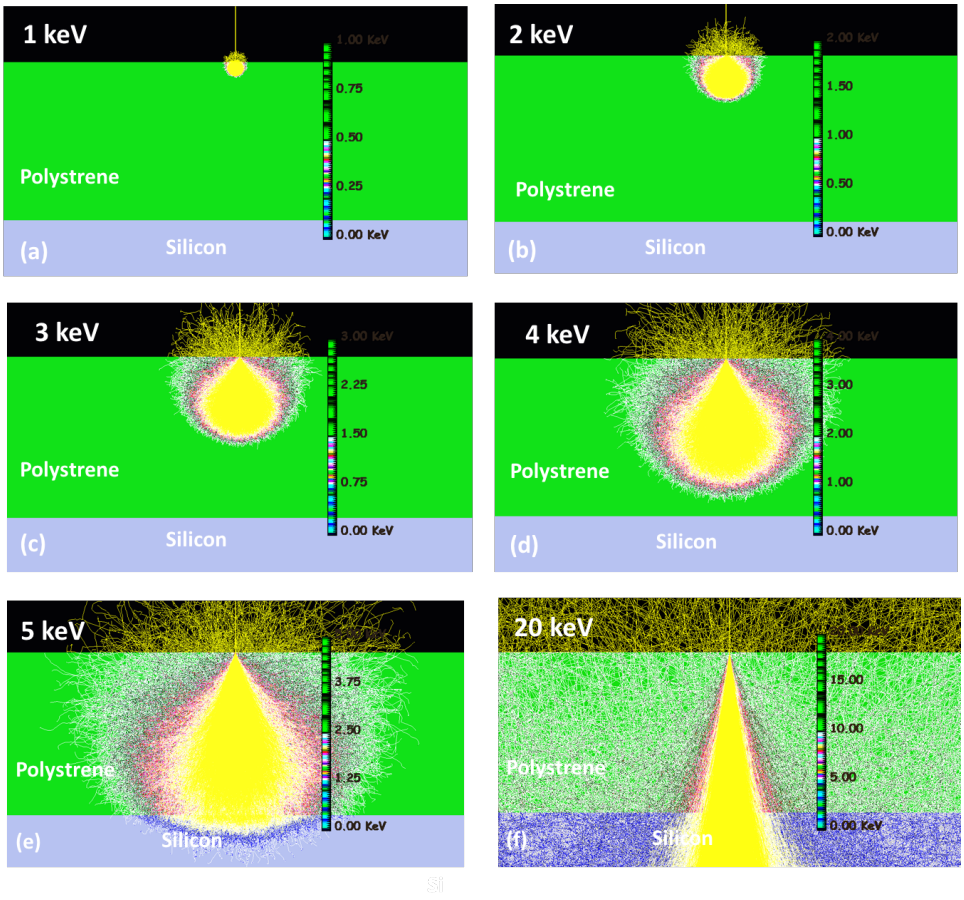

Figure 2.12. Monte Carlo simulation of 10 000 electron trajectories in 500 nm thick polystyrene coated on silicon with electron energy of (a) 1 keV, (b) 2 keV, (c) 3 keV, (d) 4 keV, (e) 5 keV, and (f) 20 keV.[48]

Forward scattering has higher rate inside the resist than backscattering. The main parameter is the energy of the electron whereas backscattering is dependent on energies of both of the

electron and the substrate nature (atomic number, Z). The relation between energy of the electrons and the forward and back scatterings happening inside the resist and the substrate is shown in Figure 2.13. As the electrons penetrate into the resist, some of them undergo small angle scattering events and this makes the beam profile broader at the bottom of the resist than the top. Hence, forward scattering has to be minimized for high-resolution patterning and this can be done via using thinner resist and/or higher voltage.

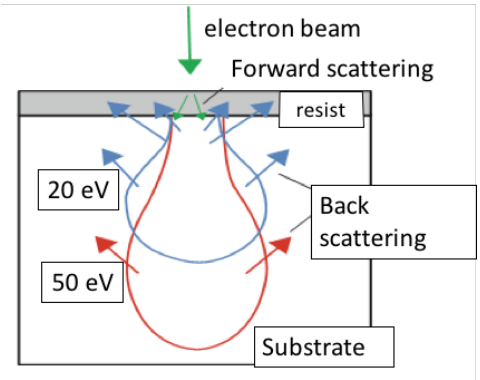

Figure 2.13. Forward and backward scattering in resist and substrate.

Forward scattering of primary electrons generates secondary electrons with low energies (typically 20-50 eV), and they are responsible for the major exposure of the resist. Contrary to trajectories inside the resist, electrons have more chance to get scattered with larger angles when they reach into the substrate, and these electrons may return back through the resist and create additional exposure on the resist far away from the initial collision. This is called the proximity effect and is shown in Figure 2.14.

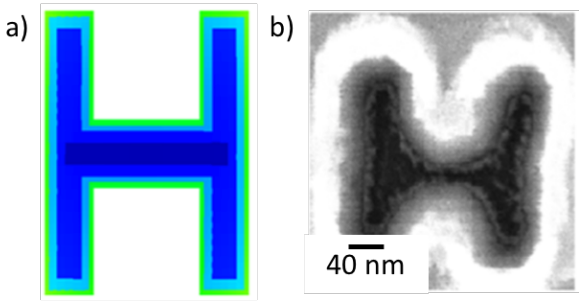

Figure 2.14. Illustrations of (a) designed (left) structure, and (b) patterned (right) structure. Due to proximity effect, nearby area of the desired region is also exposed.

To overcome the proximity effect, several attempts can be made. One of them is the dose modification which can be done after knowing the required exposure dose for each pixel with a reasonably high accuracy. A numerical calculation is needed to predict the pixel-to-pixel interactions which is time consuming. Another technique is to modify the design pattern by adding/removing the pixels at which proximity effect will be seen. Effect of this correction is shown in Figure 2.15.

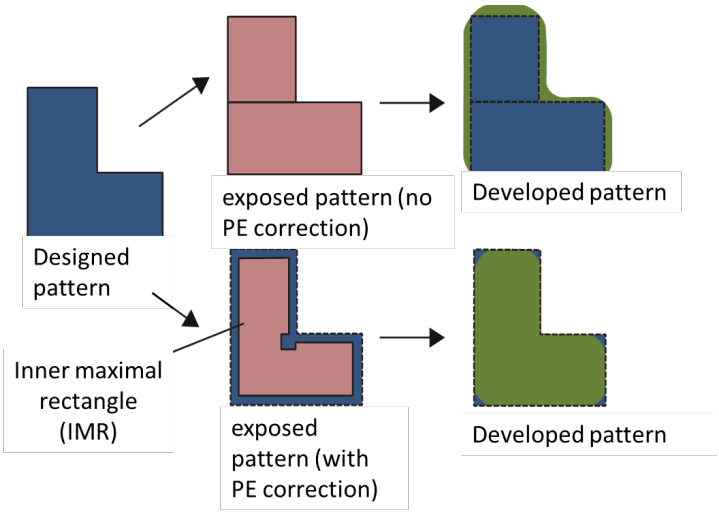

Figure 2.15. Proximity effect (PE) correction by shape modification at critical points.

Other techniques include software correction and GHOST[45] where inverse tone of the pattern is written with a defocused beam to imitate the shape of the backscatter distribution, which gives the pattern a uniform background dose. However, it needs extra data preparation and writing time.

2.3.5. Beam shapes and scanning modes

As stated earlier, electron beam lithography systems can be developed from the scanning electron microscopy by adding beam blanker and the CAD software into the system. This type of EBL systems provide huge savings for academic research facilities (costs 100K USD) since dedicated EBL systems are more expensive (2 M USD). Many of these systems use Gaussian beam, which is a rounded beam focused to a minimum spot size to achieve high resolution. However, in direct writing EBL systems, such exposure of one pixel at a time limits the exposure speed or patterning rate. Hence, variable shaped beam is made to increase the throughput by enhancing exposure speed and integrating with other nanoscale processes.[49,50] Basically, shaped beam system aims to write a primitive shaped cell (mainly rectangles), where it uses parallel electron beams. Recently, by increasing the resolution to 65 nm, the integration and high-yield manufacturing of integrated circuit (IC) were made possible by Motorola, Philips Semiconductors and STM Microelectronics.[49]

In EBL writing systems, there are two different writing strategies that can create pattern on the resist: raster scan and vector scan, as shown in Figure 2.16. In raster scan mode, the beam scans the entire field and keeps moving along the desired writing direction, and switches on and off by beam blanker to do exposure. Raster scan is very simple and repeatable, but it needs longer time than the vector scan as it has to move to every pixel. Also, as it uses the one-time focus adjusted beam, it may result in defocus during the writing and hence lose the resolution. To overcome this

issue, laser height adjustment control should be built inside the EBL system.

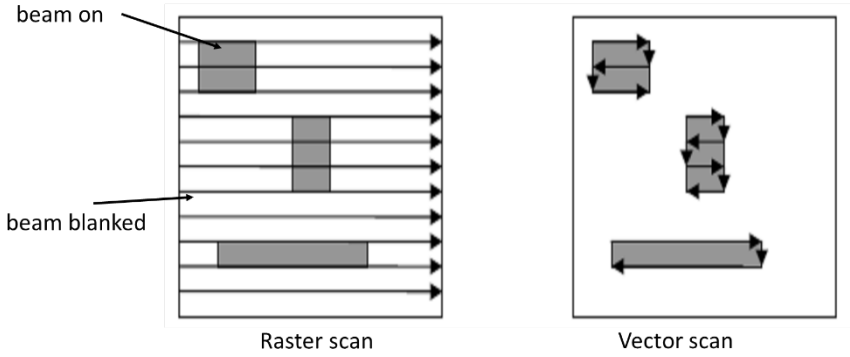

Figure 2.16. Scan systems for EBL: raster and vector scan modes.

Vector scan mode is developed in order to speed up the writing for sparse patterns. In this type of scanning, the beam is only shifted to the desired area to be patterned while it never moves to unwanted areas. One advantage is that it enables change of the exposure dose while switching from one area to the other. Another advantage of the vector scan is that it has high precision on patterning.

2.3.6. Resist materials for electron beam lithography

2.3.6.1. General characteristics of e-beam resists

It is the resolution capability of EBL that makes it popular in R&D. EBL is a maskless lithography technique, and the patterns are transferred into the substrate using a thin layer of polymer film called "resist". These polymers undergo physical and chemical change under ionizing radiation by electron beam. In terms of physical change, color, impact strength, elastic and tensile strength are changed. In chemical modification, polymer chains crosslink or scission of the chain occurs. Contrary to resists for photolithography, those resists are usually not sensitive to UV- and visible light (but often sensitive to shorter wavelengths) and have much longer shelf-life and stability. With sufficient e-beam radiation on the resist, the chains link to

each other to form a complex structure, i.e. crosslinking, and its molecular weight increases; or chains undergo a random scission and degradation, and its molecular weight decreases. Figure 2.17 is shown as an example. It is called negative type resist if the former process dominates and positive type resist if the latter happens.

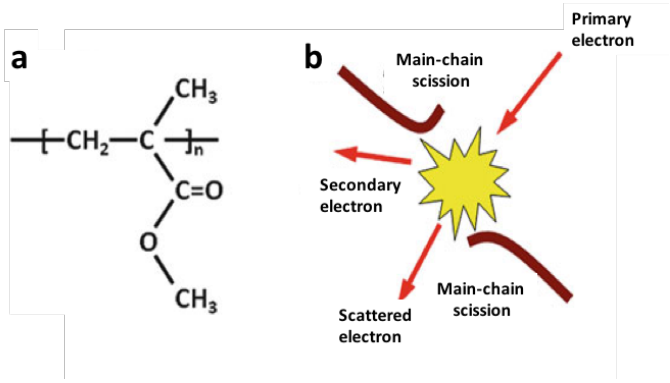

Figure 2.17. (a) Polymer sub-unit of poly (methyl methacrylate), and (b) scission of the polymer chain during EBL exposure.[12]

Generally speaking, with sufficient dose, the negative e-beam resist will be cross-linked to form a three-dimensional network. The unexposed linear polymer can be dissolved by a solvent developer, whereas the exposed and thus cross-linked part becomes insoluble and will remain after development. This is because in a negative tone resist, the electrons convert the material to less soluble in developer. This gives the resist negative tone behavior. In positive e-beam resist, chain scission is induced by e-beam exposure; and selective removal of the exposed resist, which has a greatly reduced molecular weight, can be realized using a poor solvent that does not dissolve appreciably the unexposed resist. Positive tone resists undergo a conversion from low to high soluble in developer upon exposure to electrons. The most well-known e-beam resist is PMMA which was first developed in 1960s, though there are other resists to come and go as they rise and fall in popularity. One of its exposure characteristics is acceleration voltage dependency.

Studies revealed that higher acceleration voltages require higher exposure dose for the same defined pattern area. The required dose to expose the certain area is 100 μC/cm^2 for 10 kV whereas it increases to 180 μC/cm^2 for 20 kV applications, as shown in Table 2.2. This is because at higher voltages, fewer electrons are scattered inside the resist to result in chemical modification of the resist.

Table 2.2. Typical exposure dose of PMMA resist with different acceleration voltage. Required doses to expose the certain area is increasing as acceleration voltage increases.

	10 kV	**20 kV**	**30 kV**
Area dose (μC/cm^2)	100	180	250
Line dose (nC/cm)	0.5	0.9	1.3

Today, in resist technology, an ideal e-beam resist should have high resolution, high sensitivity, and high dry etching selectivity for pattern transfer. In the following section, some important properties of electron beam resists will be discussed.

2.3.6.2. Important parameters of e-beam resists

Electron dose (usually with unit μC/cm^2) is the electron charge per unit area to achieve the chemical modification in the resist. In EBL, each lithographic process has an optimum dose that results in desired exposure. In order to determine this dose, preliminary exposure and imaging has to be done by suitable tool (i.e. scanning electron microscope, atomic force microscope) because the electron dose affects the actual size of the patterned features: With low dose, for positive resist, the structure will be smaller in size than the designed one or larger with high dose (over exposure), and these parameters are varied depending on the designed patterns as proximity effect has to be considered as well. As dose increases, the average fragment size decreases and solubility in the developer increases.

Contrast and sensitivity are other important resist parameters: E-beam resists are characterized by their contrast curves, which can be obtained by plotting the measured remaining resist thickness after exposure and development of a series of large square patterns with increasing doses. Contrast (γ) is defined by the slope of the linear portion of the falling edge (positive resist) of this curve and is calculated by

$$\gamma \equiv \frac{1}{log_{10}\left(\frac{D_1}{D_0}\right)} \tag{2.4}$$

where D_0 is the dose at which resist dissolution by developer begins, and D_1 is the lowest dose when the resist is fully dissolved. It is called high contrast when the slope is steep. For example, as shown in Figure 2.18, positive resist "A" has higher contrast than positive resist "B". Typical high resolution resist has a contrast of $\gamma>2$, and high resolution e-beam resists such as PMMA can have contrasts in the range of 6 to 9 depending on the process conditions such as developer strength, development temperature and time, and pre-exposure bake time and temperature. Sensitivity, on the other hand, is commonly defined as D_1, and in Figure 2.18, resist "A" has higher sensitivity than resist "B".

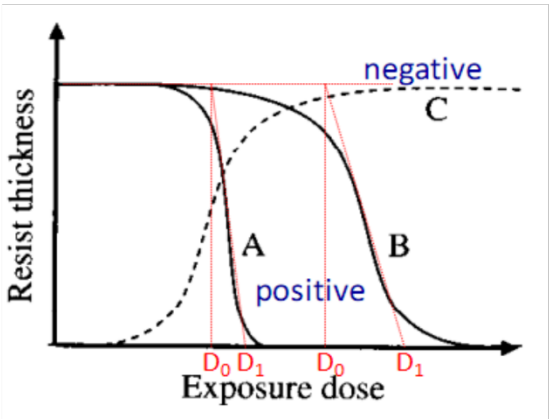

Figure 2.18. Contrast curves of resist A, B, and C.

Line edge roughness (LER) is a serious issue when the pattern size gets smaller, and LER must be as small as possible for high-resolution patterning. Typical measured LER values are about 3 nm when resists with a very high contrast are used.[51] The cause of LER can include the lithographic system (i.e. dose fluctuations), resist materials, and the development process. However, the main reason of LER is derived from the aggregation of the polymer which is naturally present in all the resist.[43] This aggregation causes uneven dissolution rates between the aggregates and the surrounding areas. On the sidewalls of these areas, the aggregations are low at the edges where LER is determined. LER is encountered in all e-beam resists and cannot be eliminated completely, though there are ways to minimize it. For instance, it can be minimized by using small molecular size resists such as HSQ or calix[n]arene. Yamaguchi developed a novel type of resist by chemically amplifying the ZEP-520 resist and reduced LER to 2 nm, whereas it is more than 3 nm with conventional ZEP-520 resist.[52]

The resolution, i.e. the capability of resolving very small features, is one of the most important parameters for electron beam lithography and hence for e-beam resists. It is often the first term mentioned when defining an electron beam resist. When the pitch of features, i.e. distance

between adjacent features, decreases, it gets harder to achieve high resolution patterning due to proximity effect. Recently, 2 nm isolated features and sub-5nm resolution structures are reported by using very high keV (200 keV) that minimizes proximity effect and forward scattering.[53]

Etch resistance is the ability of the resist to survive during the etching process, which might be the most difficult requirement of the resist. In conventional EBL process, after development, as shown in Figure 2.19, the pattern is usually transferred into the underlying layer by either a wet or dry etch process. In wet etching process, although it results in high throughput and good selectivity, it can lead to loss of adhesion of the resist and isotropic etching, and hence loss of sizes of the features. However, with dry etching, where plasma is used to transfer the defined features to the substrate, a vertical profile can be obtained. That is, anisotropic etching is possible, resulting in the faithful replication of the pattern to the underlying layer. The physical and chemical properties of the resist material represent the main limitations for the etching process. In general, a very high etch resistance is preferred.

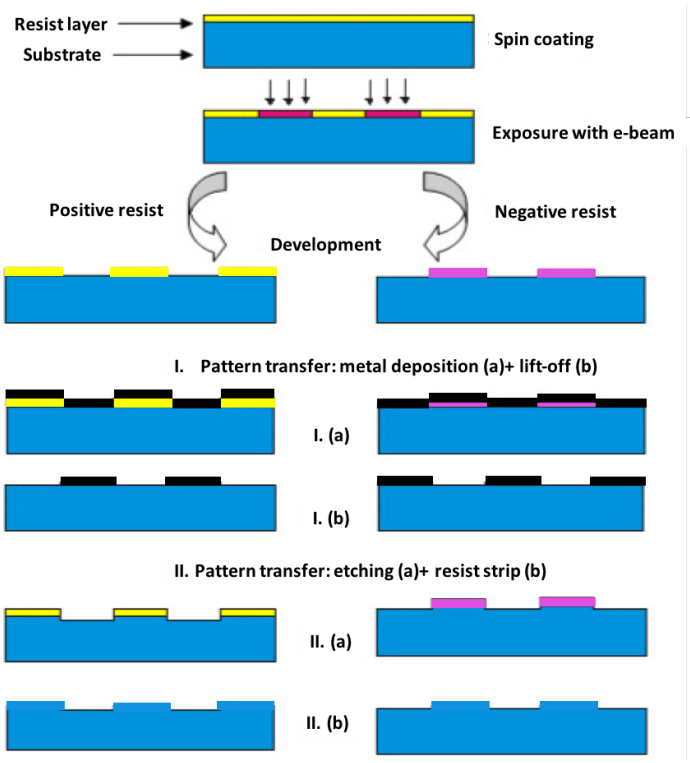

Figure 2.19. Schematic representation of the basic steps of a lithographic process including coating, exposure, development and pattern transfer such as lift-off & etching.

There have been numerous efforts on investigation of electron beam resists in order to increase the sensitivity, and the etching selectivity while achieving high resolution. In general, e-beam resist is categorized as organic, inorganic, and hybrid resists, though there are novel resists such as silk, ice, and sugar, etc. Some commonly used resists and their characteristics such as sensitivity, contrast, critical dimension and developers are given in Table 2.3 below.[3] In following sections, these resists will be discussed with their special characteristics.

Table 2.3. Comparison of lithography properties of most frequent electron beam resists.[3]

Resist	Resist tone	Sensitivity (μC/cm²)	Contrast	CD (nm)	Developer	Chemical structure
PMMA (350 k)	Positive	230 (@100 kV)	3-4	≤ 5	MIBK:IPA, O-xylene	Poly methyl methacrylate
PMMA (100 k)	Positive	163 (@100 kV)	3-4	≤ 5	MIBK:IPA, O-xylene	Poly methyl methacrylate
PMMA-MAA	Positive	84 (@100 kV)	3-4	~ 10	MIBK:IPA, O-xylene	Poly(methyl methacrylate-co-methacrylic acid)
UVIII	Positive	18 (@100 kV)	11.8	~ 30	CD26	TMAH (Tetramethylammonium hydroxide)
UV1116	Positive	38-90 (@100 kV)	10.4	30	CD26	TMAH
ZEP520	Positive	73 (@100 kV)	7.8	~ 10	O-xylene	a-Hloromethacrylate+a-methylstyrene
UVN-30	Negative	5 (@100kV)	6	~ 90	CD26	unavailable
HSQ	Negative	334 (@100 kV)	1.1	≤ 5	CD26, MIBK, TMAH	Hydrogen silsesquioxane
SU-8	Negative	3-7 (@100 kV)	3.5	20-30	EC solvent, cyclopentanone	8 epoxy groups
SAL-601	Negative	10-30 (@50 kV)	5-6	60	TMAH	-
NEB	Negative	9-14 (@50 kV)	4.7	Sub-10	CD26	-
Calix[n]arene	Negative	80-150 (@50 kV)	1.5-1.9	10-20	MIBK	P-Methylcalix[n]arene
PS	Negative	1170 (@ 5keV)	3.4-4.4	~ 5	xylene	Polystyrene

2.3.6.3. Popular electron beam resists

Poly methyl methacrylate (PMMA), ZEP, polystyrene (PS), polydimethyl glutarimide (PMGI) and poly l-butane sulfone (PBS) are common types of organic resists. PMMA, first developed electron-sensitive polymer in 1960's,[42] is currently still one of the most popular e-beam resists. During e-beam exposure, as drawn in Figure 2.20, long chains of PMMA are fragmented into smaller chains, making/rendering it soluble in solvents, weak solvents generally.[54,55] At low exposures, the scission process dominates and hence PMMA behaves as positive type e-beam resist; whereas at high exposure doses, the polymerization becomes dominant in the resist and it behaves as negative type e-beam resist.[56] When it is used as negative tone resist, the dose is almost 10 times higher than the ones usually used for positive tone PMMA.

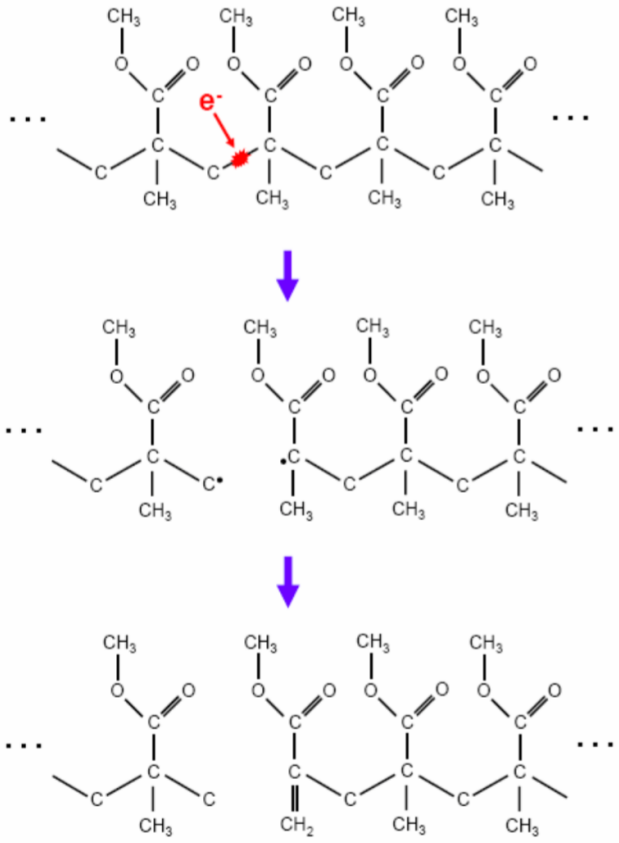

Figure 2.20. Schematic illustration of a possible mechanism for PMMA scission suggested by Alexander et al.[54] The carbon-backbone bond is first broken by an incident electron, generating two PMMA chains with free radicals at their ends. The damaged monomers then rearrange themselves to neutralize the dangling bonds, resulting in two stable chains of PMMA.[56]

PMMA can achieve a contrast in the range of 6 to 9 depending on the developer type, temperature, and strength. For the development of PMMA resist, usually methyl isobutyl ketone (MIBK) and its mixture with isopropyl alcohol (IPA) are used. MIBK is a strong solvent for PMMA and controls the solubility and swelling, and IPA dilutes and weakens the developer. Although IPA is used to develop 40 nm thick PMMA, it cannot fully develop thick PMMA at any dose, since the electrons begin to crosslink the polymer before the average molecular weight is low enough for dissolution. MIBK and IPA are hence mixed to progress at positive&negative

tone boundary. The concentration of the developer mixture affects the sensitivity and the resolution, given in Table 2.4, and higher concentration of MIBK results in higher sensitivity but lower resolution.[57] Typical conditions of high resolution patterning with 200 nm thick PMMA resist is to use MIBK:IPA 1:3 with 1 minute development.

Table 2.4. Influence of developer concentration on resist resolution.

Developer concentration (MIBK:IPA)	Sensitivity	Resolution
1:3	Low	Extremely high
1:2	Medium	Very high
1:1	High	High
Pure MIBK	Very high	Low

Besides the choice of the solvent, development condition such as temperature is another factor affecting resolution and sensitivity of the resist. Recently, Cord reported that PMMA can achieve sub-10 nm resolution by doing cold development, lower temperature than the room temperature, (in Figure 2.21).[56,58] It is reported that at low temperature of -15 ^{o}C, and using mixture of MIBK:IPA 1:3 ratio, dissolution rate of PMMA molecules decreases, hence the loss of the PMMA molecules at the trench edges will be less than that at room temperature.[56] In room temperature development process, fully and partially exposed polymer chains are readily developed by the solvent. However, in cold development process, those partially exposed parts remain insoluble in the developer. This is observed however at certain temperature range where it is linked to the fragments' glass transition temperature.[56] It is believed that while sensitivity of the resist is reduced too much during the process, a large amount of cross-linked material is created in the exposed region. These polymers will decrease the dissolution of the exposed PMMA, and hence the contrast and resolution of the resist will be lowered.

Several reports also state that pure IPA with ultrasonic agitation can also be applied for the

development.[59] Some others use cellosolve (2-ethoxyethanol): methanol= 3:7 which gives better contrast than MIBK.[60] Interestingly, mixture of water and IPA can also be applied for the development while neither of these solvents dissolve the resist individually.[61] The mixture of water and IPA acts as a so-called co-solvent, with a solvent strength larger than either separate component where highly polar water molecule improves the solvent action of IPA. This can be explained by the modification of the alcohol molecule by water molecule or by the interaction between water and PMMA molecule.

In summary, PMMA resist is cost-efficient and provides high resolution, high contrast, and low sensitivity, but it has poor etching resistance to oxygen based and fluorine based plasma etching. Hence, it is not a good resist for pattern transfer using dry etching; instead, metal deposition and lift-off is a preferred way to do pattern transfer using PMMA resist.

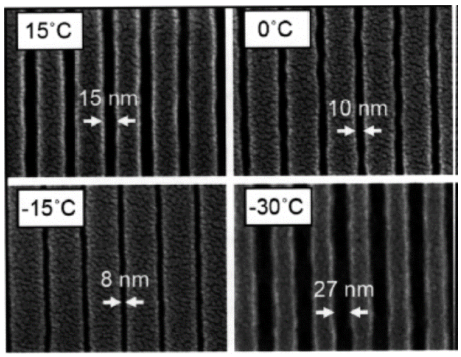

Figure 2.21. SEM images of 60-nm-pitch gratings developed at 15 ^{o}C, 0 ^{o}C, -15 ^{o}C, and -30 °C and etched into a Si substrate, showing the minimum achievable linewidth at each development temperature. The resolution is improved as the temperature was reduced, peaked at -15 ^{o}C, then dropped sharply at -30 ^{o}C. The poor line-edge definition and bridging in the -30 ^{o}C micrograph are characteristic of sloped resist sidewalls, a symptom of poor resist contrast. The "scaly" coating on the Si in all four micrographs is a 2-nm-thick Au-Pd layer deposited just before SEM analysis to help reduce charging and had no effect on the process itself.[56]

Compared to PMMA, brand co-polymer (1:1 alpha-chloromethacrylate and alpha-methylstyrene) ZEP (chemical structure is shown in Figure 2.22) provides higher sensitivity (3-5 times higher)

and etching resistivity (3 times higher than PMMA). ZEP, which is developed by ZEON Inc., can also be used as negative type e-beam resist with higher doses, though it is mostly used as positive e-beam resist. The higher sensitivity and etching resistivity is linked to the presence of the chlorine and phenyl groups, respectively.[62] There are two common available formulations of ZEP available: ZEP-520 and ZEP-7000, where the main difference is their molecular weight, 67 and 476 kg/mol, respectively; it is reported that higher molecular weight results in higher contrast.[63] ZEP-520 is reported with its sub-20 nm resolution capability.[2,64]

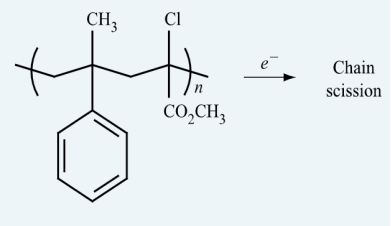

Figure 2.22. Poly(methyl-α-chloroacrylate-*co*-α-methylstyrene), the polymer comprising ZEP resist.

It is reported that composition of xylene (ZEP-RD), n-amyl acetate (ZED-N50), and MIBK, 2-butanone (ZEP-SD) can be used as a developer, shown in Table 2.5[2,65,66,67] as well as mixture of MIBK and IPA and water and IPA. Mohammad et al. compared the sensitivity and contrast values by using these developers at room temperature and cold development (-15 ^{o}C) (Table 2.5).[68]

Table 2.5. Dose window information for various developer and development conditions employed in this study.[68]

Developer	Dose window at 22 °C		Dose window at -15 °C	
	Values (pC/cm)	D_{max}/D_{min}	Values (pC/cm)	D_{max}/D_{min}
ZED-N50	100-205	2.05	213-525	2.46
MIBK:IPA 1:3	435-627	1.44	566-1212	2.14
IPA: H2O 7:3	863-3256	2.73	No clearance	

According to this report, ZEP-520 can give better contrast value with higher sensitivity, and lower dose requirements if ZED-N50 (or n-amyl acetate) is used as a developer. The highest resolution positive tone features are shown in Figure 2.23 with 13 nm gaps in 40 nm pitch and aspect ratio of nearly 1:4.5 in 60 nm thick ZEP-520 resist, where development is done by n-amyl acetate for 5 seconds at cold temperature (-15 °C).[68]

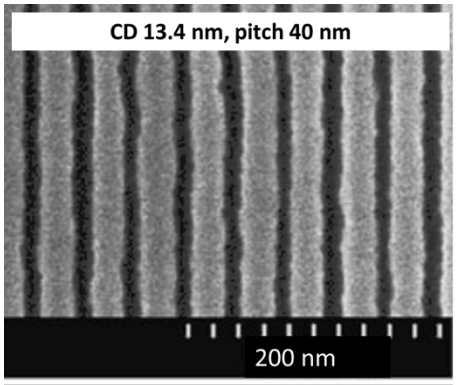

Figure 2.23. Highest resolution/density patterns fabricated using 180 pC/cm, 5 s ZED-N50 at -15 °C.[68]

Major drawbacks of ZEP resist are only one-year shelf-life and high cost. To overcome these issues, some resists are being developed which have quite similar properties in terms of chemistry, sensitivity and resolution capability, but longer shelf-life and/or lower cost. Recently, CSAR-62 from Allresist Inc. is reported with similar contrast values where it consists mainly of a 9% solution of poly(α-methylstyrene-co-α-chloromethacrylate) with a molecular weight of 38 kg/mol dissolved in anisole, with small additions to improve the electron beam sensitivity.[69]

However, after development, it leaves higher amount of residual layer behind than the ZEP520A resist, the reason of which has not been understood yet.

Self-assembled monolayers (SAMs) are also used as an e-beam resist for possible high resolution capabilities. SAMs are typically 1-10 nm thick with 0.5-1 nm intermolecular spacing.[43] These are organic molecules that spontaneously bind to certain materials such as silicon dioxide, metals, gallium arsenide, to form ordered monolayers.[70] This can be done e.g. by immersing the substrate into the solutions of octadecyltrichlorosilane (OTS). SAM resist can offer both positive and negative tone behavior. Recently, Lercel et al. patterned GaAs and SiO_2 using OTS with 25 nm resolvable features and 100-200 $\mu C/cm^2$ sensitivity.[70] However, as they are very thin with poor dry etching selectivity and wet etching results in isotropic profile, two-step etching process was employed for pattern transferring.

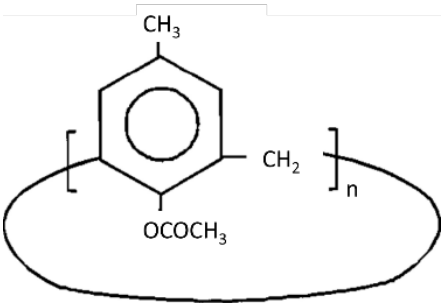

Figure 2.24. Chemical structure of calix[*n*] arene, where *n* is the number of phenol groups.[71]

Chemically amplified resists (CARs) are also capable of high resolution patterning. Calix[n]arene, (chemical structure shown in Figure 2.24) is one of the examples of CARs.[71] A typical CAR has two components: a matrix copolymer and a photo-acid generator (PAG). After the e-beam exposure, post-exposure bake is performed to catalyze the reaction between the acid molecule and the protecting group, and the generated acid initiates a chain reaction which causes

several chemical reactions inside the resist, hence it is called chemically amplified resist. As a result, the exposure can be done at low doses. As shown in Figure 2.25, by using 30 nm thick calix[n]erene film, Fujita et al. achieved 15 nm diameter and 35 nm pitch dot array.[72] Yet the standard area dose for calix[n]arene is almost 20 times higher than that for PMMA.

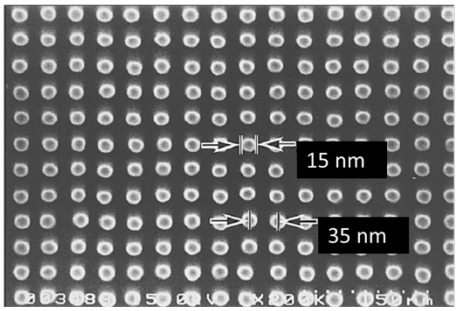

Figure 2.25. SEM image of 15 nm dots at a pitch of 35 nm written in 30 nm thick calixarene resist.[72]

Other examples of CARs include fullerenes and SU-8 resists.[73,74,75,76] The electron beam exposure sensitivity for SU-8 was found to be extremely high, making it ideal for patterning over large writing area; and by modifying its chemistry, it can achieve sub-30 nm resolution (Figure 2.26).[76,77]

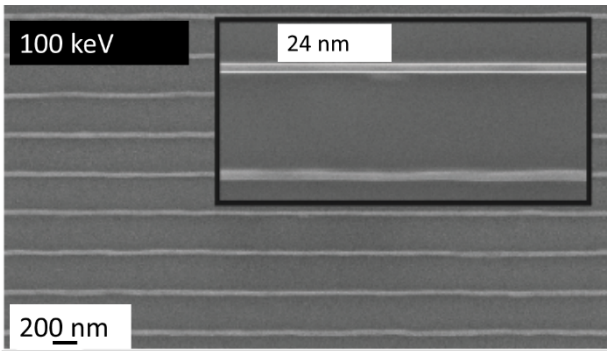

Figure 2.26. SEM images of 24 nm wide lines achieved by using SU-8 negative resist.[77]

Hydrogen silsesquoxiane (HSQ) (chemical structure is shown 2.27) is an inorganic negative tone e-beam resist that can achieve sub-10 nm resolution.[43] HSQ has a cage-like structure which are in various sizes, and it becomes a network structure upon e-beam exposure.

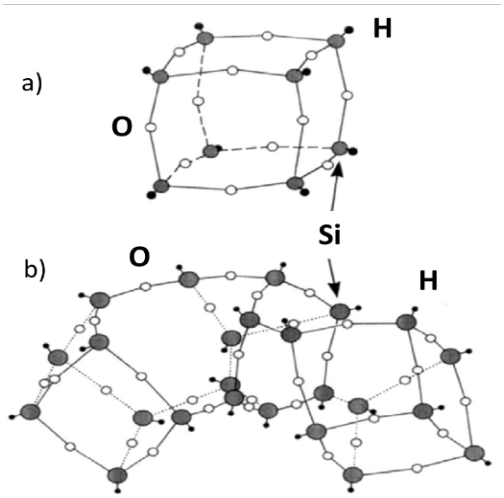

Figure 2.27. Schematic representation of the molecular structure of HSQ: (a) cage structure for an eight-corner oligomer; (b) random structure of the resist solution.[43]

HSQ is popular with its high resolution and high contrast.[43] Yang et al. achieved 4.5 nm half-pitch line array pattern using 10 nm thick HSQ film as an e-beam resist (shown in Figure 2.28).[78] HSQ, however, cannot be developed by a solvent. After exposure, unexposed part of the resist reacts with bases such as ammonium hydroxide (NH_4OH) or sodium hydroxide (NaOH) developers to produce hydrogen gas (H_2), and the development is done once the reaction reaches the saturation point. On the other hand, it has very short shelf-time and handling and processing are not as easy: once it is spin-coated, it has to be baked, exposed and developed promptly so that its properties are not lost.

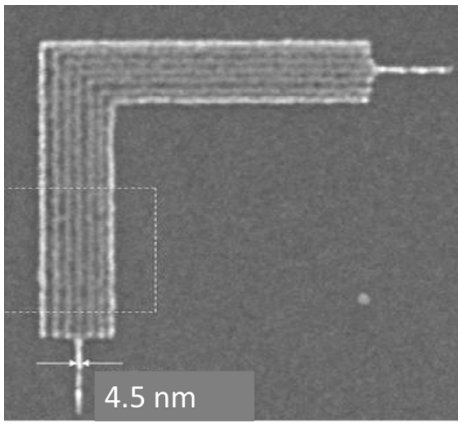

Figure 2.28. 4.5 nm half pitch lines with 10 nm thick HSQ negative resist.[78]

Metal halides such as aluminum fluoride (AlF_3), lithium fluoride (LiF), sodium chloride (NaCl), CaF_2, MgF_2 and metal oxides such as AlO_x, ZnO and TiO_x are the examples of inorganic electron beam resists which also have self-developing capabilities. They either dissociate to halide components, or volatilize the fluorine component and metal component diffuses at the substrate surface. Hence, metal halides behave as positive tone whereas metal oxides as negative tone electron beam resist.[43] Contrary to conventional electron beam resists, these resists can be deposited on the substrate via sputtering or thermal evaporation techniques. As they have metal component inside the molecules, they have high dry etching selectivity compared with other resists such as PMMA and ZEP. However, they have very low sensitivity (almost 10 C/cm^2). Muray et al. reported a dense array of very small holes (shown Figure 2.29) of 2 nm in diameter with 4 nm pitch, fabricated by AlF_3 resist.[79] These resists, however, cannot produce arbitrary structures such as rectangles due to limited lateral diffusion range of the resulting metallic aluminum upon beam exposure.[79,80,81]

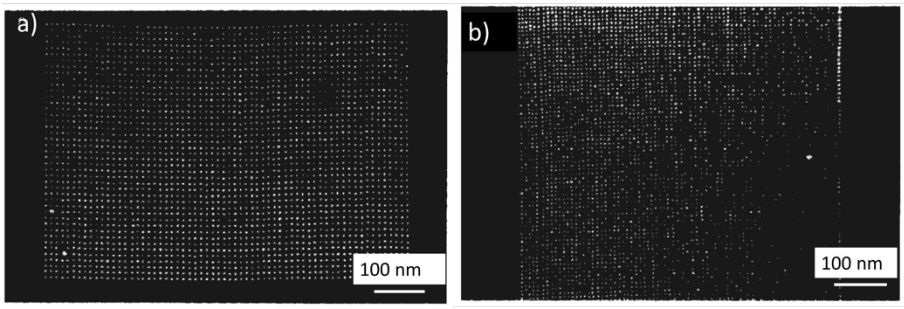

Figure 2.29. Annular dark field STEM image (ADF-STEM) of arrays of holes in AlF_3 resist: (a) 4 nm diameter and 8 nm pitch; (b) 2 nm diameter and 4 nm pitch.[79]

Another example of metal-containing resist is polyferrocenylsilane (PFS), its derivatives containing iron (Fe) and silicon, and PFpP.[82] Co-PFS, cobalt-clusterized polyferrocenylsilane (chemical structure is shown in Figure 2.30) can be used as negative tone electron beam resist with 0.5 μm resolution capability. However, these metal-containing polymers are extremely hard to synthesize.[83]

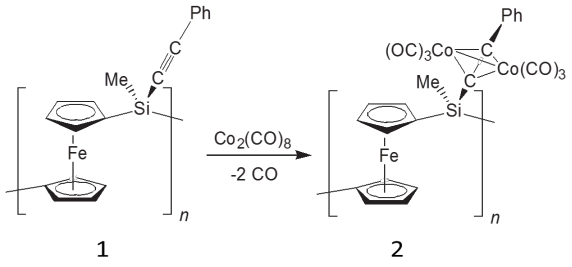

Figure 2.30. Synthesis of cobalt-clusturized polyferrocenylsilane (Co-PFS).[83]

PFpP, on the other hand, is a newly emerged main-chain, metal-carbonyl metal-containing polymer with the backbone constructed from both P–Fe metal coordination and Fe–C bonds (Figure 2.31). Recently, Zhang et al. reported 17 nm line-width with 20 nm half pitch lines.[84] PFpP also has better oxygen plasma etching resistance, 4 nm/min, whereas it is 200 nm/min for

PMMA resist. However, it has low sensitivity (12000 μC/cm^2) and contrast (1.0).

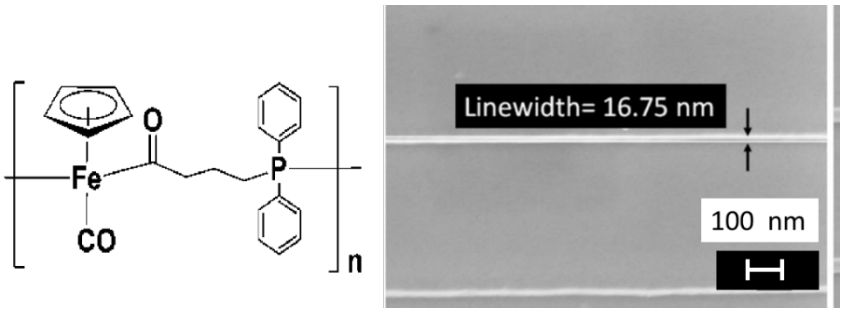

Figure 2.31. a) Chemical structure of PFp, and b) SEM image of exposed line array pattern using PFpP, 500 nm pitch, 17 nm line-width, exposed at 15 nC/cm.[84]

Chapter 3 Fabrication techniques for patterning on non-planar and fragile substrates using evaporated electron beam resists

The following section is based on previously published work[85] by Zhang J, Con C., and Cui B. ACS Nano 2014, 8 (4), 3483-3489
"**Electron Beam Lithography on Irregular Surfaces Using an Evaporated Resist**"
Reproduced with permission.

3.1. Introduction and Motivation

One challenge in nanofabrication is to pattern on non-flat or pre-structured surfaces, which is desired in many fields such as MEMS,[86] electronic devices,[87] super-adhesive surfaces,[88] and optical devices.[89] For example, nanopatterning on optical fibers allows the so-called lab-on fiber technology,[90] and that on an atomic force microscope (AFM) tip allows tip enhanced Raman spectroscopy,[91] near-field optical focusing,[92,93] and the study of fundamental quantum mechanical systems.[94,95] In addition, nanofabrication on a cylindrical roller may be needed as the mold for roll-to- roll nanoimprint lithography (NIL).[96,97] However, it is far more challenging to fabricate nanostructures on non-flat surfaces than flat ones such as a wafer, for which the popular resist coating method spin-coating works well.

Previously, various methods have been demonstrated to create nanostructures on non-flat surfaces. For slightly non-flat yet regular surfaces such as a macroscale curved surface, spin-coating may still be employed to coat the resist, which can be patterned by NIL using a flexible mold capable of conformal contact to the surface.[98] For a non-planar surface without sharp

corners or edges such as a V-shaped trench on a wafer, spray-coating may be used to coat a uniform layer of resist over the trench.[99] Spin-coating using a very low viscosity resist solution can be coated uniformly on the side of ridges patterned on a silicon wafer, yet only when the ridge is aligned along the radial direction during spinning.[100] Electron beam resist applied by the Langmuir-Blodgett method can also be coated on a curved surface, but pattern transfer by dry etching is problematic due to the extremely thin resist thickness;[101] this is also the case for a self-assembled monolayer resist (pattern transfer through an intermediate wet etching step has been demonstrated, yet wet etching has poor CD control compared to dry etching).[102,103] In principle, the resistless nanolithography method, notably focused ion beam milling or deposition, can be used to pattern any surface, yet its cost is higher and its throughput is much lower than electron beam lithography (EBL). Therefore, it is believed EBL using a vacuum-deposited resist is the most efficient method for patterning irregular non-planar surfaces.

Previously, Pedersen et al. have reported the coating of an electron beam resist using plasma-polymerized hexane.[104] The resulting hydrocarbon resist presented a negative tone when developed in a 1:1 mixture of cyclopentanone and o-xylene for 40 min. However, besides its low sensitivity and poor resolution (demonstrated a 150 nm wide sparse line array), this approach is not ideal for a wide range of applications, as it needs a special custom-built plasma chamber. Eric et al. have developed a negative evaporated sterol resist, named QSR-5, which was employed to pattern on an optical fiber and laser diode facet, as well as on the backside of membranes for the fabrication of an X-ray mask.[105,106,107] Yet, in addition to its moderate resolution, this specially formulated resist is not commercially available. Daniel et al. introduced water vapor into the SEM chamber and formed ice on an AFM cantilever or graphene film, which was cooled to < 120 K. The thin ice layer was patterned by e-beam exposure with low

voltage. This novel patterning process is named ice lithography.[91,108,109] However, for ice lithography the resist has to be kept at very low temperature before pattern transfer by lift-off or dry etching is completed, thus a specially designed tool or tool accessory is needed. In addition, the resist sensitivity is very low, three orders lower than PMMA, which is already considered an insensitive resist. Similar to ice, frozen CO_2 can also be used as an electron beam resist, although it would suffer from the same drawbacks as an ice resist.[110]A metal halide such as AlF_3 is another type of inorganic evaporated resist, which again suffers from extremely low sensitivity, and it is able to form only line or dot (not areal) patterns.[79,81] Lastly, silicon dioxide, which can be grown or coated by various thin film deposition methods, has been used as a kind of electron beam resist, yet its sensitivity is again extremely low.[111]

Therefore, there is still a great demand for a simple process using a cheap and readily available evaporative resist for nanofabrication by EBL on an irregular non-flat surface with high resolution. Here, it will be shown that low molecular weight polystyrene (PS) satisfies all these criteria. Although its sensitivity is much lower than PMMA, it is two orders higher than the above mentioned inorganic resists (e.g., >1 C/cm^2 needed for exposing an ice resist). Previously it was demonstrated that PS is a very versatile negative resist, offering a high resolution of a 15 nm period dense dot array pattern for low molecular weight[112] and very high sensitivity on the order of 1 $\mu C/cm^2$ at 5 keV for high molecular weight.[113] Its dry etching rate is much lower than that of PMMA, which is a desirable property for pattern transfer using plasma etching. Moreover, it can be dry thermally developed to reduce pattern collapse due to the capillary force when using solvent development.[114] Additional advantages for an evaporated resist over spin-coating include the lack of edge bead effect, which is a serious issue for spin coating on small samples such as a single-crystal diamond,[115] precise control of film thickness, uniform coating

around dust particles on substrates, and negligible attack to the substrate material, which may be a polymer susceptible to dissolution or swelling by the solvent used for spin-coating.

3.2. Experimental methods

For this work, a low molecular weight of 1.2 kg/mol polystyrene is chosen (Scientific Polymer Products Inc., Ontario, NY, USA) for PS (chemical structure is shown in figure 3.1) thermal evaporation with a chamber background vacuum of 2 μTorr using an Intlvac vacuum deposition system. During the deposition, the heating power was increased slowly until a desired deposition rate of ~1 Å/s was achieved. The actual temperature of the heating boat containing PS powder was not monitored by the system, but is expected to exceed 575 K, at which appreciable weight loss was observed.[116] We were unable to obtain a uniform and thick-enough PS film for higher molecular weights such as 5 kg/mol because the process was unstable at the power needed to give significant vaporization. This process instability is due to the fast decomposition at higher temperatures and is in agreement with the observed initial sharp decrease in molecular weight when PS was gradually heated.[116]

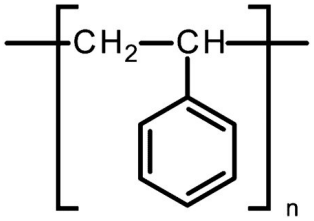

Figure 3.1. Chemical structure of polystyrene (PS) film.

The surface roughness of the PS films prepared by evaporation and spin-coating on silicon wafers was mapped by AFM. To examine the structural change of PS before and after thermal evaporation, PS films are coated by thermal evaporation and spin-coating on a KBr substrate and

we recorded their respective infrared transmission spectra using a Fourier transform infrared (FTIR) spectrometer (Bruker Vector-27, Bruker AXS GmbH, Karlsruhe, Germany). In addition, the decomposition of PS due to the high-temperature process can be examined indirectly by comparing its sensitivity with the spin-coated film, as it is known that for a simple cross-linking resist such as polystyrene the sensitivity ($\mu C/cm^2$) is inversely proportional to molecular weight (kg/mol).[117] Here for spin-coating, polystyrene powder with the same molecular weight of 1.2 kg/mol was dissolved in chlorobenzene with a concentration of 1.3 wt/vol %, which gave a film thickness of 140 nm. After spin-coating, the film was baked at 90 ^{0}C for 5 min on a hot plate. Electron beam lithography was conducted using a Raith 150TWO system with 5 kV acceleration voltage and 0.2 nA beam current. The exposed PS was developed by xylene (mixture of o-, m-, and p-xylene) for 1 min and observed by LEO 1530 FESEM. Other solvents that can dissolve the unexposed PS, including chlorobenzene, toluene, anisole, and cyclohexane, can also be used as a PS developer with similar results. The PS film was typically 100 nm thick and was coated on low-resistivity (0.01-0.02 Ω.cm) silicon wafer pieces. An AFM cantilever and optical fiber were used to demonstrate its capability of patterning on non-flat surfaces. To prepare the surface for PS coating, the buffer layer of the fiber was removed by soaking in acetone and scrubbing, followed by a solvent cleaning using acetone and 2-proponol and a short exposure to oxygen plasma. For pattern transfer to the substrate using reactive ion etching, a hard RIE mask layer of 10 nm aluminum was coated by sputter deposition, which gives a better conformal coating on the irregular surfaces than vacuum deposition. After EBL and development, the pattern was first transferred into the Al layer using ICP-RIE (Oxford Instruments ICP380 dry etching system, 50 sccm BCl_3, 5 mTorr, ICP power 800 W, RF bias power 200 W, 15 s) with the resist as a mask

with the etching selectivity PS:Al = 2:1, then into the substrate with the patterned Al as hard mask using F-based gases that etch Si (for the AFM cantilever) and SiO_2 (for the optical fiber).

3.3. Results and Discussion

Figure 3.2 shows the AFM images for an evaporated and spin-coated PS film. As can be seen, the roughness of the two films was very close to each other, with a mean roughness (Ra) of 0.239 and 0.223 nm for the spin-coated and evaporated film, respectively. However, although not evident in the AFM images, for a spin-coated film the uniformity is also affected by the dust on the substrate and the edge bead effect.

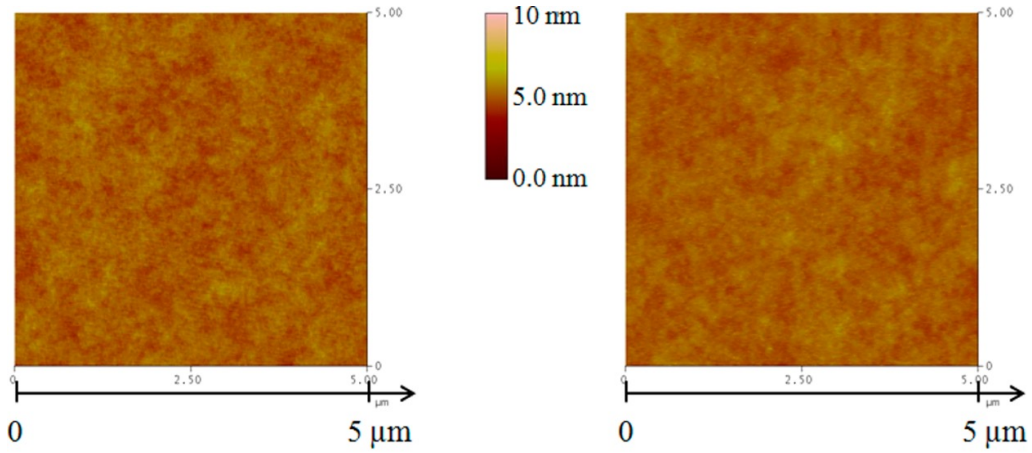

Figure 3.2. AFM images of PS films prepared by the spin-coating method (left) and thermal evaporation (right).

The IR transmission spectra for the PS film prepared by thermal evaporation and the spin-coating method are shown in Figure 3.3. Both the spectra of evaporated and spin-coated PS show peaks at 2700-3200 (attributed to the =CH- group), 1500, 1450, 1020 (attributed to the aromatic group), and ~500 cm^{-1} (attributed to the -CH2- group). This suggests that the PS film coated by evaporation was not modified chemically during heating and can thus be employed as an electron beam resist the same way as a spin-coated film.

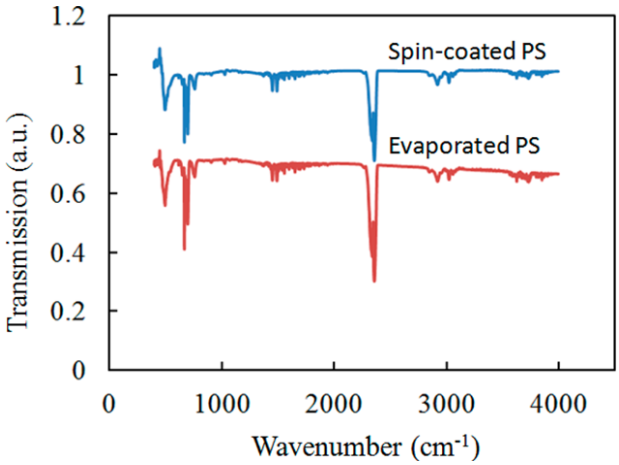

Figure 3.3. Fourier transform infrared (FTIR) spectra of PS films coated on a KBr substrate by spin-coating and thermal evaporation methods. The spectra were shifted relative to each other along the vertical axis for clarity.

Figure 3.4 shows the contrast curves for the PS coated by spin-coating and evaporation. The contrast of evaporated PS exposed at 5 keV, defined as $\gamma = [\log(D_{100}/D_0)]^{-1}$, is calculated to be 2.6, and the sensitivity (D_{50}) was derived as 4500 μC/cm^2. The contrast of the spin-coated PS is 4.3 with a sensitivity of 1920 μC/cm^2. As seen, the sensitivity is lower for evaporated polystyrene, which indicates the evaporated film has a lower molecular weight due to partial decomposition during evaporation. In fact, it is believed that PS can be thermally evaporated because its thermal decomposition involves not only end-chain scission (unzipping process), which gives styrene monomer, which cannot form a solid film, but also random chain scission, which leads to a PS chain with reduced molecular weight and increased volatility to form the film on the substrate surface.[116] On the contrary, the other popular electron beam resist PMMA cannot be thermally evaporated since its thermal decomposition is mainly an unzipping process. For other polymer resists such as polycarbonate,[118] the thermal decomposition is not by chain scission, but by significant chemical structure modification (generating carbon dioxide,

bisphenol A, and phenol for polycarbonate, leaving behind a char); thus they are unsuitable for coating by thermal evaporation.

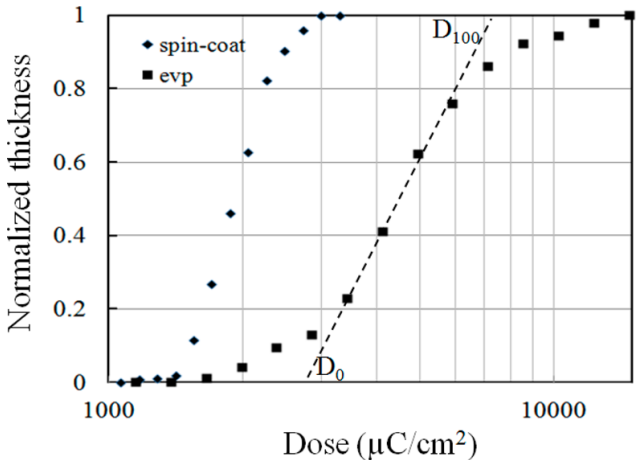

Figure 3.4. Contrast curves for 1.2 kg/mol polystyrene by spin-coating and thermal evaporation. Both were exposed at 5 keV and developed by xylene. The sensitivity (dose for 50% remaining thickness) and contrast are 1920 μC/cm^2 and 4.3 for spin-coated PS and 4500 μC/cm^2 and 2.6 for evaporated PS.

To study the resolution capability of the polystyrene resist, periodic dense line arrays with periods down to 40 nm are exposed at 5 keV. The line was written by single-pass exposure with a step size of 6 nm. Figure 3.5 shows line array patterns of 50 and 60 nm periods, which are both well-defined. A line array with a smaller period was found collapsed because of the capillary force during the drying of the rinsing liquid. The obtained half-pitch of 50 nm is much smaller than the previously reported evaporated resists.[103,104,105,106] To demonstrate its patterning capability on a non-flat surface, 50 nm PS film was evaporated onto an AFM cantilever and exposed with the same conditions. An array of letters "WIN" (Waterloo Institute for Nanotechnology) with a line width of 34 nm was successfully patterned on an AFM cantilever, as seen in Figure 3.6.

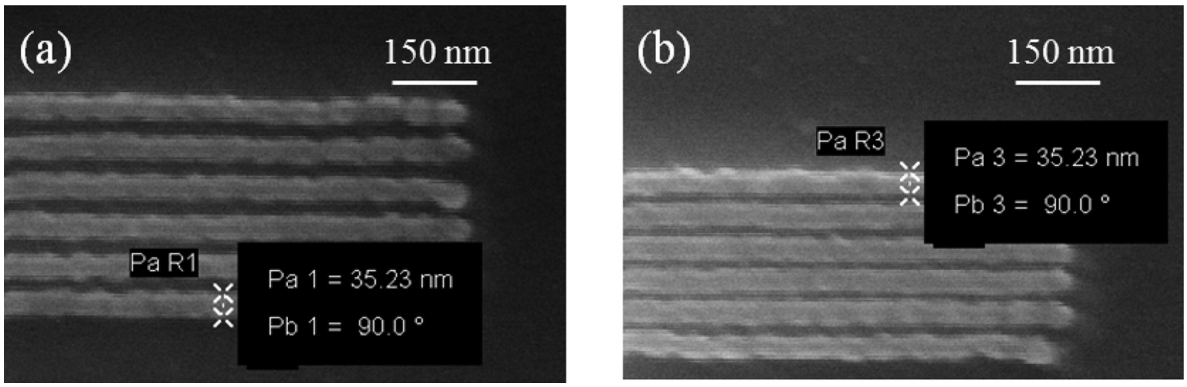

Figure 3.5. Line array patterns with 60 nm (a) and 50 nm period (b) exposed at a line dose of 18.4 nC/cm.

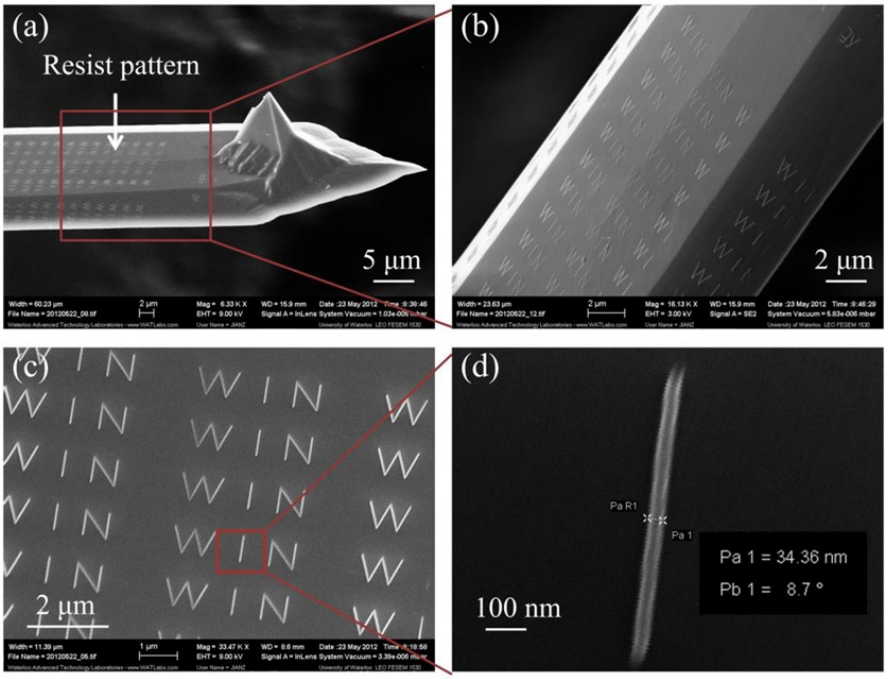

Figure 3.6. SEM images of patterned PS on an AFM cantilever by EBL, taken at increasing magnifications from (a) to (d). The exposed pattern is "WIN", standing for Waterloo Institute for Nanotechnology.

For most applications it is desirable to transfer the pattern from the resist to the sub-layer or substrate. As a proof of concept, a metal (here Al coated by sputtering) pattern are fabricated by

reactive ion etching (RIE) with BCl_3 gas using the resist as mask, and if desired, the pattern can be further transferred into the underlying silicon using Al as a hard mask. The pattern in Al and silicon is shown in Figure 3.7. The star line pattern in Figure 3.7a demonstrated the exposure uniformity along all directions. Figure 3.7b shows the Al "circuit" pattern with a line width of about 60 nm, which was transferred to the Si substrate with a depth of 200 nm, as shown in Figure 3.7c. A high-aspect-ratio (1:20) pattern of the name of our Institute and Group (Waterloo Nanofabrication Group) was achieved by a longer etching time to give a pattern height of 2 μm, as shown in Figure 3.7d.

Recently, nanofabrication on an optical fiber has attracted growing attention in various aspects, such as applications in Bragg gratings,[119] optical filters,[120,121] SERS sensors,[122,123] plasmonic lens,[124,125] and transmission measurement.[126,127] Our process using an evaporated resist can be equally applied to patterning an optical fiber, as shown in Figure 3.7. Evaporated PS on a fiber (cladding layer removed) was exposed by EBL; then the patterns were transferred to an Al layer and fiber (SiO2) by BCl_3 RIE followed by CF_4 RIE for high aspect- ratio structures. Figure 3.7a shows the tilted SEM image of the two-dimensional grating array after CF_4 RIE. With the patterned Al structure as an etching mask, a pattern on fiber having a depth of 270 nm was achieved.

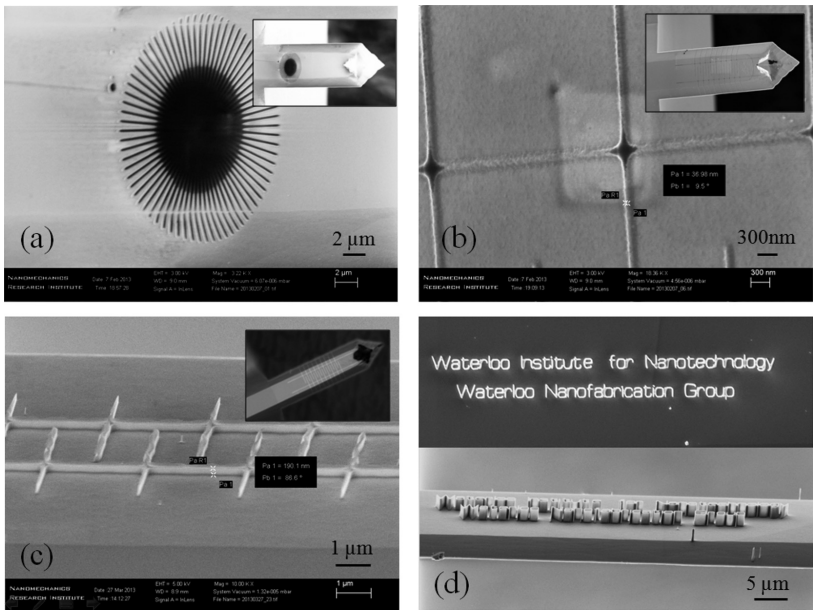

Figure 3.7. SEM images of (a) Al star line pattern, which demonstrated the exposure uniformity along all directions. (b) Al "circuit" pattern with a line width of about 60 nm. (c) Same pattern as (b), after pattern transfer into Si by 1 min RIE for a pattern height of 200 nm. (d) High-aspect-ratio (1:20) pattern of the name of our Institute and Group by 10 min RIE for a pattern height of 2 µm.

Figure 3.8 b&c show a dot array with a diameter of 200 nm and a crossbar array with a line width of 167 nm, both etched into the fiber for 270 nm, respectively. To demonstrate the uniformity along different directions, a star line pattern was exposed and etched into the fiber as shown in Figure 3.8d. Figure 3.9 compares the 2D grating pattern (same sample as Figure 3.8a) on the top and side surface of the fiber. To image the pattern on the top surface, the fiber was mounted on a normal stub, whereas to image the pattern on the side surface (here $\theta = 70^0$ away from the top), the fiber was mounted on a 70^0-tilted stub. As expected, the pattern on the top surface (Figure 3.9a) is well-defined. The pattern on the side surface (Figure 3.9b) has a 70^0 electron beam incidence angle during exposure; thus the structure is tilted by the same angle.

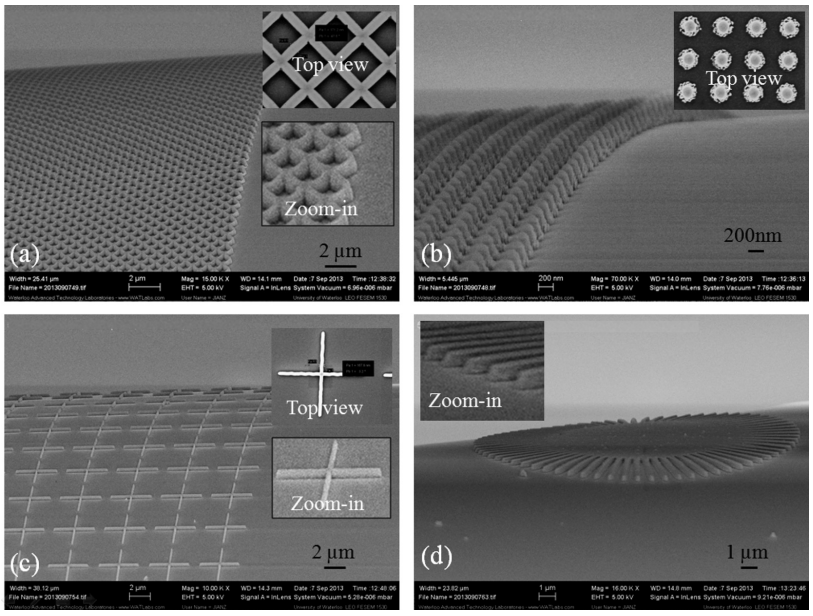

Figure 3.8. SEM images of nanostructures on an optical fiber with a height/depth of 270 nm. (a) 2D grating array with a line width of 167 nm; (b) dot array with a diameter of 200 nm; (c) crossbar array with a line width of 167 nm; and (d) star line pattern. The insets show a top view and/or zoom-in view of the structures. The insets show a top view (pattern on the top surface) and/or zoom-in view of the structures. Except for the top-view images, the wafer piece onto which the fiber was attached was mounted on a 45^0-tilted stub for SEM imaging.

Previously, a similar tilted structure by exposing a wafer mounted on a tilted stub was achieved.[128] Moreover the cross sections of two orthogonal lines are taller than the line sections next to them. This is because the exposure dose is reduced to cos 70^0 = 0.34 x nominal line dose, and thus the lines were greatly underexposed, which led to a shorter resist structure after development. However, the cross sections received twice the exposure, which gave taller resist structures sufficient for the subsequent pattern transfer process. The underexposure at large angle can be compensated through increasing the dose by 1/cos θ. The 2D grating pattern eventually disappeared when θ is too large, which led to too low exposure dose and/or too thin resist film (both dose and thickness are proportional to cos θ if without dose compensation).

For evaporation on a curved surface of an optical fiber, one consequence of the non-uniform

resist thickness is related to the resist sensitivity. For a given development time, positive/negative resist sensitivity increases/decreases with reduced film thickness. Therefore, for a nominal exposure dose varying by 1/cos θ (to maintain the same areal dose along the side surface), when the negative resist on the top ($\theta = 0^0$) of the fiber is properly exposed, the resist on the side would be underexposed or overdeveloped since it is thinner. The degree of underexposure/overdevelopment and the resulting feature size shrinkage strongly depend on the resist contrast. For a resist with reasonably high contrast, such as low Mw polystyrene, the overdevelopment would not cause significant feature size shrinkage because the lateral development toward the more exposed region is very slow.

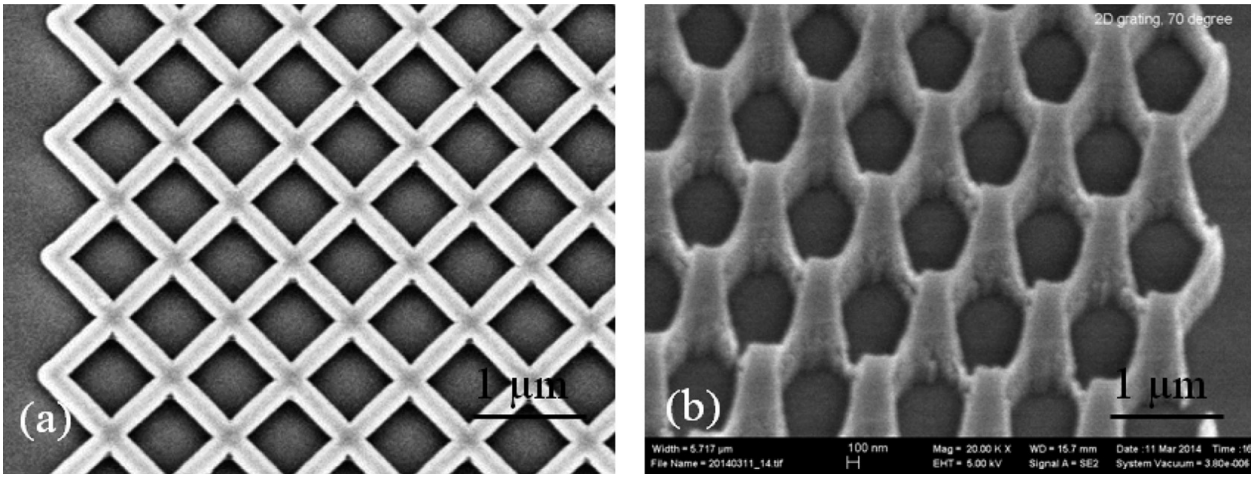

Figure 3.9. SEM images of the 2D grating pattern on a fiber. (a) Perpendicular nanostructure on the top surface ($\theta = 0^0$); (b) tilted nanostructure on the side surface ($\theta = 70^0$). Note that for (b) the fiber support was mounted on a 70^0-tilted stub, and thus the electron beam had normal incidence during SEM imaging.

Unlike an AFM cantilever that has a flat top surface, the side surface of an optical fiber has a circular shape. Thus, the electron beam will be out of focus and distorted away from the top of the fiber surface, where the beam was well focused with minimal stigmation. As a consequence,

the achievable resolution on the fiber side surface depends heavily on the depth of focus (DOF) of the electron beam. The wave nature and diffraction of the electron beam can be ignored when the feature size is well above 10 nm, as is the case for the current work. Then DOF is inversely proportional to the aperture size and proportional to the working distance. A large DOF can be obtained by using a small aperture size such as 7.5 μm, which is the smallest one for the Raith 150TWO system, or using a large working distance such as 20 mm, which is the maximum for the system. However, a small aperture results in a long exposure time because the beam current is roughly proportional to the square of the aperture size, whereas a large working distance makes the exposure more susceptible to electromagnetic and vibrational noise. Therefore, a trade-off between exposure time and achievable resolution on the fiber side surface has to be made. For example, with 37 μm out of focus (fiber radius is 50 μm) and 30 μm aperture size, one can achieve 80 nm resolution on a flat wafer.[129] Moreover, in addition to beam enlargement (here to 80 nm diameter) due to out of focus, the beam spot size on the side surface is further elongated by 1/cos θ (θ is the local incident angle) along the vertical direction.

In addition to DOF, another two important factors for patterning on the side surface of an optical fiber are film deposition and dry etching uniformity. The film thickness for vacuum evaporation is proportional to cos θ, with θ being the incident angle, which is 0 for the top (horizontal surface) of the optical fiber and 90 for the vertical surface. To achieve a more uniform film, one can either continuously and automatically rotate the fiber along its axis during deposition or carry out multiple (e.g., three times) depositions each time the fiber is mounted at a rotated angle (e.g., 60^0). As for the etching uniformity, it is less of a concern because, for dry plasma etching, the etching direction tends to be perpendicular to the local surface with similar ion energy and isotropic diffusion of free radicals to the local surface, which results in a weak dependence of the

etching rate on the incident angle. As a matter of fact, one has to use a Faraday cage[130] or ion sheath control plate[131] in order to etch a tilted (i.e., not normal to the wafer surface) nanostructure, because the self-formed electrical field inside a plasma environment, which determines the ion bombardment and thus the etching direction, is always perpendicular to the sample surface whether the sample is tilted or not.

3.4. Out-of-plane fabrication using evaporated resist

This part has not yet published.

3.4.1. Introduction

Conventional electron beam lithography (EBL) using spin-coated resist is a planar process with the structure formed in the plane of the substrate surface. Previously, out-of-plane or 3D EBL has been realized using rotational stage or low-viscosity resist that can be coated on the sidewall of protruded (out-of-plane) ridges.[100,132] However, the coating is uniform only for ridges aligned with radial direction during spin coating. Polystyrene, an e-beam resist that can be evaporated on non-planar surfaces, can be utilized for patterning on non-planar surfaces of the substrates such as high aspect ratio ridges (walls).

3.4.2. Experiment and results

Fabrication procedure is shown in Figure 3.10. First, high aspect ratio silicon walls were fabricated by EBL. To do this, silicon substrate is cleaned by solvent followed by oxygen plasma etching to remove any organic residues. Then, 200 nm PMMA e-beam resist is spin-coated and annealed for 1 hour at 180 ^{o}C to cure the resist.

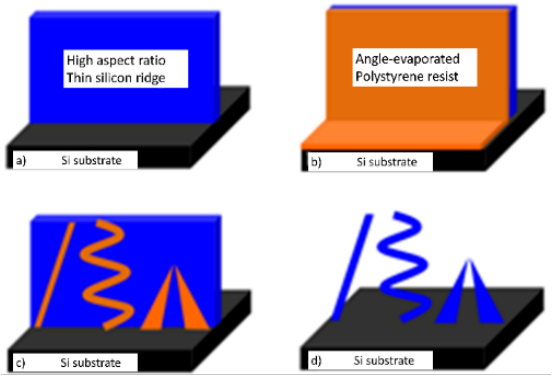

Figure 3.10. Schematic view of out-of-plane nanofabrication process. a) Fabricate high aspect ratio thin silicon nano-wall structure. b) Evaporate polystyrene resist with the wafer tilted at an angle, from one or both sides of the wall; c) Electron beam lithography with the wafer tilted at an angle to expose the resist on the wall; d) Etch through the silicon wall by isotropic RIE using SF_6 gas, and remove the remaining polystyrene by oxygen plasma. Here three structures are shown: tilted pillar, nano-spring and 3D bowtie.

For EBL, Raith 150^{TWO} is used with 20 keV acceleration voltages to create single/periodic lines inside the resist. Upon exposure and development of the resist with MIBK:IPA 1:3 solvent mixture and IPA rinsing, 10 nm Cr metal film is deposited with e-beam evaporation technique. After lift-off process of the resist, metal film is then used as a hard etching mask to fabricate the silicon nanowalls. This is done by dry etching procedure which was non-switching or switching deep silicon etching using SF_6 and C_4F_8 gas. Some of resulted high aspect ratio nanowalls are demonstrated in Figure 3.11.[133,134,135,136,137] These nanowalls with 1:32 aspect ratio are then used as a substrate for out-of-plane fabrication. Similar structure can also be fabricated by conventional low temperature (sub-50^{o}C) KOH etching of (110) wafer that could achieve aspect ratio of over 100.[138]

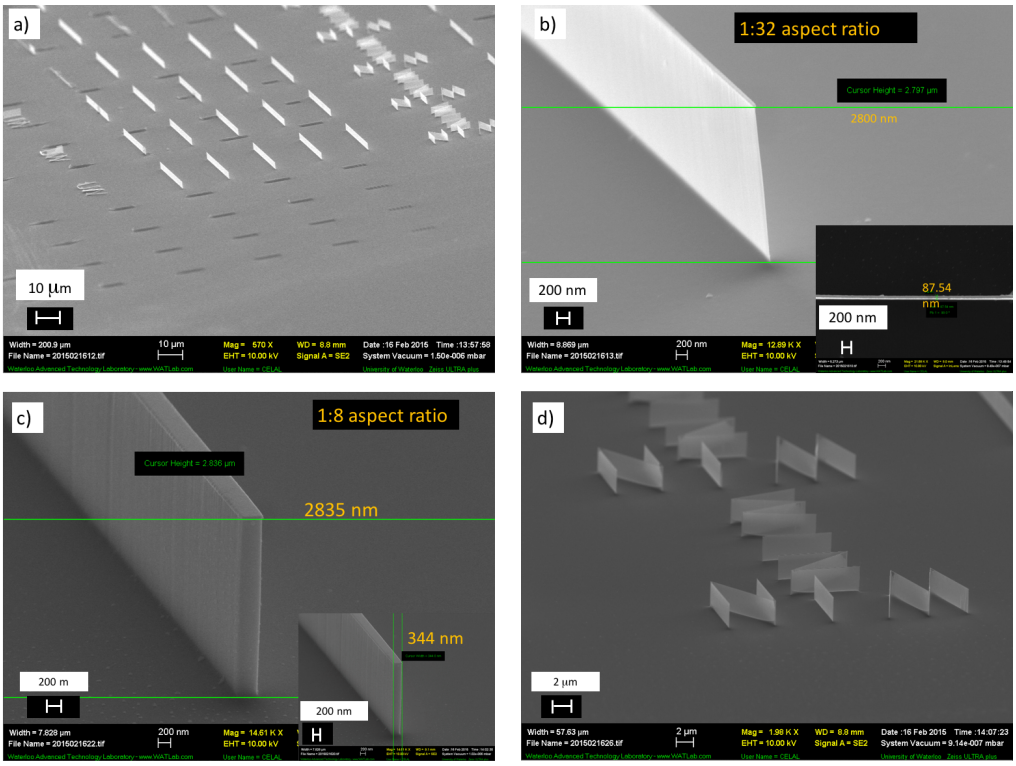

Figure 3.11. SEM images of high aspect ratio silicon nanowalls. a) array of nanowalls, b) nanowall with 1:31 aspect ratio, 87 nm wide, 2800 nm high, c) nanowall with 1:8 aspect ratio, 344 nm wide, 2835 nm high, d) array of WIN (Waterloo Institute for Nanotechnology) nanowalls.

To coat the sides of these walls, polystyrene was then evaporated with the wafer tilted with 60 degrees. Evaporation is done by using thermal evaporation technique where evaporation rate was set to 1 Å/s and the film thickness is 200 nm. Next, using LEO FESEM 1530 system equipped with Nabity pattern generator, EBL was carried out with the wafer tilted, ideally close to 90 degrees, to define the patterns on the wall. After developing the resist with xylene and rinsing with IPA, resulted structures are observed by using SEM. Shown in Figure 3.12, exposure was done successfully both on the planar surface and non-planar surface of the silicon and the wall itself.

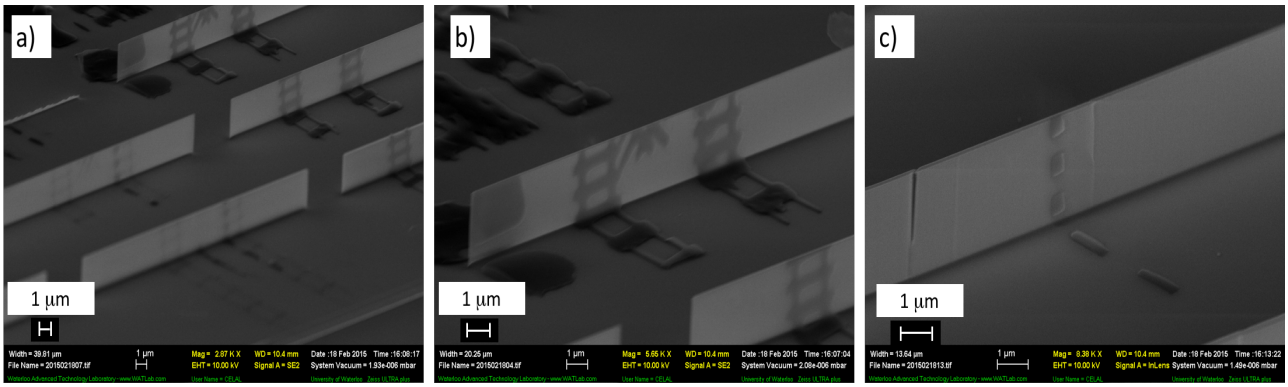

Figure 3.12. SEM images of resulted resist structure on polystyrene resist both on sidewall of the nanowall and the planar surface of the silicon substrate.

Finally, the silicon wall is etched through laterally using isotropic RIE with SF_6 gas (ICP power 50 W, 20V bias, 100 mTorr) that etches silicon and polystyrene at rate of 465 nm/min and 60 nm/min, respectively. Other materials such as gold can be coated onto the out-of-plane patterns to form, for example, 3D bowtie structure for light focusing.

Figure 3.13 shows the completed out-of-plane (as well as in-plane) nanostructures consisting of periodic line and square array patterns, which demonstrates the feasibility of the current process. As can be seen in Figure 3.13 c&e, free standing structures can be fabricated by using polystyrene e-beam resist which can be evaporated on planar/non-planar surfaces by thermal evaporation technique.

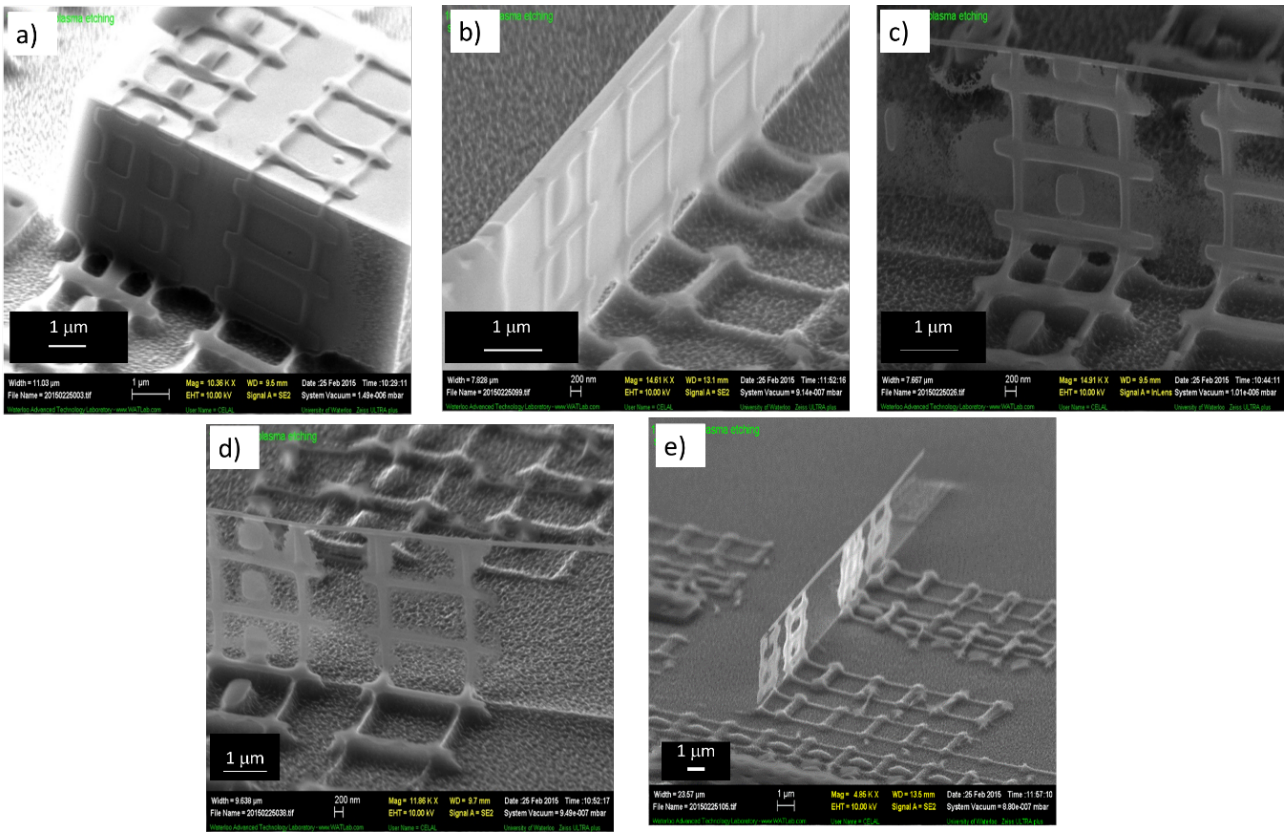

Figure 3.13. SEM images of out-of-plane nanofabrication using polystyrene as a resist, consisting of periodic line and square array patterns with 100 nm line-width resolution.

3.5. Conclusion

In this chapter, it is shown that polystyrene can be thermally evaporated and applied as an electron beam resist on a non-flat, irregular, or fragile substrate. Slight thermal decomposition occurred during evaporation, leading to a reduced molecular weight for the evaporated polystyrene and thus lower sensitivity as compared to the source material. A high resolution of 25 nm half-pitch was achieved using the evaporated resist. As a proof of concept of patterning on irregular surfaces, nanostructures on the AFM cantilever and the optical fiber were fabricated. Moreover, using polystyrene resist, out-off plane nanofabrication using electron beam lithography is made possible.

Chapter 4 Fabrication of high aspect ratio structures on non-planar surfaces using resist containing metal

The following section is based on previously published work[139] by Con C., Zhang J, and Cui B. Nanotechnology **25** (2014) 175301
"**Nanofabrication of high aspect ratio structures using an evaporated resist containing metal**"
Reproduced with permission.

4.1. Introduction

Among all nanolithography techniques, electron beam lithography (EBL), which can generate arbitrary patterns without the need of mask or mold, is the most popular method for R&D as well as for device prototyping and the production of photomask and nanoimprint mold. In typical nanofabrication process using EBL, upon resist exposure and development, pattern transfer is commonly carried out either by direct etch using the resist as mask or by liftoff. The most popular resist, polymethyl methacrylate (PMMA), has a poor plasma etching resistance, thus suitable for liftoff but not for direct etch. The next popular resist ZEP-520A is more resistant to plasma etching than PMMA due to its stable phenyl group, but it is still far from being ideal for pattern transfer by direct etching to fabricate high aspect ratio structure. The same is true for other organic resists including polystyrene (PS), calix[n]arene, ma-N 2403 and SU-8.[112,113,117,140] The popular inorganic resist, hydrogen silsesquioxiane (HSQ), is resistant to oxygen plasma but not to fluorine-based plasma used for etching silicon and its compounds.[43] Other inorganic resists such as metal halide (notably AlF_3) is resistant to plasma etching,[79,80,81,141,142] but its application

is very limited due to its extremely low sensitivity and inability to define structures other than lines and dots.

To pattern deep structures using direct etching method, obviously one can use a very thick resist layer. Yet the resist structure may collapse due to capillary force during rinsing and drying upon development, and the critical dimension (CD) loss may be significant due to lateral etch of the resist structure. Alternatively, an intermediate hard mask layer such as Cr and Al, which can be etched by chlorine-based plasma using the resist as mask, is sometimes employed to etch the sub-layer using fluorine-based plasma. However, this adds extra process steps with increased complexity and cost. As a consequence, it is desirable to use a resist that contains metal and thus has a high dry etching resistance.

Four metal-containing resist systems have been previously demonstrated. Apparently, one can use a resist that contains metal in its chemical structure, such as polyferrocenylsilane (PFS) and its derivatives containing Fe and Si.[82,143] However, besides its low sensitivity and resolution (for PFS, 25 mC/cm^2 and 700 nm, respectively), it is challenging and costly to synthesize such resist. One exception is the recently studied negative resist poly(sodium 4-styrenesulfonate) that is inexpensive and readily available,[144] but its etching resistance is still not high enough possibly because sodium is not an ideal hard mask. The second method is to introduce metal or metal oxide nanoparticles into the resist as a filler, with nanoparticles contents up to 80% that leads to very high dry etching resistance; but the final resolution (and line edge roughness) is limited by the size of the filling nanoparticles.[145] The third method employs the sol-gel process to synthesis the so-called "hybrid organic-inorganic" resist with high content of metal oxide.[146] The main issue is the huge volume shrinkage (e.g. from an initial thickness of 200 nm to a final film of 30-

40 nm) after development and subsequent thermal annealing, which makes critical dimension control difficult and renders it unsuitable for patterning dense structures.

The fourth method, to incorporate metal into e-beam resist, is the sequential infiltration synthesis (SIS) of metal oxide (Al_2O_3) using an atomic layer deposition (ALD) system.[147,148,149,150] In SIS, thin film of resist is infiltrated with Al_2O_3 by alternating exposures to trimethyl-aluminum (TMA) and water in an ALD chamber. Once precursors are diffused into the bulk of the resist layer and chemical reaction with the resist polymer, the resist becomes more resistant to plasma etching. However, in addition to process complexity, the SIS procedure increases line edge roughness and resist swelling, and reduces resist contrast and thus resolution to ~100 nm.

In this work we demonstrate that metal can be incorporated into polystyrene (PS) resist by co-evaporation, which is possible for polystyrene resist since it can be thermally evaporated just like most metals do. PS is an organic negative e-beam resist that offers ultra-high resolution for low molecular weight polymer and ultra-high sensitivity for high molecular weight one. In addition, like PMMA, it is a simple, low-cost polymer with practically unlimited shelf-life. We have previously shown that low molecular weight PS can be thermally evaporated, hence capable of coating onto any irregular non-flat surfaces.[85] Evaporated resist also avoids some issues of spin-coated resist, such as swelling or dissolution if the sub-layer is an organic material, or the edge-bead problem if the wafer is of small size.[115] Since exposed and thus cross-linked PS is difficult to dissolve, lift-off is challenging and direct etching is therefore preferred pattern transfer process. Here we achieved a high dry-etching selectivity of 1:35 to silicon by using the co-evaporated polystyrene-chrome (PS:Cr) composite resist, which was used to pattern high aspect ratio structure on an AFM cantilever. Nanofabrication on irregular non-flat surfaces, such as

AFM cantilever and optical fiber, may find applications in the fields of (AFM) tip enhanced Raman spectroscopy for chemical analysis[151] and lab-on-fiber technology.[90]

4.2. Experimental methods

We chose polystyrene (PS) with molecular weight of 1.2 kg/mol (Scientific Polymer Products Inc.), as it was found that high molecular weight PS decomposed before vaporization and thus did not give a film. We used a thermal evaporator (Intlvac Inc.) to co-evaporate PS and Cr, with the deposition rate individually monitored for each source. Other metals suitable for thermal evaporation, such as Al, can also be introduced to the PS film. PS powder was put inside a boat with holes in the cover of the boat. For Cr evaporation, we used a tungsten wire (R.D. Mathis Company) covered with a thick layer electrodeposited Cr, which allowed a lower evaporation temperature than putting Cr pieces inside a crucible due to the intimate contact of Cr with the heating tungsten wire. As Cr adheres well to the substrate and cannot be removed by the solvent developer, we first evaporated a very thin (20 nm) layer of PS before co-evaporation of the two materials with a total thickness of 200 nm, in order to assure Cr is not in direct contact with the substrate. After co-evaporation with different PS:Cr ratios, electron beam exposure was carried out using Raith 150^{TWO} system with 5 keV acceleration voltages and 0.2 nA beam current. Development was carried out by 1 min soaking with xylene in an ultrasonic bath, followed by 2-propanol (IPA) rinsing. Ultrasonic agitation helped to dissolve the unexposed composite resist that is more difficult to dissolve than pure PS resist. For pattern transfer into the underlying silicon, we used Oxford Instruments ICP380 dry etching system with a non-switching process (22 sccm SF_6 and 38 sccm C_4F_8, 10 mTorr, 1200 W ICP power and 20 W RF power, etching rate 370 nm/min),[133,135] though a Bosch process with a very short cycle time may also be employed to etch high aspect ratio silicon nanostructures.[134]

4.3. Results and discussion

Figure 4.1 shows the contrast curve measured by atomic force microscope (AFM) for the evaporated PS-Cr resist as well as for the pure (no Cr) evaporated polystyrene resist. The two curves followed each other well, implying the incorporation of Cr did not affect significantly resist property due to its low concentration. The volume ratio of PS and Cr was controlled by the quartz crystal thickness monitor for each source, and is here 15:1, leading to a weight ratio of ~2:1 (Cr density 7.2 g/cm^3, polystyrene 1.0 g/cm^3), or roughly one Cr atom per PS monomer. However, Cr would not distribute uniformly in the PS matrix and a certain degree of phase-separation is expected. Right after the "gel point" (the dose where the contrast curve starts to rise), the slope of the contrast curve for the resist containing Cr is more abrupt than pure PS; and this may be because the Cr-enhanced PS is more difficult to dissolve once cross-linking occurs. The contrast for the PS-Cr resist is 11.9 that is a very high value. However, the sensitivity is around 2000 μC/cm^2, which is very low due to the low molecular weight, as for simple cross-linking resist its sensitivity (μC/cm^2) is inversely proportional to molecular weight (kg/mole) according to the Charlesby theory[152]. The sensitivity is lower than spin-coated resist of the same molecular weight, presumably because the evaporated resist has actually lower molecular weight than the source material due to thermal decomposition.

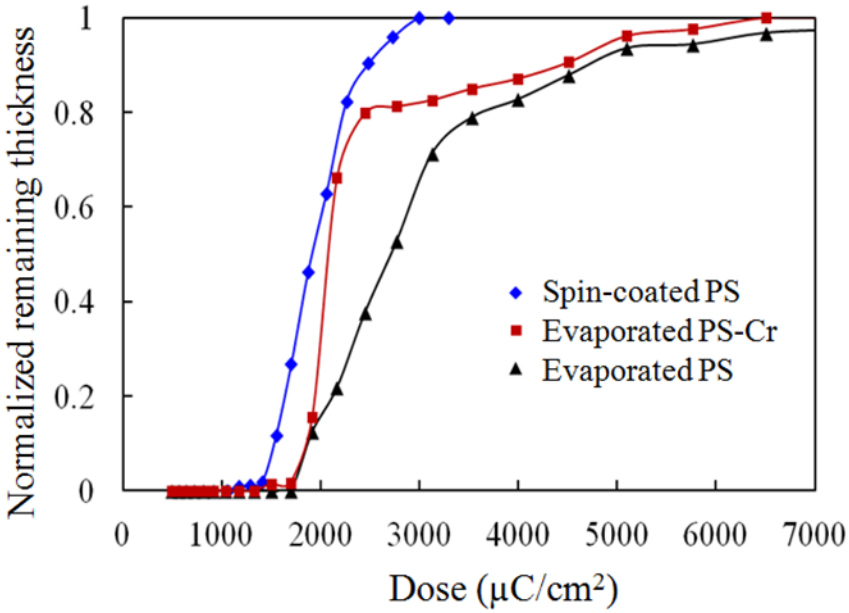

Figure 4.1. Contrast curves exposed at 5 keV and developed by xylene for spin-coated polystyrene with molecular weight of 1.2 kg/mol, co-evaporated Polystyrene-Cr and evaporated (pure) polystyrene (source material with molecular weight 1.2 kg/mol).

With a high contrast, the PS-Cr resist is capable of achieving high resolution. Figure 4.2 shows a pillar array with diameter 55 nm exposed in PS-Cr resist at 5 keV. Smaller pillar diameters (down to 30 nm, not shown) could be defined, but the pillars (200 nm height, aspect ratio 6.7:1 for 30 nm diameter) all collapsed due to capillary force during drying the rinsing solvent.

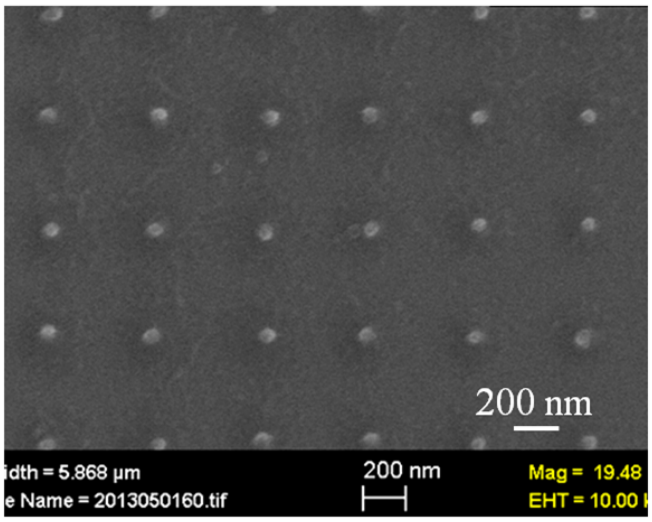

Figure 4.2. Pillar array exposed in PS-Cr resist by electron beam lithography at 5 keV and developed using xylene for 1 min. The pillar diameter is 55 nm and height 200 nm.

The metal-containing resist structure was used as mask to transfer the pattern to the silicon substrate by ICP-RIE with C_4F_8 and SF_6 gases. As seen in Figure 4.3a-b, silicon structures of high aspect ratio of 35:1 was obtained. Our measurement on blank film showed an etching rate selectivity between silicon and PS-Cr (15:1 volume ratio) resist of 1:33, compared to 1:2.6 for pure PS under the same etching condition. Thus the incorporation of Cr into polystyrene improved its etching resistance by one order. One major advantage of evaporated resist, as compared to spin-coated resist, is its capability of coating on irregular non-flat surfaces. As a proof of concept, we coated PS-Cr resist onto an AFM cantilever, and followed the same lithography and pattern transfer procedure. The high aspect ratio silicon structure patterned on AFM cantilever is shown in Figure 4.4a-c. It would be straightforward to employ the same process to other non-flat surfaces, such as the side or end of an optical fiber for photonics application.[115,153] Compared to focused ion beam milling that is also capable of patterning on irregular surface, EBL using evaporated resist is faster (since electron beam can be well focused even for nA beam current, which is not the case for Ga ion beam), and free from Ga contamination.

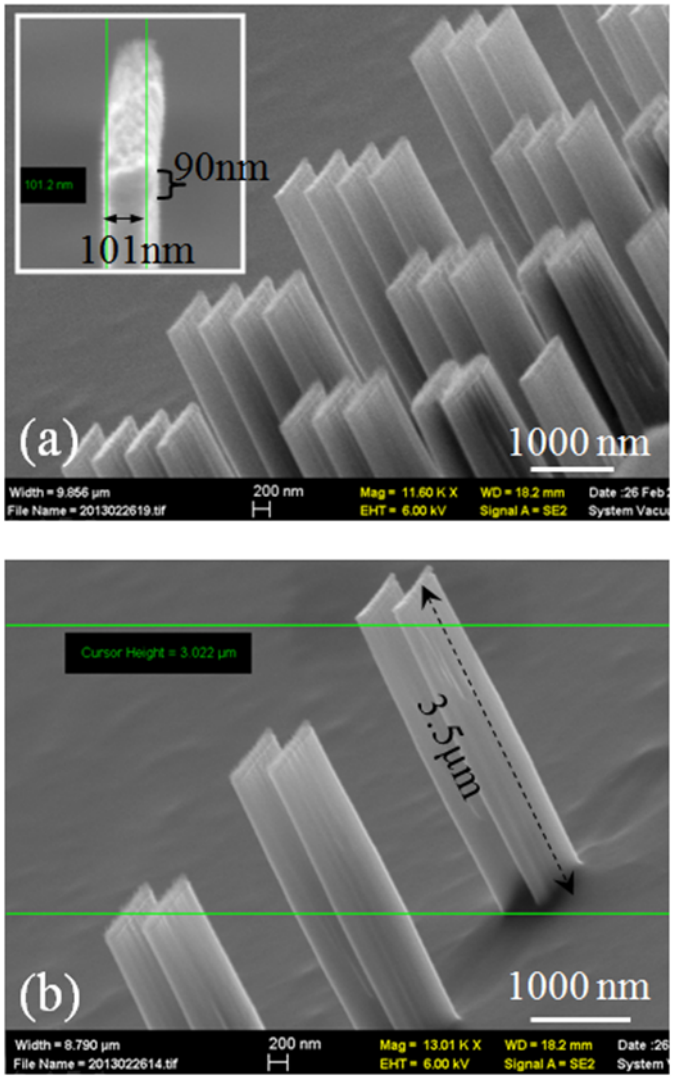

Figure 4.3. SEM images of high aspect ratio silicon structures patterned by EBL using PS-Cr resist and ICP-RIE. The width of the short lines is about 100 nm and height 3.5 µm. The remaining PS-Cr mask is 90 nm as shown in the insert of (a).

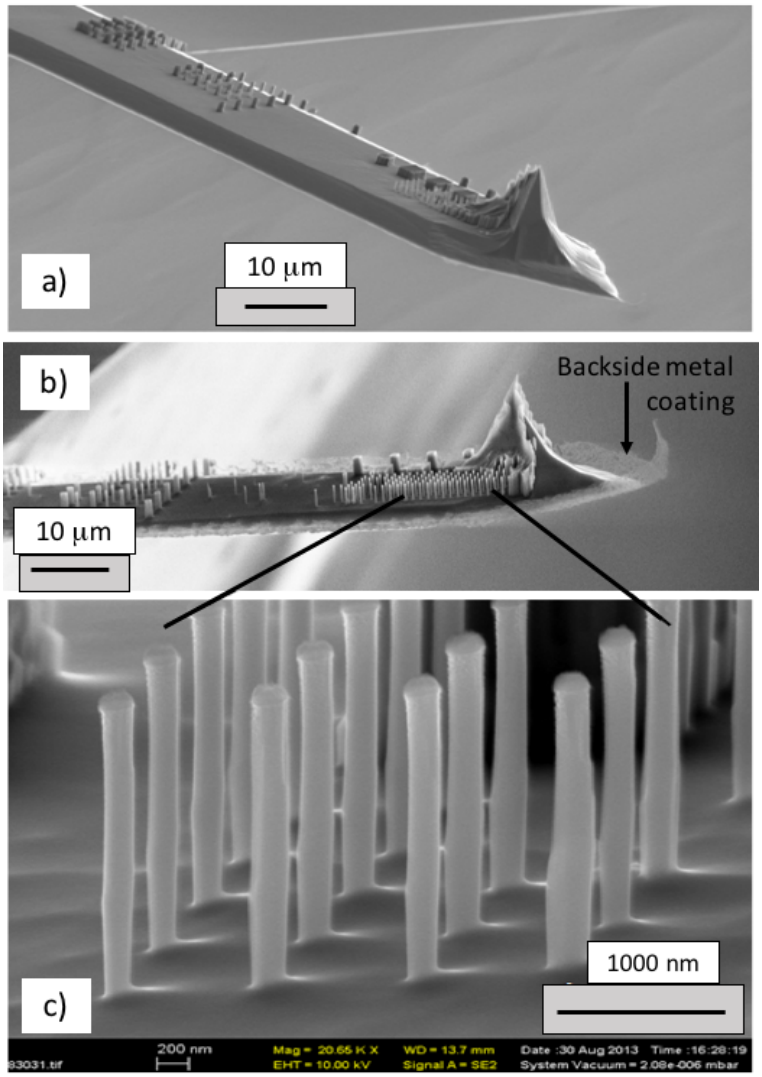

Figure 4.4. SEM images of high aspect ratio silicon structures patterned on AFM cantilever. (a-b) Images taken at low-magnification for two AFM cantilevers; (c) Zoom-in of the silicon pillar array in (b).

4.4. Conclusion

To improve dry etching resistance of polymer resist, here we showed that metal can be incorporated into PS resist by co-evaporation of the two materials onto a substrate. With a volume ratio of 1:15 between Cr and polystyrene, this nanocomposite resist showed an etching selectivity to silicon one order higher than pure polystyrene resist. Its contrast was also higher than pure PS resist by thermal evaporation. Silicon structures of 100 nm width and 3.5 μm height

(aspect ratio 1:35) were obtained using a non-switching deep silicon etching recipe with SF_6 and C_4F_8 gases. Moreover, as evaporated nanocomposite resist can be coated onto irregular and non-flat surfaces such as optical fiber and AFM cantilever, we demonstrated the fabrication of high aspect ratio structures on top of an AFM cantilever. Nanofabrication on non-flat surfaces may find applications in the fields of (AFM) tip enhanced Raman spectroscopy for chemical analysis and lab-on-fiber technology.

Part II Fabrication methods of dense surface nanostructures

Chapter 5 Dense nanostructures without long-range ordering: properties and low-cost fabrication

5.1. Introduction

Recently, micro- and nano-structured surfaces have become a hot topic in nanotechnology where performance of devices is enhanced due to surface nano-structuring. Such structures are often called "smart" coatings where they could provide enhanced functionalities such as wetting/de-wetting, adhesion, thermal and/or electrical conductivity, super-hydrophobicity, self-cleaning, anti-icing, anti-reflectivity, anti-fogging, capability to direct cell growth, and gas barrier properties.[154,155,156,157] Those functions can be generally attained using dense nanostructures (notably pillars and holes) without long range ordering. Therefore, the costly top-down lithography methods such as electron beam lithography are not needed; instead, the various low-cost self-assembly methods are ideal since self-assembly processes usually lead to dense pillar or hole structures without long range ordering, over large surface area and within a short time. Hence, fabrication of surface nanostructures, or often described as surface nano-texturing, attracted great attention in recent decades.[158] This chapter will first introduce the functions offered by such nanostructured surface, and then give an overview of the various self-assembly/self-formation methods suitable for the fabrication of such nanostructures at low cost. Next chapter (Chapter 6) will present our self-assembly method using metal salt-polymer composite materials and its application for anti-reflection and super-hydrophobic surface.

5.2. Properties of surface nanostructures

5.2.1. Wetting/hydrophobicity

Nature offers a large variety of surfaces with those types of structures with amazing properties. For instance, when rain drop is in contact with the surface of lotus leaves, it rolls off the surface without wetting it since leaves have such surface with super-hydrophobic or self-cleaning coatings/texturing.[156] Those leaves are composed of micro- and nanostructures covered with a hydrophobic wax, where water droplets attain a quasi-spherical shape. Hydrophobicity, physical principle occurring at substrate surface with the presence of liquid, is normally characterized using contact angle measurements, as shown in Figure 5.1. Generally speaking, when a liquid droplet contacts on a solid substrate, it will remain either as a droplet or spread out on the surface to form a thin liquid film. Hydrophobic layers commonly have contact angles below 120^{o} and above 90^{o}, and surfaces providing larger contact angle are called super-hydrophobic surface.[157]

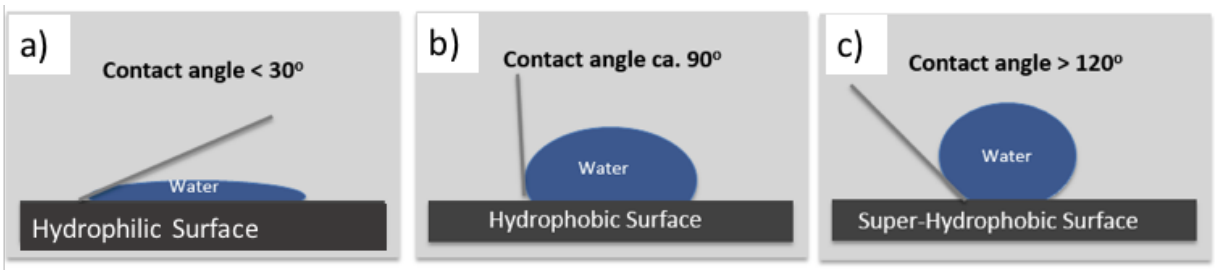

Figure 5.1. Contact angle measurement and comparison of a) hydrophilic, b) hydrophobic, and c) super-hydrophobic surfaces.

To fabricate this kind of surface, one needs to texture the surface with sub-micron sized structures which will increase the amount of air trapped within the pores, and should apply chemical coatings to lower the surface energy of the substrate. One work was recently achieved by Checco et al. using block copolymer lithography (BCPL) followed by dry & wet etching to

get tapered profile on silicon structures, as shown in Figure 5.2, where contact angle is observed to change from 150° to 165° depending on the profile of the pillars, compared to 112° with chemically identical flat samples (Figure 5.2.e).[159]

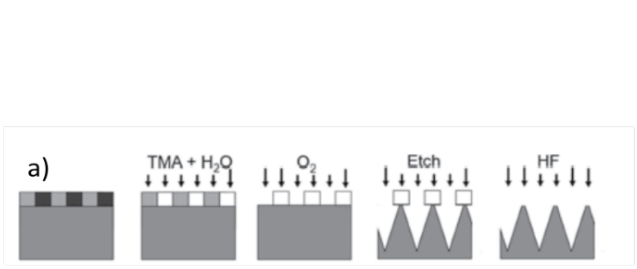

e)

Surface Texture	Spacing (±1 nm) [nm]	Feature height (±5 nm) [nm]	θ_{adv} (±2°) [°]	$\Delta\theta$ (±3°) [°]
Flat	NA	NA	112	6
52 nm spaced pillars	52	180	150	30
30 nm spaced pillars	30	75	137	27
52 nm spaced cones 1	52	75	165	5
52 nm spaced cones 2	52	180	165	6
30 nm spaced cones	30	95	162	7

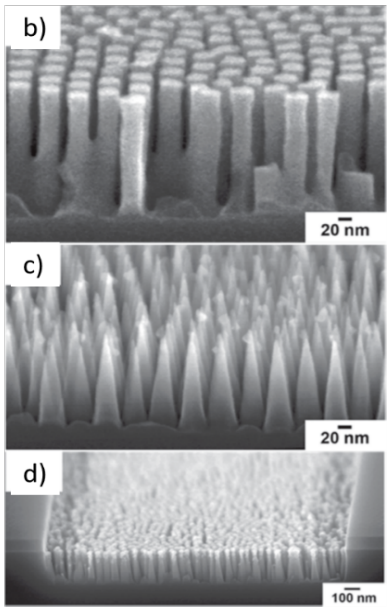

Figure 5.2. a) Fabrication process of super-hydrophobic surface structures by block copolymer lithography using PS-b-PMMA block-copolymer film, b-d) SEM images of created pillars with different tapered profile, and e) measured contact angle values with respect to pillars formed. Contact angle values change from 150° to 165°. [159]

Such example of application areas includes non-adhesive surfaces for micro-devices, microfluidics, glass coatings, anti-bouncing additives for pesticides, and environment-friendly self-cleaning underwater surfaces, etc.[160]

5.2.2. Adhesion

Adhesion properties of surface nanostructures on the foot of insects and reptiles enable them to be able to move on vertical walls, and such bio-inspired structures are used in robotics, medical bandages, material gripping, household products, and biomedical devices, etc. [161,162,163,164] These adhesive structures generally consist of arrays of angled branching hierarchical fibers with spatula-shaped tips, as shown in Figure 5.3.[156] The structures with large aspect ratios provide

millions of small contact points to the species, and hence enable them to adapt to both rough and smooth surfaces. It is reported that the physical forces behind this adhesion are van der Waals forces with possible combination of capillary forces.[165,166,167]

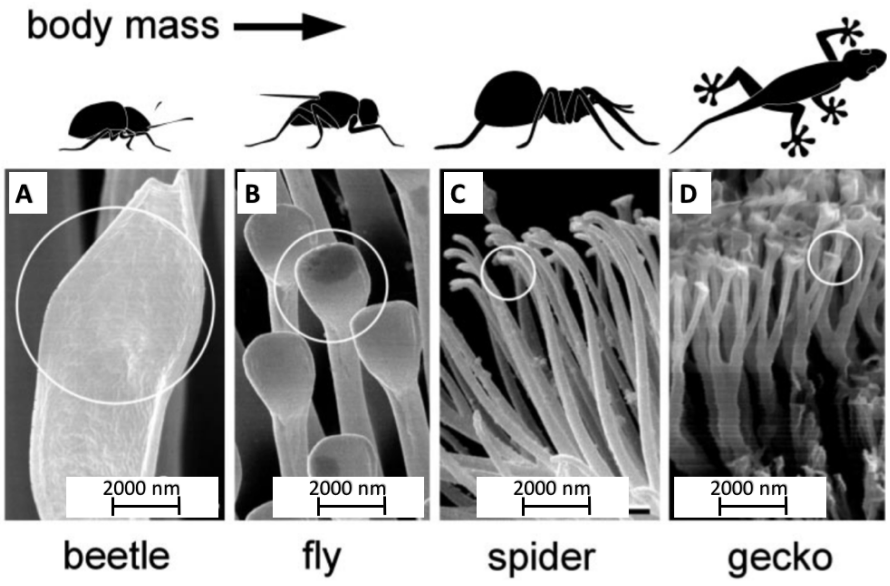

Figure 5.3. Terminal elements (circles) in animals with hairy design of attachment pads. SEM images of the hairy attachment pads of several animals: a) beetle, b) fly, c) spider, and d) gecko. Note that heavier animals exhibit finer adhesion structures.[156]

Recently, mimicking those structures attracted great attention. Yao et al. reported numerical modelling of pads mimicking the gecko's foot, and found that the adhesion strength of a strongly anisotropic attachment pad exhibits essentially two levels of adhesion strength depending on the direction of pulling, resulting in an orientation-controlled switch between attachment and detachment.[168] By using modelling and advancements in fabrication tools, wall-climbing robot, called 'Stickybot', is developed that uses directional adhesive feet.[162,163]

5.2.3. Anti-reflectivity

Another common application of these surface nanostructures comes from their anti-reflective properties. In nature, the most famous example is the moth eye, as shown in Figure 5.4a-d,

where the eye itself is equipped with a quasi-periodic array of sub-wavelength structures (Figure 5.4d). This makes the insect's big eyes appear lusterless while they are inactive during daytime thereby disguising from predators.[169] It is seen that those eyes exhibit curvilinear surfaces, as shown in Figure 5.4b, where hexagonally packed convex micro lenses focus light onto the internal photoreceptor cells.

Clapham et al. discovered that the anti-reflective property of these nanostructures comes from the effective gradual change of the refractive index between air and the cornea surface.[170] In short, light transmittance increases through the eye, which enhances the omnidirectional anti-reflective property.[171,172,173]

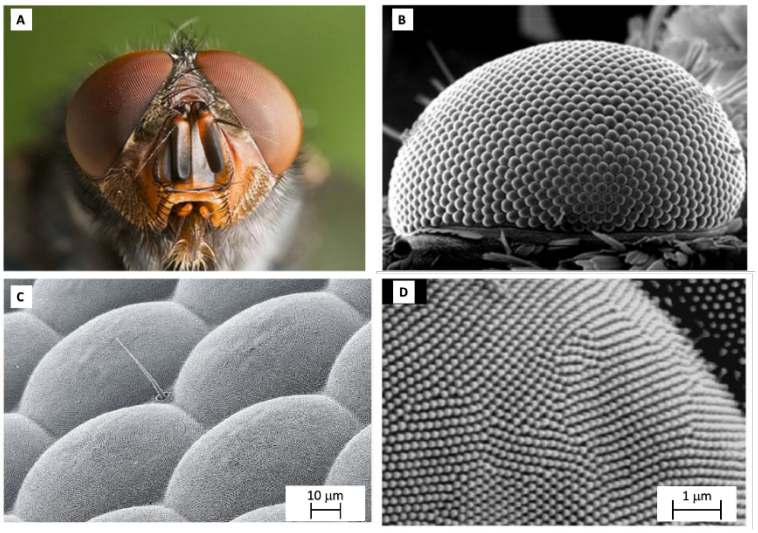

Figure 5.4. (a) Image showing the lusterless eyes of a moth, (b) SEM image of a compound eye showing a curvilinear array of micro-lenses, (c) SEM image of the facet micro-lenses called *ommatidia* arranged in a hexagonal lattice, (d) High magnification SEM image of the *ommatidia* showing the close-packed anti-reflective nanostructures that reduce the reflection of light.[169]

Interaction of light with the medium will be different between macro and nanoscales, as illustrated in Figure 5.5. Incident light will be reflected, scattered and absorbed on macrostructures (Figure 5.5b). However, when light is incident on the nanostructures where

feature size is smaller than wavelength, structures will appear as an interface with a gradual transition in effective refractive index. Depending on the dimensions of the structures and the wavelength of the light, reflection of the light is decreased and transmission is increased when the wavelength is larger than the period of those nanostructures. It is also reported that moth-eyes have the optimal anti-reflection conditions using two-dimensional sub-wavelength structures.[174,175] To obtain anti-reflection property of any array of nanostructures, relationship between wavelength (λ) of the incident light and the periodicity (p) and the height (d) of those structures should meet the following condition:

$$d > \frac{\lambda}{2.5} \; and \; p < \frac{\lambda}{2} \tag{9.1}$$

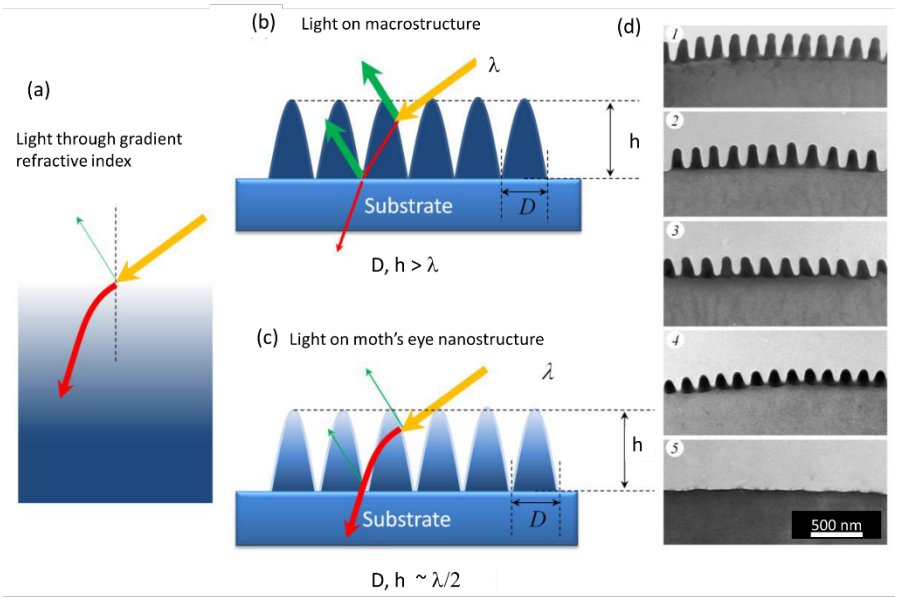

Figure 5.5. (a) An illustration showing the light path through a gradient refractive index medium based on Rayleigh's theory. (b) Light reflected or scattered from a macrostructure. (c) If dimensions of the structures are comparable to half the wavelength of light, light would see the structures as an effective medium with a gradient index profile. (d) Anti-reflective nanostructure in eyes of other species such as the nymphalids *Bicyclus anynana* and *Polygonia c-aureum* (*1,2*), the pierid *Pieris rapae* (*3*), the lycaenid *Pseudozizeeria maha* (*4*) and the papilionid *Papilio xuthus* (*5*).[169]

Recently, anti-reflective surfaces have found many applications such as in solar cells, electro-optical devices, lenses, displays, and imaging systems.[176,177,178] For silicon-based solar cells, it is reported that more than 30% of incident light is reflected back from the surface.[179,180] Hence, anti-reflective coatings (ARCs) are required. Such coating was initially done by coating an extra layer on cells with a thickness of quarter wavelength. However, those coatings resulted in two major problems: the minimum reflectance only happens at single wavelength and then gradually increases as the wavelength deviates from λ^2_{min}; the adhesion and thermal stability of the ARC is generally unsatisfactory due to the mismatch of material properties between silicon and the ARC layer.[177,179,181] Hence, using surface nanostructures as an alternative solution to ARC films is an effective way to obtain reduced reflection.

So far, several types of surface nanostructures have been investigated and developed for anti-reflection properties that can achieve less than 2% reflectivity[182] using lithography techniques including top-down and bottom-up fabrication procedures which will be discussed in the following section.

5.3. Low-cost fabrication of surface micro-nano structures

5.3.1. Self-formed surface nanostructures by wet and dry etching

Creating surface nanostructures does not mean only building nanopillar, hexagonal arrays, etc. it also means nanoporous surfaces. Porous silicon created via electrochemical etching of silicon in hydrofluoric (HF) solution is also used in surface texturing for solar cell applications since 1970s.[183,184,185] By controlling the HF ratio, etching time, applied current density, or using mixture of different acids and hence changing the pore size and the volume, the density of the pores can be modified for better result. In another way, as shown in Figure 5.6, structures of

pyramidal shape of silicon is achieved by basic solutions such as potassium hydroxide (KOH) and sodium hydroxide (NaOH) solutions where reflectivity can be reduced to 12.5%.[186,187,188]

In order to increase the efficiency of the porous surfaces, noble metals such as gold (Au), platinum (Pt), and silver (Ag) nanoparticles can be used to assist HF based solution etching, whch is called metal assisted chemical etching (MacEtch).[182,189,190] In this way, creating high aspect ratio silicon nanowires is fabricated where less than 1.4% reflectivity is measured with single crystal silicon nanowire sample.[182]

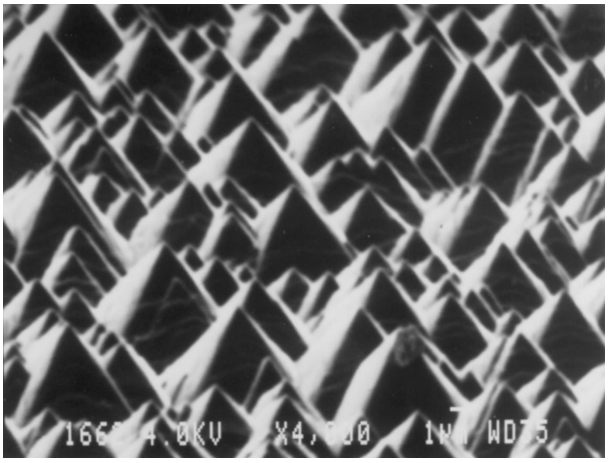

Figure 5.6. Textured silicon surface with 100% pyramid density via NaOH.[187]

Besides wet etching, another way of doing maskless etching is using dry plasma etching.[191,192] Ha et al. developed a process in which mixture of hydrogen (10%) and argon (90%) gases were utilized for creating pyramid-shaped Si nanostructures.[176] In order to enhance the anti-reflection property, upon getting pyramid-shaped structures, 1 μm thick poly(dimethylsilexone) (PDMS) is casted on top of those structures. Resulted reflectivity is measured by less than 10 % in ultraviolet and visible region, as shown in Figure 5.7.[176] In this process, gas flow rates are changed while chamber temperature is changed from 1100 to 1350 ^{o}C. This high temperature annealing process plays a key role as annealing of silicon weakens the bonds between Si atoms

under hydrogen environment. As a result, SiHx free radicals are formed easily through the reaction with hydrogen gas, and resulting both etching and re-deposition of silicon to give the pyramid-shaped silicon.

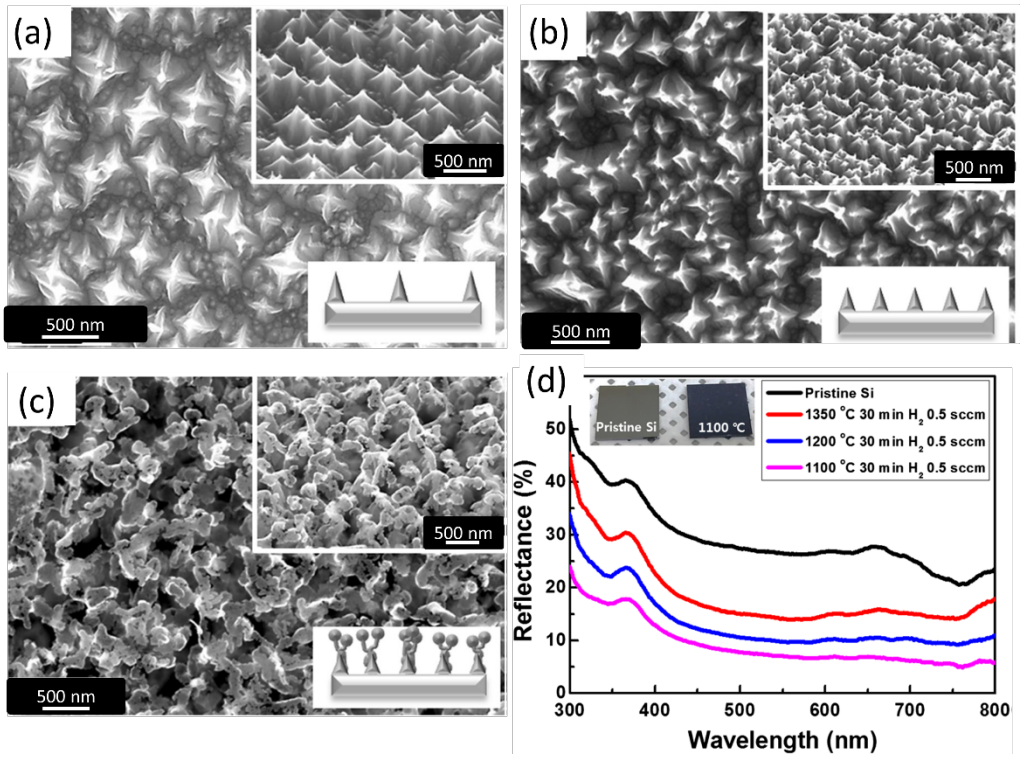

Figure 5.7. SEM images and schematics of the Si nanostructures. Etching done at (a) 1350°C, (b) 1200°C, and (c) 1100°C. Insets: tilted SEM images and schematics of the Si nanostructures. d) Measured reflectance spectra of the fabricated Si nanostructures. Inset: optical image of the pristine Si and Si nanostructure etched at 1100°C.[176]

Recently, Gogolides et al. described how plasma–chamber wall interactions in etching plasma leads to either random roughening/nanotexturing of polymeric and silicon surfaces, or formation of organized nanostructures on such surfaces.[193] In this work, using a high-density helicon plasma reactor and oxygen gas at certain pressure and temperature, they reported texturing of polymers such as PMMA surface, as shown in Figure 5.8. As their process requires specific

equipment and conditions such as etching tool, alternative to this method, a thin layer of metal deposition can be used to create nanosized structures on the surface by annealing, and such a metal nanostructure can be used as a hard etching mask to etch the under-layer.[194,195]

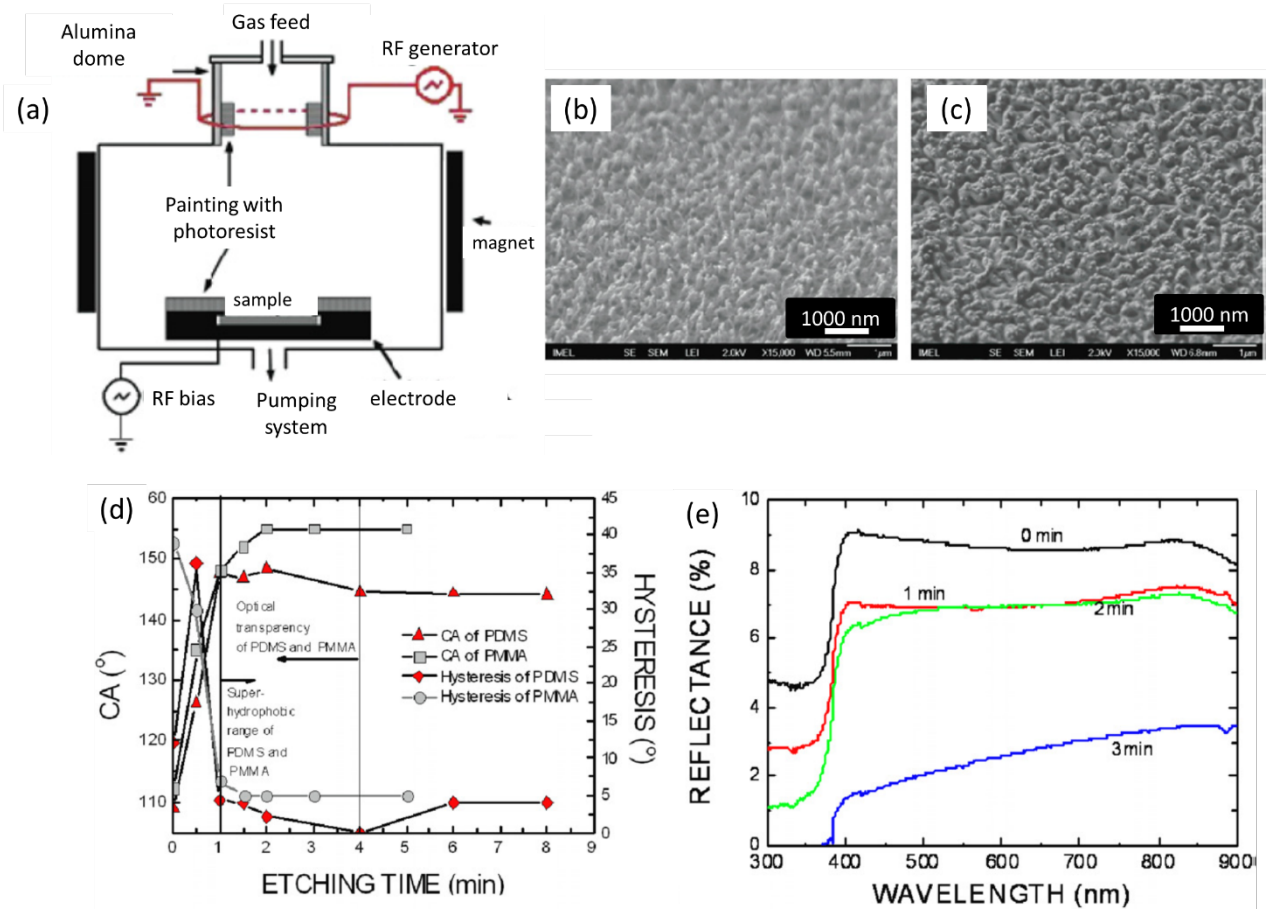

Figure 5.8. Plasma nanotexturing of PMMA in O_2 and the role of reactor walls. The z-axis shows the range of height values in each image. (a) Schematic view of the MET helicon reactor showing the positions of "painting" with photoresist polymer on the walls in order to reduce wall material sputtering. (b) Wall condition 1 for PMMA film etched for 2 min. The SEM image shows the morphology of a polymer film and the roughness formed. c) Wall condition 5 for PMMA film etched for 2 min. d) Contact angle (CA) and CA hysteresis versus etching time for PDMS and PMMA. The evolution of super-hydrophobicity and the process window for optical transparency are also indicated. (e) Reflection spectra (at 6^o) of 2 mm PMMA substrates before and after 1, 2, 3 min O_2 plasma processing on one side of the polymer plate.[193]

5.3.2. Sol-gel processing

Sol-gel processing has been in use for ARC since 1960s where dip-coating and spin-coating are used to coat the film.[169] The precursor used in the process is prepared by mixing metal organic compound in an organic solvent. In dip-coating method, the substrate is immersed into a precursor solution (sol-gel) and withdrawn at a controlled speed, whereas spin-coating involves the rotation of the substrate with a precursor dispersed on the substrate surface, followed by gelation during the evaporation of the solvent as shown in Figure 5.9.[196,197] After coating, a final heat treatment is applied on the coated film in order to transform the coated layer into metal oxide or fluoride (depending on the precursor) and remove the organic by-products present in the film. Recently, using this approach, Walheim et al. reported formation of porous ARC layer inside PMMA-PS mixed polymer film that enables 99.7% transmittance of the light in visible region.[198]

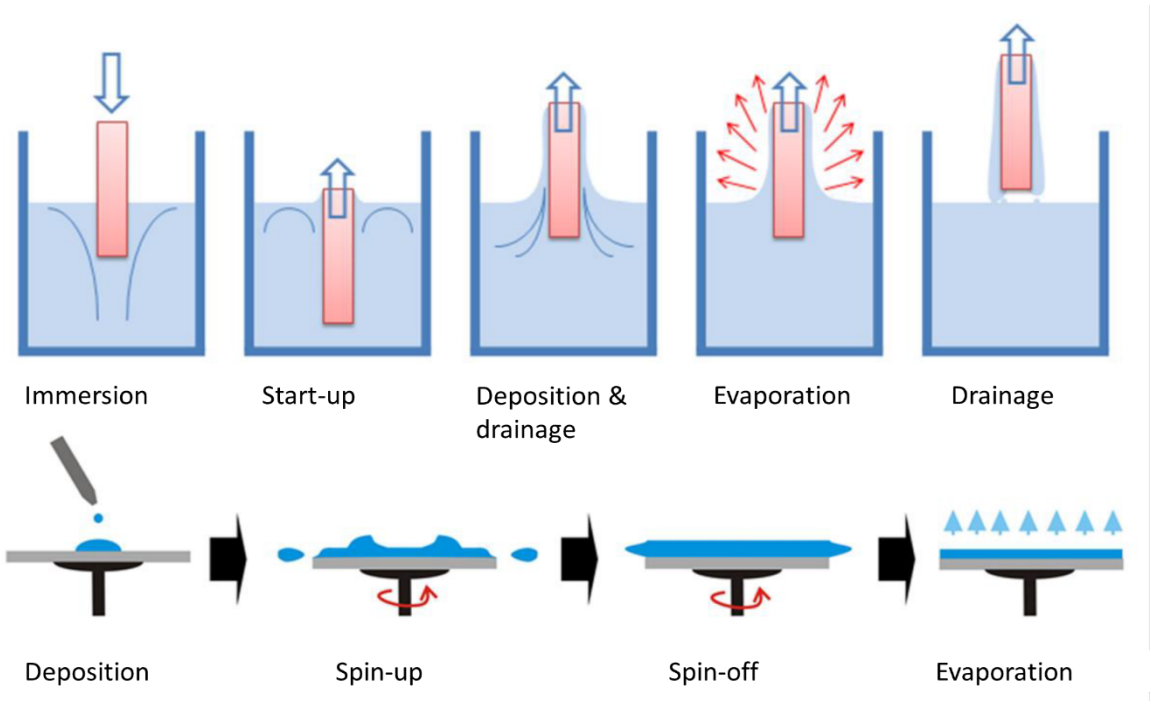

Figure 5.9. Process steps involved in sol-gel coating of glass using (top) dip-coating and (bottom) spin-coating.

5.3.3. Vapor deposition

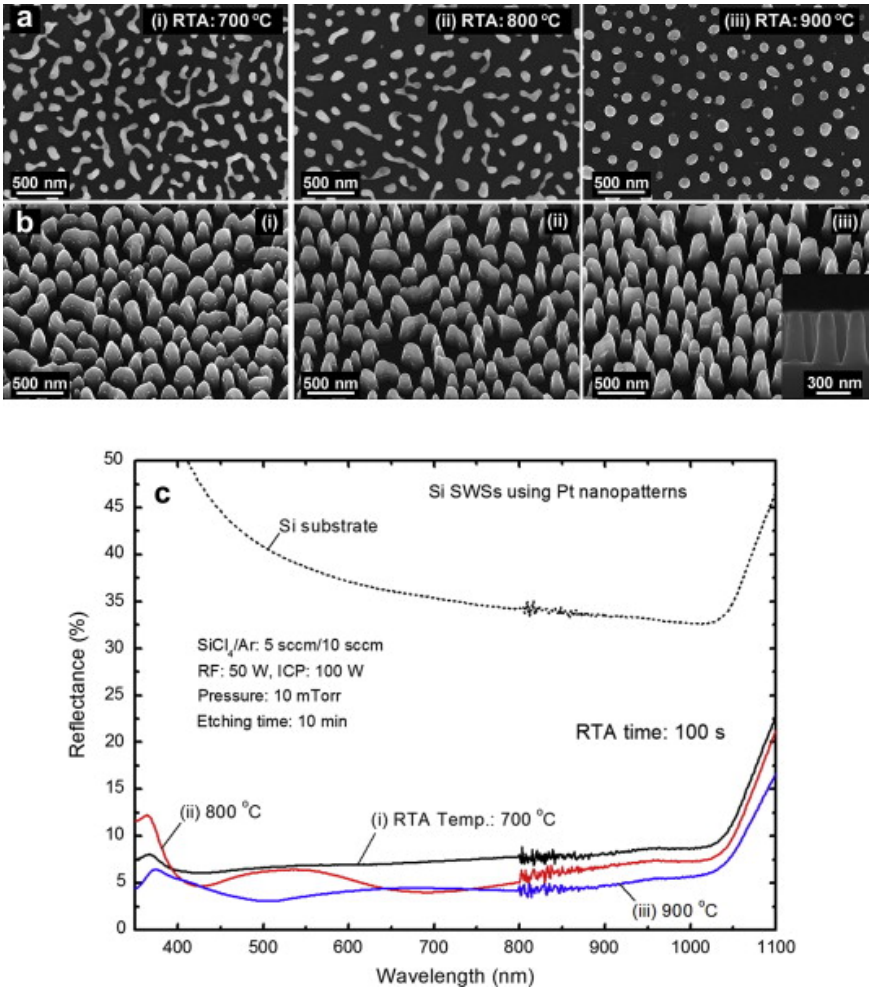

Figure 5.10. SEM images of (a) the thermally dewetted Pt nanopatterns after rapid thermal annealing (RTA) at different temperatures of (i) 700 °C, (ii) 800 °C, and (iii) 900 °C for 100 s, and (b) etched Si subwavelength structures (SWSs) by ICP etching, and (c) measured reflectance spectra of the corresponding Si SWSs. [199]

In order to fabricate ARC layer formed from the surface nanostructures or porous surfaces, metal film deposition on a substrate is also utilized. For this process, thin metal films are thermally annealed in order to form sub-micron sized nano-islands on the substrates that can be used as hard mask for etching the substrate. Recently, Leem et. al. reduced the reflectance of structured silicon to 5% over a wide wavelength range of 350–1030 nm (Figure 5.10).[199] These structures

were patterned by using 5 nm Platinum (Pt) film as an etching mask where they are heated up to 900 ^{o}C to get desired nano-islands of platinum, as shown in Figure 5.10 a-b.

Alternatively, plasma enhanced chemical vapor deposition (PECVD) and other chemical vapor deposition (CVD) techniques can be used to create surface nanostructures. To fabricate, for instance, nitride-based ARC layer such as silicon nitride (SiNx:H) coatings on textured silicon solar cells, PECVD is a commonly used technique where nitride coatings function both as an ARC and surface passivation layer for Si solar cells.[169,200] In PECVD, thin film is deposited on the substrate where a vapor state of reacting gases turn into a solid state on the substrate.

A new fabrication technique called glancing angle deposition (GLAD) uses evaporation technique to generate films with low densities, high pore density and hence low reflectivity.[201,202,203] In GLAD, as shown in Figure 5.11, vapor flux is deposited on a rotating substrate with a tilted incident angle that allows the thin film to grow with a gradually decreasing density or high porosity.[204] Besides PVD, CVD is also used to fabricate nanostructures for anti-reflecting properties, such as GaN nanotubes and carbon nanotubes.[205]

Lastly, cesium chloride (CsCl) film can be thermally evaporated to form nano-islands as etching mask upon exposure to humidity after film deposition, which is used to enhance the efficiency of hybrid solar cells.[169,206]

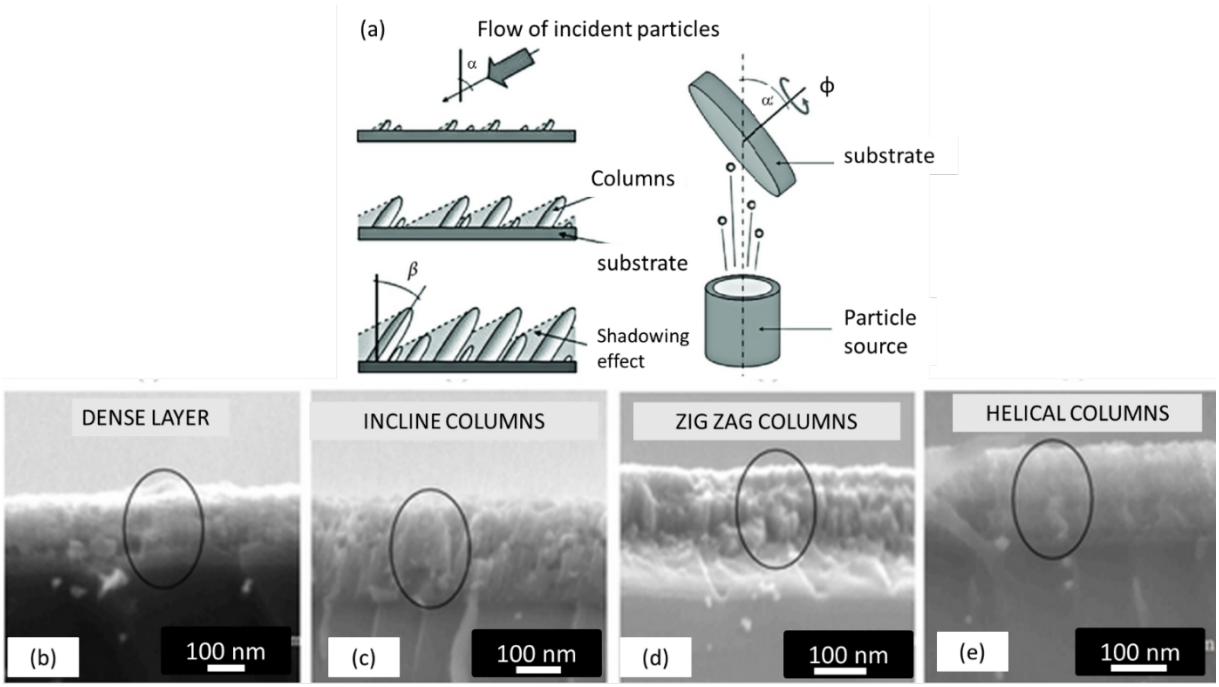

Figure 5.11. a) Principles of glancing angle deposition, b-e) SEM analysis of chosen thin-film edges as dense layer, incline columns, zig zag columns, and helical columns.[204]

5.3.4. Colloidal lithography

Colloidal lithography, colloidal self-assembly, or sometimes called nanosphere lithography, is a very simple, cost and time effective and reproducible fabrication method on different substrates.[207,208,209,210,211] Schematically shown in Figure 5.12, colloidal lithography is a two-step process where first two-dimensional (2D) colloidal crystals are prepared on the substrate and then surface nanostructures are formed using those crystals as a mask in RIE process.[212] Coating of those colloids can be done in various ways such as dip-coating, floating on an interface, electrophoretic deposition, physical and chemical template-guided self-assembly, and spin-coating techniques.[170]

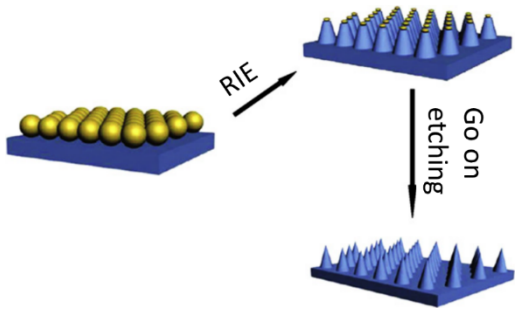

Figure 5.12. Schematic view of the procedure of fabricating anti-reflective structure (ARS) arrays by colloidal lithography.

In RIE process, during substrate etching masked with the nanospheres, spheres themselves are also etched. By increasing the etching duration, the transverse diameter of the sphere is decreased, and the etched area on the substrate is increased gradually. The top diameter of the obtained structure was nearly the same as the transverse diameter of the sphere above, which enables the fabrication of cylinder, or frustum-like shaped surface nanostructures. Polystyrene (PS) nanospheres are the most common materials for colloidal self-assembly as PS has good etching selectivity with the silicon. Recently, Zhang et al. reported high aspect ratio (1:12 aspect ratio) anti-reflecting surface nanostructures of hollow-tip silicon nanowire arrays using metal catalytic wet etching of silicon[213] followed by a short time RIE process to tune the shape of the tips. Resulted silicon hollow-type arrays are shown in Figure 5.13 a & b where reflectance can drop to below 1.3% in visible and near-infrared region and below 5% in mid-infrared region.

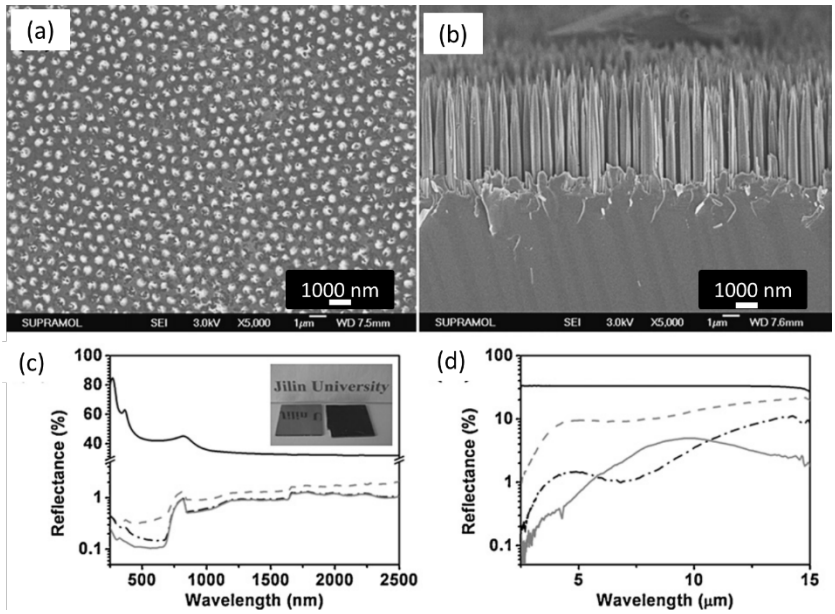

Figure 5.13. (a) Top-view SEM image of the hollow-tip arrays of 7.1 μm in length. (b) Cross-sectional view SEM image of the hollow-tip arrays of 7.1 μm in length. Comparison of the specular reflectance as a function of wavelength for a planar silicon wafer (black solid line) and hollow-tip arrays of 2.1 μm (grey dash line), 3.4 μm (black dash dot line) and 7.1 μm (grey solid line) in length in the UV—VIS—NIR wavelength region (c) and in the mid-infrared region (d). The inset shows photographic images of 20 mm × 20 mm polished silicon wafer (left) and the wafer coated with hollow-tip arrays (right).[213]

5.3.5. Block copolymer self-assembly

Block copolymers (BCP) are commonly used in self-assembly of nanostructures.[214,215] BCP molecules contain two or more polymer chains attached to each other by a covalent bond[216,217,218] where spontaneous self-assembly of those copolymers into different intermolecular phases is possible because of connectivity constraints, entropic factor and incompatibility between the two polymer chains. Through those effects, such copolymers can generate spheres, cylinders, double gyroid, or lamella morphologies that can be used as a mask for etching in order to create surface nanostructures.[219] Block copolymer micelle lithography (BCML) is a lithography technique where metal salts are loaded into the micellar cores of the copolymers during micelle formation

of block copolymers, as shown in Figure 5.14.[220] Micelles consist of insoluble block in the core and the soluble block pointing outward of the block copolymers, which are formed at critical value of polymer concentrations.[221,222] Metal salts such as Au, Ag, Pd, Pt, Co, Ni are reported.[223,224]

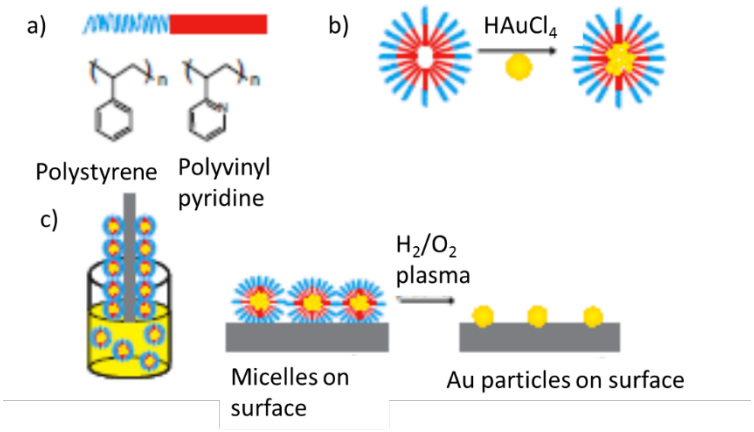

Figure 5.14. Schematic of block copolymer micelle nanolithography (BCML). a) Structural formula of PS-b-P2VP block copolymer. b) Micelle formation from a PS-b-P2VP block copolymer and loading of the gold salt into the micelle core. c) Dip coating and subsequent plasma treatment of the micellar film lead to an array of gold nanoparticles.[220]

By using BCML, highly ordered nano structures can be fabricated over large areas. Compared with conventional photolithography, it is a versatile and inexpensive technique.[220] Various materials such as glass, silica, GaAs, mica as well as sapphire and diamond can be structured with nano-sized islands over a large area (>> 20 cm^2) within minutes. In BCML method, coating of micelle of block copolymers on substrates can be realized using various methods such as spin-coating, dip-coating, etc., and the polymer matrix is then removed completely by hydrogen plasma treatment, where metal such as gold nanoparticles are left behind as surface nanostructures or as a mask for RIE. Figure 5.15 shows the resulted artificial moth-eye structures prepared on glass and fused silica where 2% increase in transmission was achieved.[225]

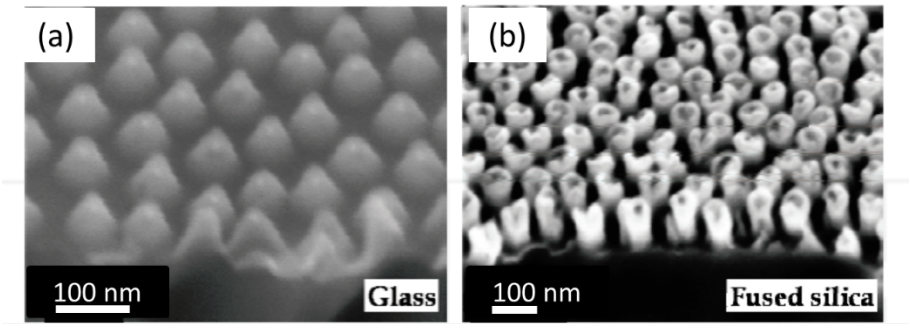

Figure 5.15. "Moth-eye" structured glass cover-slips and fused silica samples. a) High magnification micrograph showing the triangular shape of the glass cones. b) Side-view image of the pillar array measured with a tilt angle of 45^{0}.[225]

5.4. Conclusion

In this chapter, application of surface nanostructures and the fabrication methods are discussed. Micro/nano-sized surface nanostructures grabbed great attention due to their effect on surface property. It plays critical role in wetting/de-wetting, adhesion, and absorption of the incident light to improve the efficiency of the solar cells. These structures were also employed in industry as a smart coating on the surfaces that provide wetting, adhesion, thermal and/or electrical conductivity, super-hydrophobicity, self-cleaning, anti-icing, anti-reflectivity, anti-fogging, capability to direct cell growth, and gas barrier properties. When they are used as an antireflection coating layer, for instance, reflectivity can drop to below 2% over the visible spectrum. Creating such structures, hence, is critical where top-down and bottom-up approaches are utilized. There are many conventional lithography techniques as well as wet etching methods, such as using acids to create micro-nano-islands on the surface, that can be used as a hard etching mask. Among them, colloidal lithography, as an easy fabrication technique, is the most used technique to create surface nanostructures. Block copolymers are also used for the

fabrication with recent studies using metal salts that can incorporate inside the block copolymer micelle during micelle formation.

Chapter 6 High resolution nanofabrication using self-assembly of metal salt-polymer nanocomposite film

The following section is based on previously published work[226] by Con C., Aydinoglu F., and Cui B.
J. Vac. Sci. Technol. B 33(6), Nov/Dec 2015
"**High resolution nanofabrication using self-assembly of metal salt-polymer nanocomposite film**"
Reproduced with permission.

6.1. Introduction and Motivation

Surface nanostructures without long range ordering and precise placement have a wide range of applications. For instance, they can be used as anti-reflective coating (ARC) for photovoltaic devices where the reflection of incident light from the substrate surface is greatly reduced to improve their efficiency. In flat panel display or imaging applications, they can be employed to increase transmission and eliminate ghost image or veil glare.[227] These nanostructures can also mimic and follow the nature's example such as lotus leaves to make super-hydrophobic surfaces, or gecko feet for adhesive surfaces.[155,156,158,227]

These nanostructures can be fabricated via top-down lithography techniques including photolithography, electron-beam lithography, and nanoimprint lithography, and bottom-up lithography approaches that are commonly called self-assembly lithography. Top-down lithography techniques, while offering more precise control of the shape, size and placement of the nanostructures, usually require sophisticated and expensive equipment. Among them, nanoimprint lithography is the most promising one since it is relatively a low-cost and high

throughput process with ultra-high resolution capability, though the mold has to be fabricated by other costly lithography. On the other hand, self-assembly lithography is undoubtedly much cheaper than top down lithography techniques, though it can only achieve either random or periodic patterns without long range ordering unless otherwise guided. The most popular self-assembly lithography is the so-called nano-sphere lithography where nanosized spheres are assembled to form periodic structures. Yet it is challenging to form uniform mono-layer sphere for sub-100 nm sphere size.[228] In recent years, self-assembly of di-block copolymer is gaining increasing popularity, but the process can be lengthy and very sensitive to substrate preparation, and feature size over 100 nm is hard to obtain. Another technique to create surface nanostructures makes use of the self-masking effect in reactive ion etching that lead to the formation of "grass"[192] structure notably "black silicon".[229] Besides silicon, polymer can also be nano-textured by plasma etching.[193,230,231] This roughness instability is due to deposition coming from sputtering of irremovable materials from the metallic or dielectric reactor wall, which acts as hard mask during the polymer etching. Moreover, under certain optimal conditions, ordered periodic morphology can be induced on plasma-etched polymeric surfaces.[231]

The next self-assembly technique is the deposition of metal film on a substrate followed by thermal annealing to achieve sub-micrometer sized metal islands that can be used as hard mask for etching the substrate.[194,195,199] Lastly, CsCl film can be thermally evaporated to form nano-islands as etching mask upon exposure to humidity after film deposition.[232] However, these techniques based on island film both need high cost vacuum deposition tool.

Here, we report a simple process to obtain nanostructures using low-cost spin-coating method and RIE pattern transfer. We dissolved metal salt and polymer in a solvent; and after forming a thin film by spin-coating and thermal annealing to attain a phase separation, the nanocomposite

film was etched with oxygen plasma to remove the polymer matrix, leaving behind nanoscale metal salt islands on the substrate that can be used as a hard-mask to dry-etch the substrate or sub-layer (shown in Figure 6.1). We show that with our method it is possible to achieve sub-20 nm resolution nanostructures on the substrate surface, though it does not give a periodic structure.

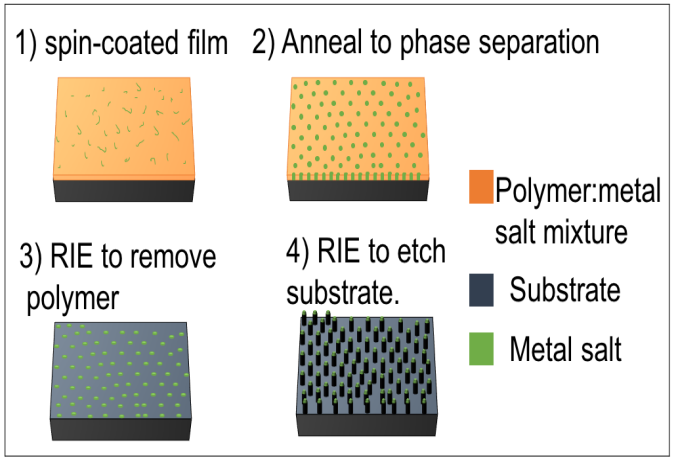

Figure 6.1. Fabrication process of ultra-high resolution nanostructures using self-assembly of metal salt-polymer nanocomposite film. 1) Spin-coating film from a solution containing polymer and salt. 2) Phase separation by thermal annealing. 3) Etching polymer using oxygen plasma and leaving behind metal salt nano-islands on silicon. 4) Etching silicon using fluorine based plasma (CF_4 gases) with metal salt nano-islands as mask.

6.2. Experimental methods

For our purpose we have investigated several metal salts containing nickel metal. Nickel is a very hard etching mask for reactive ion etching using both fluorine and chlorine based plasmas that can create surface nanostructures. Nickel is found in the form of nickel (II) sulfate, nickel (II) nitrate and nickel (II) chloride hexahydrate. Recently, nickel chloride hexahydrate is reported as a metal salt miscible with PMMA resist to increase its etching resistance by 4 times.[233] Unlike salt-containing electron beam resist for lithography, for the purpose of creating nanostructures by

self-assembly, the mixture needs to phase-separate. As nickel (II) nitrate hexahydrate ($Ni(NO_3)_2 \cdot 6H_2O$) has a low melting temperature (56.7 ^oC), phase-separation can be attained readily by thermal annealing.

In the experiment, we first dissolved PMMA powder (996 kg/mol, Sigma Aldrich) with 10 wt/vol % concentration in dimethylformamide (DMF). In parallel, we dissolved nickel nitrate hexahydrate (99.999% purity, Sigma Aldrich) in DMF with varying concentrations of 1-10 wt/vol %. Afterwards, we mixed the as-prepared PMMA solution and salt solution with 1:1 volume ratio and obtained a uniform clear solution. As such, the final solution for spin-coating contains 0.5-5 wt/vol % nickel salt and 5 wt/vol % PMMA, leading to a weight ratio of nickel salt and PMMA ranging from 1:10 to 10:10.

The fabrication process for nanostructured silicon as an example is shown in Figure 6.1. We cleaned the silicon substrate by solvent and oxygen plasma, and coated 100 nm PMMA on silicon. This layer of pure PMMA film was found to help attain a more uniform film of the PMMA-salt mixture. Then the mixture was spin-coated on PMMA film, to obtain a 300 nm-thick film for the case with 10:1 weight ratio of PMMA: metal (obtained by mixing at equal volume 10 wt/vol % PMMA solution and 1 wt/vol % salt solution, both in DMF). Thermal annealing was carried out at 120 ^oC for 1 h to induce phase separation between polymer and the salt. To evaluate the potential intermixing with the bottom PMMA layer, we spin-coated PMMA dissolved in DMF on the bottom PMMA layer, and found the total film thickness was the sum of the top and bottom PMMA films. Hence the bottom PMMA is not significantly dissolved by DMF during the spin-coating and there should be negligible intermixing between the PMMA-salt composite and bottom PMMA layer. We also spin-coated a polystyrene film (glass transition temperature close to that of PMMA, low Flory-Huggins interaction parameter with PMMA and

thus relatively easy inter-diffusion) on the bottom PMMA layer and annealed the film stack at 120 ^{o}C for 5 min. After selectively dissolving the top polystyrene layer using xylene, the remaining PMMA film had a smooth surface, indicating negligible intermixing during the thermal annealing. Therefore, we expect the intermixing between the PMMA-salt composite and bottom PMMA layer is negligible.

Next, we conducted oxygen plasma etching using Trion Phantom II ICP-RIE system (20 sccm O_2, 20 W RF power, 0 W ICP power, 100 mTorr, room temperature, etches PMMA 100 nm/min) to remove PMMA without significant attack of metal salt, leaving behind nickel nitrate nano-islands on silicon as seen in Figure 6.2. As a final step, we etched silicon by RIE using CF_4 gases (20 sccm CF_4, 100 W RF power, 0 W ICP power, 20 mTorr, room temperature; etching rates for silicon, PMMA and metal salt are 30, 300, and roughly 10 nm/min, respectively) with the salt nano-islands as hard etching mask.

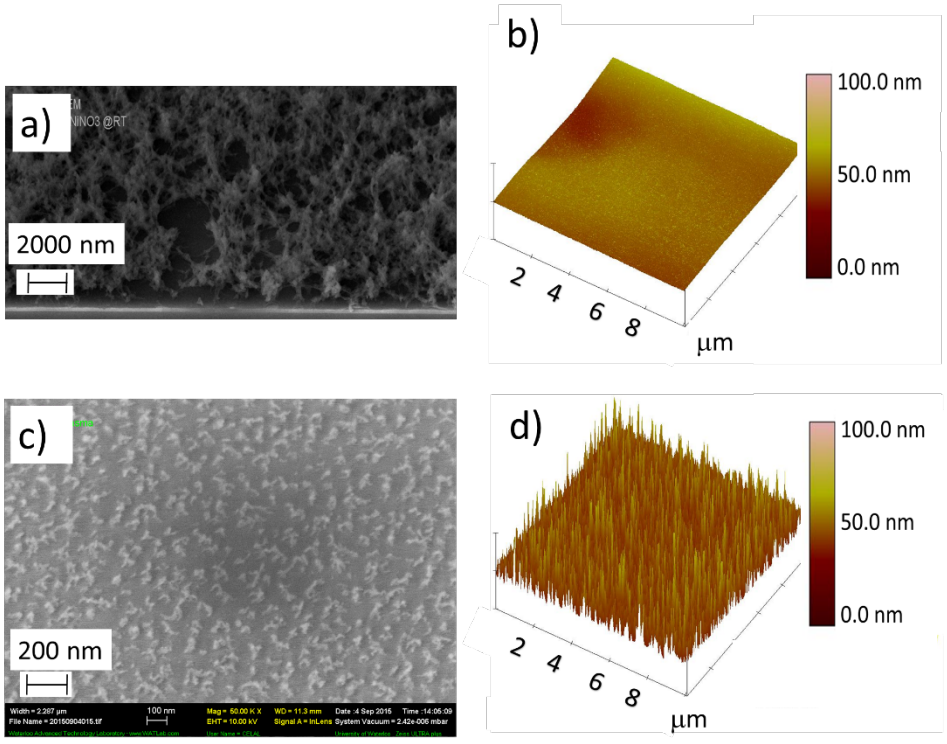

Figure 6.2. a) SEM image of the thin film of PMMA: nickel (II) nitrate hexahydrate 10:1 wt% after spin-coated, without immediate baking, non-uniform film formation is observed. b) AFM image of the same film after annealing at 120 ^{o}C, which introduced uniform film distribution and phase separation. c) SEM image of the film upon oxygen plasma, removed all polymer film and left behind nano-sized metal salt islands. d) AFM image of the film upon oxygen plasma, removed all polymer film and left behind nano-sized metal salt islands.

6.3. Results and discussion

The main challenge is to find a solvent that can dissolve both PMMA and metal salt, because salts are typically soluble in water whereas polymers are commonly soluble in organic solvents. Broadly speaking, solvents are categorized as non-polar solvent such as benzene and toluene, polar aprotic solvent such as tetrahydrofuran (THF), acetone, and DMF, and polar protic solvent such as ethanol, acetic acid and water. After extensive search and trial, we found that this nickel salt is soluble in solvents including THF, DMF and acetic acid, all of which can also dissolve PMMA. Atomic Force Microscopy (Dimension 3100, tapping mode using standard silicon tip)

images are shown in Figure 6.3. Only DMF gave a uniform and smooth film with a rms value of 5.0 nm after spin-coating and thermal annealing, and the other two solvents gave very rough films with a rms value of 26.1 and 27.1 nm for acetic and THF, respectively. Hence we chose DMF solvent, which is a polar aprotic solvent having a boiling temperature of 153 ^{o}C. As for the polymer, we studied only PMMA that is a well-known electron-beam lithography resist and is very popular with low cost.

After PMMA removal by oxygen plasma etching and pattern transfer into silicon using CF4 gas RIE, the obtained self-assembled nanostructures are shown in Figure 6.4, by using Zeiss UltraPlus FESEM. We obtained dense, with the diameters average to be 40.5 nm (Figure 6.4a, and 6.4b) and a standard deviation of 12.46 nm pillars with 100 nm height by using nickel nitrate and PMMA nanocomposite with mass ratio of 1:10 (i.e. the weight concentration for PMMA in the DMF solution is 10 times that of the nickel nitrate hexahydrate), and the pillar diameters are relatively uniform, though the pillar location is rather random without short or long range ordering.

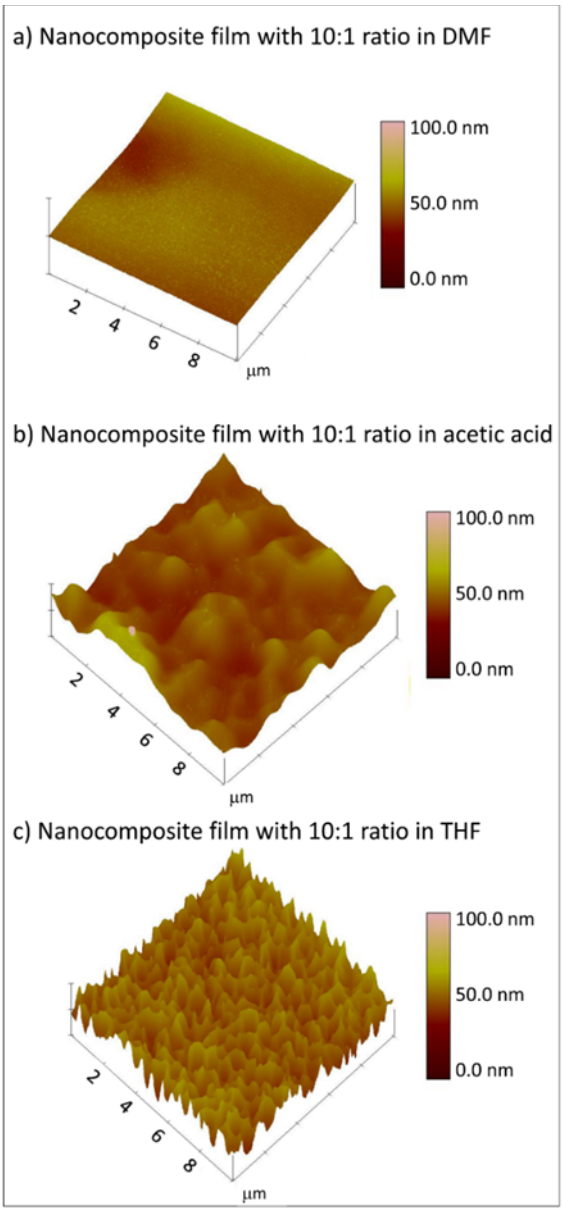

Figure 6.3. AFM images of the thin film of PMMA: nickel (II) nitrate hexahydrate, dissolved for spin-coating in a) DMF, b) acetic acid, and c) THF, respectively. Nanocomposite film inside DMF gives less roughness (5.0 nm) than others (26.1 nm with acetic acid and 27.1 nm with THF).

For this weight ratio, it can be calculated that on average each MMA monomer contains 0.034 Ni atom (alternatively, 1 nickel atom in every 29.0 MMA monomers). As we increased the amount of nickel salt inside PMMA to a ratio of 2:10 - 5:10 (Figure 6.4c-e), pillars become larger that is

expected, and the structure became less well defined. Further increase of the salt in PMMA to a ratio of 7:10 & 10:10 resulted in poorly-defined nanostructure (Figure 6.4f-g), implying that salt islands were agglomerated to form quasi-continuous film.

As the salt consists of a large amount of hydrate (here hexahydrate), it might be decomposed (dehydrated) during the thermal annealing process. Thermal decomposition of metal salts including nickel nitrate has been well studied[234,235,236,237,238,239] under atmospheric or nitrogen environment by monitoring the reactions occurring throughout the decomposition up to 600°C by means of thermogravimetry analysis (TGA) and differential thermal analysis (DTA).[236] These works reported that, with thermal treatment at low pressures (≤5 mbar), only decomposition/dehydration products (tetrahydrate, dihydrate and anhydrous nickel nitrate) are obtained in the first step.[240] Additional study at high temperatures of above 200 ^{o}C and low pressure conditions suggests the presence of intermediate compounds with different characteristics, which eventually give place to NiO with different surface properties.[240] Under atmospheric conditions, Elmasry et al.[239] reported that decomposition/dehydration starts at low temperatures by losing water, and the nickel salt becomes anhydrous ($Ni(NO_3)_2$) at 205 ^{o}C where 37% mass is lost and constant mass is maintained above 205 ^{o}C till 303 ^{o}C, where the salt turns into $Ni_2(OH)_2$ and becomes nickel oxide (NiO) at 505 ^{o}C along with a mass loss of 73.3 % of its original mass.

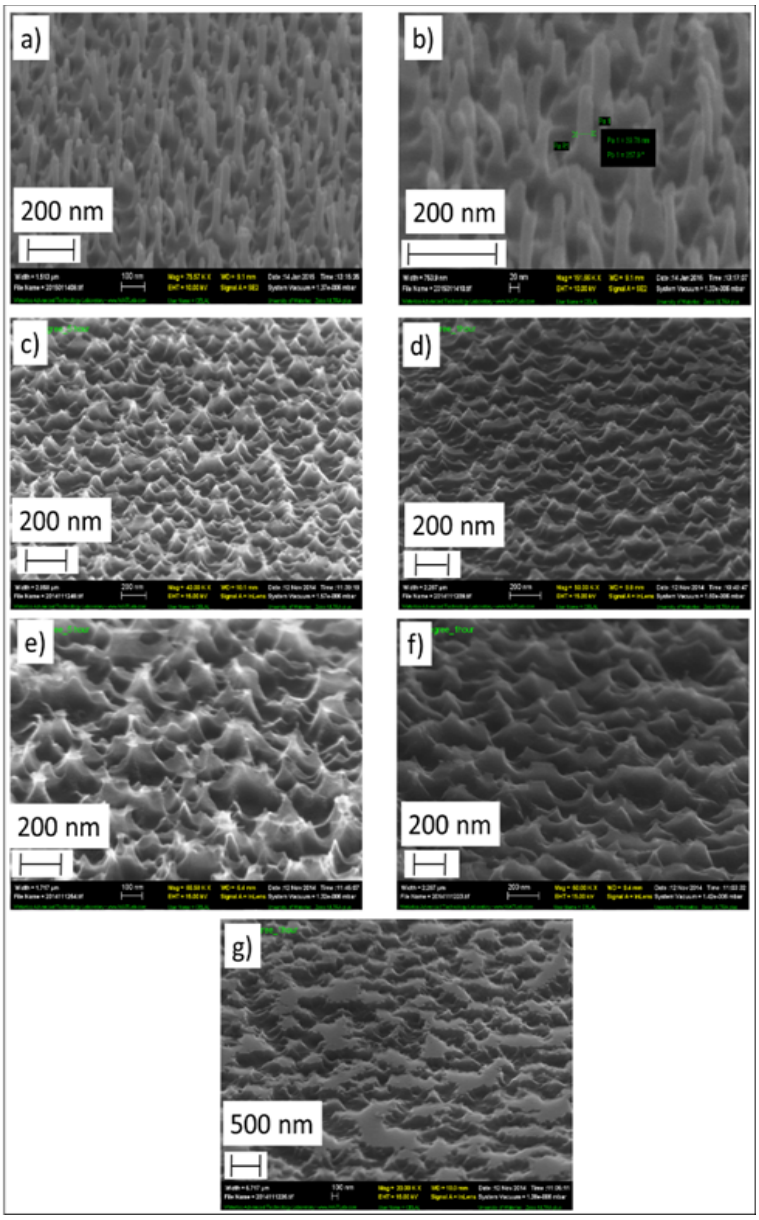

Figure 6.4. SEM images of silicon nanostructures, etched using phase-separated nickel (II) nitrate metal salt:PMMA film as a mask with different weight ratio. a-b) 1:10, c) 2:10, d) 3:10, e) 5:10, f) 7:10, and g) 10:10. It is observed that with 10:1 ratio film, some pillars with diameter less than 20 nm are formed.

According to the TGA analysis by Elmasry et al.,[239] our annealing at 120 ^{o}C at atmospheric condition would lead to a ~12 % mass loss, corresponding to a drop in molecular weight from 290.79 g/mol to 255.89 g/mol by forming $Ni(NO_3)_2 \cdot 4.1H_2O$.

Lastly, similar hard mask for etching the substrate can also be obtained by mixing metal or metal compound nanoparticle with a polymer, followed by etching away the polymer using oxygen plasma. Nanocomposite consisting of metal nanoparticle dispersed in a polymer matrix is considered as a single homogeneous material with unique thermal, mechanical and biological properties when compared to conventional composite.[241,242] Yet it is challenging to disperse evenly the nanoparticle into a polymer matrix, and typically the nanoparticle surface has to be functionalized to avoid agglomeration and attain even distribution in the solvent for spin-coating to form a film. Our method is advantageous in that the final feature size can be tuned by adjusting the salt-polymer weight ratio or annealing conditions, whereas the nanoparticle composite gives only a fixed feature size equal to the particle diameter.

6.4. Conclusion

In this section, development of a simple process to obtain nanostructures using the low-cost spin-coating method and RIE pattern transfer was discussed. Metal salt and polymer are dissolved in a solvent; and after spin-coating to form a thin film and thermal annealing to attain a phase separation, the nanocomposite was etched with oxygen plasma to remove the polymer matrix, leaving behind nanoscale salt islands on the substrate that can be used as a hard-mask to dry-etch the substrate or sub-layer. The key challenge for this process is to identify a solvent or solvent mixture that can dissolve both the salt (commonly soluble in water) and polymer (commonly soluble only in organic solvent). After extensive testing, we found that nickel (II) nitrate hexahydrate and PMMA can be dissolved in DMF and form a uniform film by spin-coating. Nickel nitrate is a suitable salt since nickel is a very hard mask for RIE using both F- and Cl-plasmas, and it has a low melting temperature of 56.7 ^{o}C. It is calculated that 10:1 weight ratio of PMMA and salt corresponds to 1 nickel atom in every 29.0 MMA monomers. Using this method

with optimum weight ratio of 1:10, very high resolution (down to 20 nm) silicon nano-pillars with 100 nm height and ~100 nm spacing at low cost and wafer-scale high throughput can be achieved.

6.5. Application for anti-reflective and super-hydrophobic coatings

The following section is not previously published.

As shown in the sections above, our method is capable of high resolution fabrication of surface nanostructures. Nickel salts have been initially tested, but as it is a magnetic material and less microfabrication compatible, here I extended the choice of metal salt to aluminum (III) nitrate nonahydrate [$Al(NO_3)_3.9H_2O$] (ANN), and chromium (III) nitrate nonahydrate [$Cr(NO_3)_3.9H_2O$] (CNN), since Al and Cr are more microfabrication compatible - they are both commonly used as hard plasma etching mask for pattern transfer in micro/nano-fabrication. For instance, selectivity between Cr and Si using silicon etching recipe developed by Khorasaninejad et al.[133] is ~1:80. In addition, ANN and CNN have a low melting point around 66 ^{o}C and 60 ^{o}C respectively, which increases their chance of phase separation at relatively low temperature. Lastly, it is found that, similar to nickel metal salts, those metal salts are also soluble in DMF solvent. Hence, I prepared ANN:PMMA and CNN:PMMA metal salt: polymer nanomaterials with different concentrations, and the solution in DMF was homogeneous to give a smooth thin film after spin-coating on a substrate.

6.5.1. Effect of annealing temperature on formation of nanoislands

To study the effect of annealing temperature on phase separation of metal salts, I prepared ANN : PMMA with 1:10 ratio. Keeping same spin-coating conditions, I annealed the films at temperatures ranging from 40 ^{o}C to 200 ^{o}C. After annealing, samples are exposed to oxygen plasma to remove the polymer part of the film, and then the underneath silicon is etched using

switching (Bosch) or non-switching etching recipe with SF_6 and C_4F_8 gas.[133] Typical resulted structures are shown in Figure 6.5. Nanopillars are formed in all conditions, even without annealing (Figure 6.5a), Relatively uniform distribution of pillar diameter and inter-pillar spacing was obtained when the film was annealed at 100 ^oC.

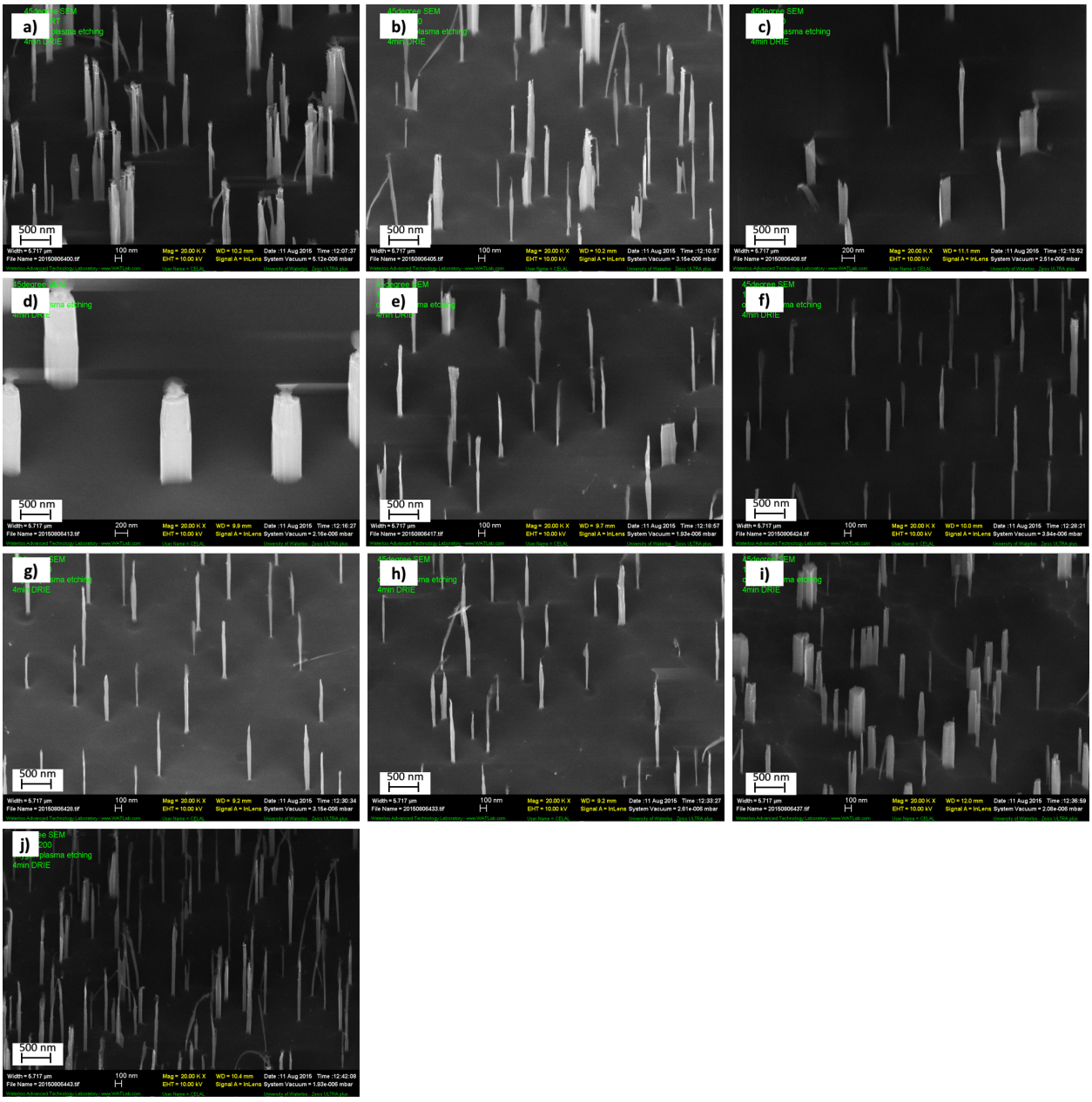

Figure 6.5. SEM images of silicon nanostructures, etched using phase-separated aluminum (III) nitrate nonahydrate (ANN) metal salt : PMMA film as a mask with 1:10 weight ratio annealed at different temperatures. a) no baking, b) 40 ^{o}C, c) 50 ^{o}C, d) 60 ^{o}C, e) 80 ^{o}C, f) 100 ^{o}C, g) 120 ^{o}C, h) 150 ^{o}C, i) 180 ^{o}C, and j) 200 ^{o}C. It is observed that with 10:1 ratio film, pillars with diameter sub-50 nm are formed uniformly with 100 ^{o}C (Figure f) and 120 ^{o}C (Figure g) baking temperatures.

6.5.2. High aspect ratio nanopillars formation

After a systematic study, I chose to use ANN with 1:10 metal salt : polymer weight ratio and 120^{o}C annealing temperature since this condition gives more uniform pillar diameter. After annealing the film for 1 hour, 10 min oxygen plasma etching is performed, followed by 4 min RIE. As shown in Figure 6.6, pillars with sub-40 nm diameter and ~1:30 aspect ratio are fabricated with average inter-pillar distance of roughly ~300 nm.

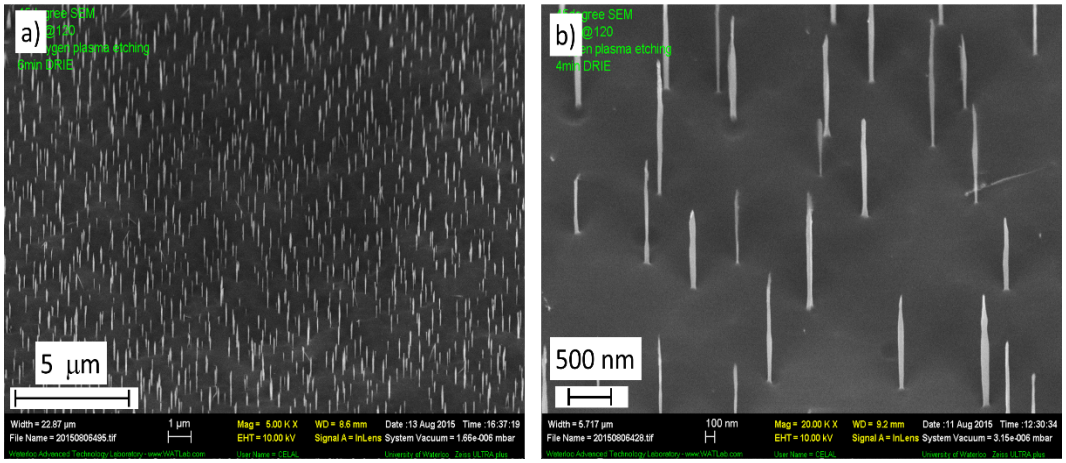

Figure 6.6. SEM images of silicon nanopillars formed upon DRIE using aluminum nitrate nonahydrate: polymer 1:10 ratio. a) Nanostructures over large area b) 40 nm diameter pillars with 1:29 aspect ratio annealed at 120 ^{o}C.

6.5.3. Effect of metal salt: polymer ratio on formation of nanostructures

In order to apply those structures for anti-reflection or super-hydrophobic coatings, denser pillars are desired. ANN : PMMA and CNN : PMMA mixture with different ratios in DMF solvent were prepared. Upon film spin coating on the substrate, films are baked at 120 ^{o}C for 1 hour. As discussed in chapter 5, surface nanostructures are popular for anti-reflective and/or hydrophobic coating applications, and ideally the pillars should have a cone-shape tapered profile. Hence, I modified the etching process to fabricate such cone-shaped pillars. Previously, Faycal et al. reported RIE recipes to give tapered profile.[243] Using the same etching recipe, resulted structures

are shown in Figure 6.7 for ANN : PMMA, and Figure 6.8 for CNN : PMMA with different ratios. For ANN salt, as shown in Figure 6.7a and 6.7b, pillars with diameter close to 400 nm are formed, and the pillars are denser with 100 nm diameter and more tapered when metal salt : polymer ratio was increased to 3:10 and 5:10 (see in 6.7c and 6.7d). As for CNN salt, (Figure 6.8), the pillars have similar dimensions to those produced by ANN salt. This was expected as these metal salts have similar chemical structure and melting temperature.

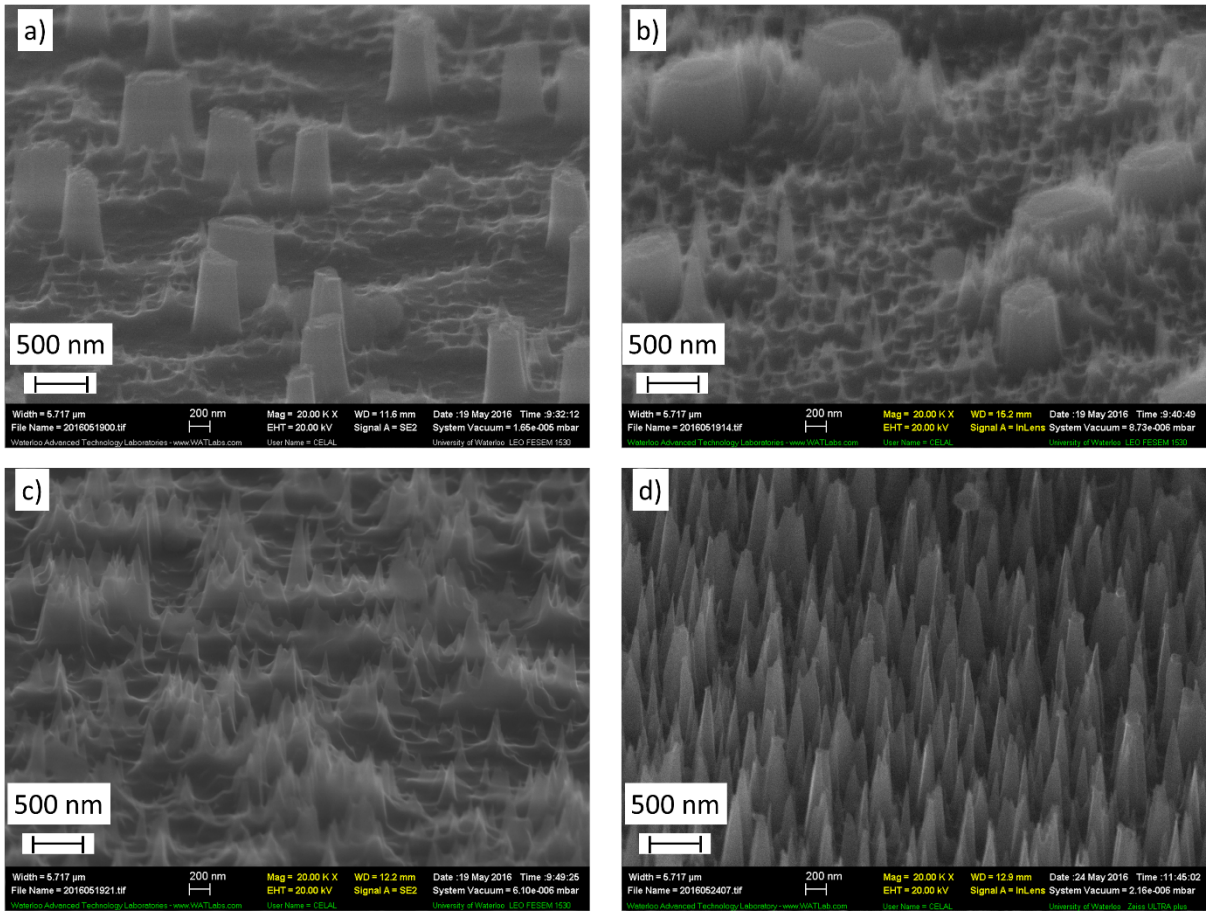

Figure 6.7. SEM images of silicon nanopillars formed upon DRIE using aluminum nitrate nonahydrate: polymer a) 1:10, b) 2:10, c) 3:10, and d) 5:10 ratio.

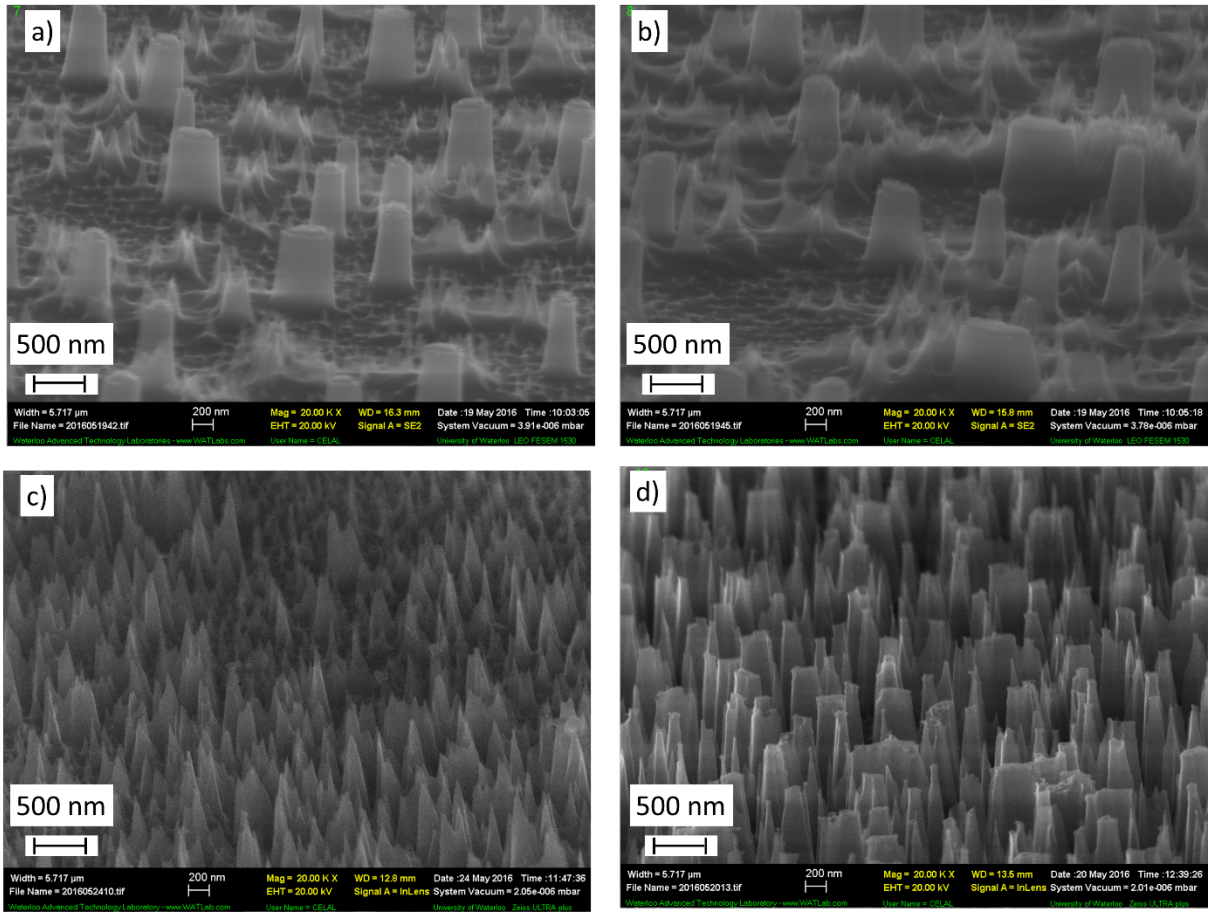

Figure 6.8. SEM images of silicon nanopillars formed upon DRIE using chromium nitrate nonahydrate: polymer a) 1:10, b) 2:10, c) 3:10, and d) 5:10 ratio.

6.5.4. Anti-reflectivity properties of fabricated surface nanostructures

Figure 6.9 compared silicon wafer before and after surface nanostructuring using metal salt : polymer phase separation self assembly and RIE pattern transfer, which shows clearly the greatly reduced reflectivity for the structured surfaces. In order to quantify the anti-reflective property, reflectivity measurements were carried out using PerkinElmer Precisely Inc. Lambda 35 UV/VIS spectrometer with spectrum scan speed of 240 nm/min. Resulted spectra are shown in Figure 6.10. As expected from SEM images shown in Figure 6.7 and 6.8, reflectivity is decreased by

increasing salt ratio in the nanocomposite film. Compared to bare silicon which shows ~35% reflectivity in visible region, the reflectivity drops to 15 % for structures fabricated using metal salt : polymer ratio of 1:10, 12 % for 2:10, 7 % for 3:10, and only 2 % for 5:10 ratio, which represents one order improvement over the unpatterned bare silicon wafer.

Figure 6.9. Comparison of silicon wafer before and after processing with metal salt : polymer composite film and DRIE. It can be seen by eye how they show less reflectivity with respect to bare silicon wafer.

The improvement is also rather high compared to many published results that occasionally reported reflectivity down to 2% in visible region. Further improvement of our result might be realized by increasing the metal salt content in the nanocomposite film; yet actually the surface structures turned out to be very large at too high metal salt content, which led to higher reflectivity. This is not unexpected because more metal salt would eventually result in merged nanoislands to form much larger ones. Another way to enhance the anti-reflectivity property could be by using different plasma etching conditions to provide more tapered profile or higher aspect ratio structures.

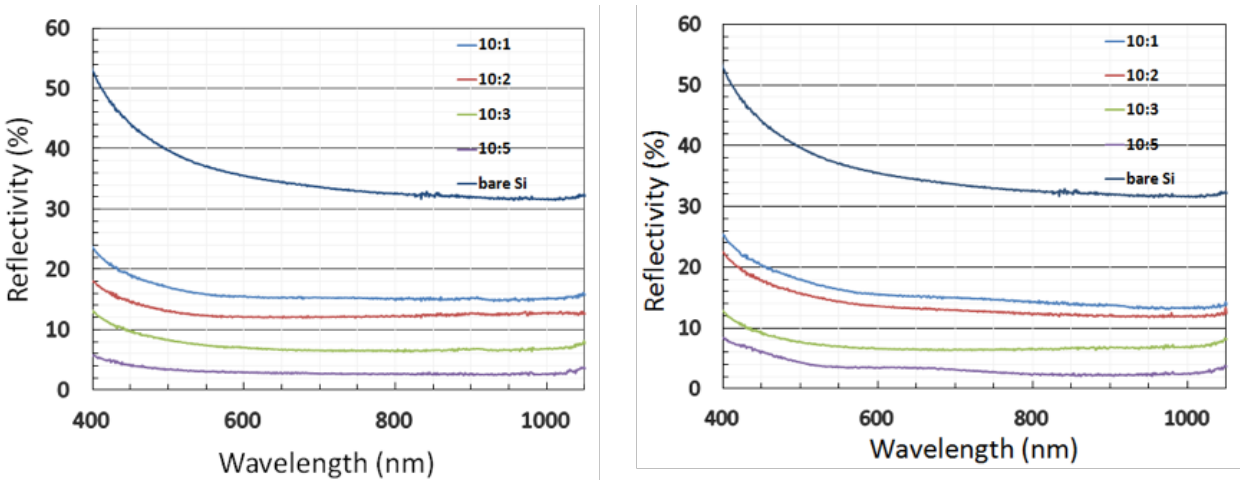

Figure 6.10. Comparison of reflectivity measurements of silicon wafer with nanopillars fabricated by using a) ANN:polymer, b) CNN:polymer metal salt with different weight ratios.

6.5.5. Super-hydrophobic applications of fabricated surface structures

Another popular application of these surface structures is for hydrophobic coatings. In order to test this property, water contact angle measurements were conducted, using Ramé-hart Model 200 Standard Contact Angle Goniometer with DROP image CA v2.5, on samples coated with a self-assembled monolayer of Trichloro (1H,1H,2H,2H-perfluorooctyl)silane (FOTS). Results of water droplets on bare silicon wafer and on surface structured wafers using metal salt (ANN or CNN) : polymer nanocomposite of different weight ratios are shown in Figure 6.11. Silicon wafer gives a contact angle of 110^{o} when coated with FOTS, whereas our structures can greatly increase the contact angle up to a remarkable value of 165.7^{o} when using 3:10 ratio of metal salt : polymer. Our results are close to the reported highest contact angles, such as the 165^{o} water contact angle achieved by Checco et al.,[159] yet our process is simpler with lower cost.

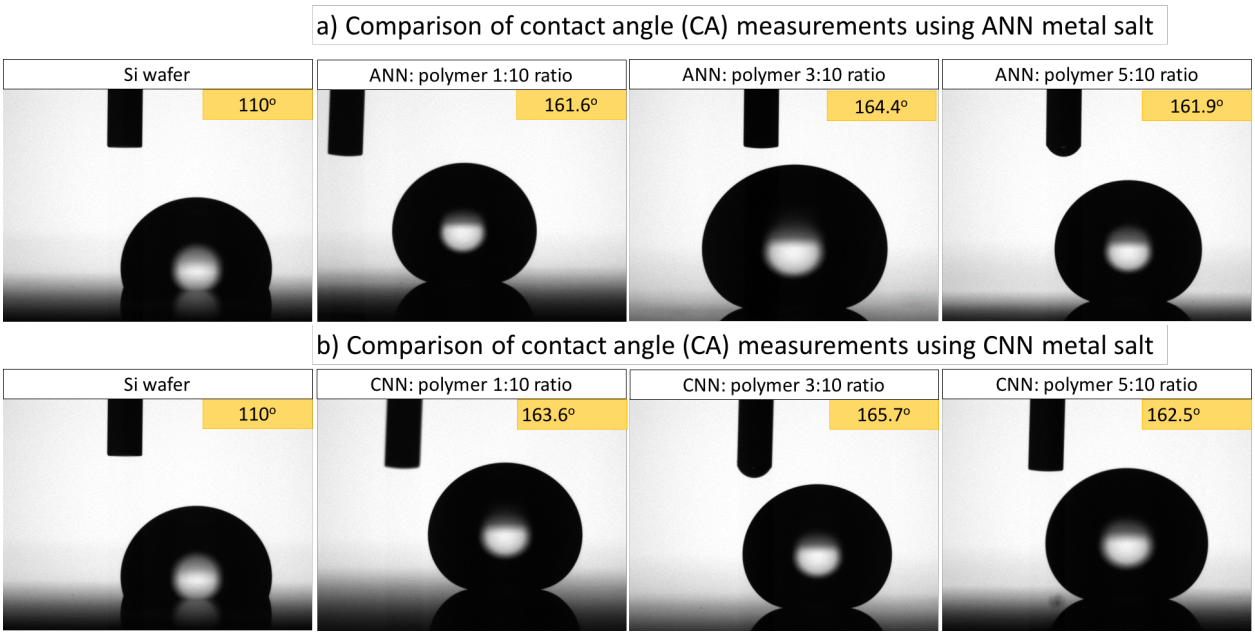

Figure 6.11. Comparison of water contact angle measurements of silicon wafer with nanopillars fabricated by using a) ANN : polymer, b) CNN : polymer metal salt with different weight ratios after treatment with FOTS surfactant.

6.5.6 Conclusion

By using phase separation of metal salt – polymer nanocomposite film, we showed the fabrication of surface structures etched into silicon with high aspect ratio (1:30) and high resolution (sub-50 nm). Aluminum nitrate nonahydrate and chromium nitrate nonahydrate can both be used in order to obtain those structures. By using appropriate metal salt : polymer ratio, here 5:10 as optimum, reflectivity of light in visible region can be reduced down to only 2 % that is quite remarkable for many applications. Beside anti-reflective properties, these fabricated structures can also provide super-hydrophobic property with exceptionally high water contact angle of up to 165.7^{o}. These values could be further improved by modifying metal content inside the composite film or optimizing the silicon dry etching conditions.

References

1 Feynman, R. P. (1960). There's plenty of room at the bottom. Engineering and science, 23(5), 22-36.

2 Zhang, J. (2014). Nanofabrication and its application in plasmonic chemical and bio-sensors. (Doctoral Dissertation, University of Waterloo).

3 Chen, Y. (2015). Nanofabrication by electron beam lithography and its applications: A review. Microelectronic Engineering, 135, 57-72.

4 Zoski, C. G. (Ed.). (2006). Handbook of electrochemistry. Elsevier. p.678.

5 Menon, V. P., & Martin, C. R. (1995). Fabrication and evaluation of nanoelectrode ensembles. Analytical Chemistry, 67(13), 1920-1928.

6 Moretto, L. M., Tormen, M., De Leo, M., Carpentiero, A., & Ugo, P. (2011). Polycarbonate-based ordered arrays of electrochemical nanoelectrodes obtained by e-beam lithography. Nanotechnology, 22(18), 185305.

7 Madou, M. J. (2002). Fundamentals of microfabrication: the science of miniaturization. CRC press.

8 Yang, J. K., Jung, Y. S., Chang, J. B., Mickiewicz, R. A., Alexander-Katz, A., Ross, C. A., & Berggren, K. K. (2010). Complex self-assembled patterns using sparse commensurate templates with locally varying motifs. Nature nanotechnology, 5(4), 256-260.

9 Ji, S., Liu, C. C., Liu, G., & Nealey, P. F. (2009). Molecular transfer printing using block copolymers. ACS nano, 4(2), 599-609.

10 Rai-Choudhury, P. (1997). Handbook of microlithography, micromachining, and microfabrication: microlithography (Vol. 1).

11 Mohammad, M. A., Chen, J., Stepanova, M., Aktary, M., Buswell, S., Dew, S. K., & Fito, T. (2010). The Interdependence of Exposure and Development Conditions when Optimizing Low-Energy EBL for Nano-Scale Resolution. INTECH Open Access Publisher. p.293.

12 Mohammad, M. A., Muhammad, M., Dew, S. K., & Stepanova, M. (2012). Fundamentals of electron beam exposure and development. InNanofabrication (pp. 11-41). Springer Vienna. p.350.

13 Santos, A., Deen, M. J., & Marsal, L. F. (2015). Low-cost fabrication technologies for nanostructures: state-of-the-art and potential. Nanotechnology, 26(4), 042001.

14 Rius Suñé, G., Pérez Murano, F., & Bausells Roige, J. (2008). Electron beam lithography for nanofabrication. (Doctorate Dissertation, Universitat Autònoma de Barcelona).

15 Ito, T., & Okazaki, S. (2000). Pushing the limits of lithography. Nature,406(6799), 1027-1031.

16 Cui, B. (2010). Nanofabrication: principles, capabilities and limits.

Retrieved from https://ece.uwaterloo.ca/~bcui/ECE_730.html. [Powerpoint slides].

17 Venugopal, G., and Kim, S-J. (2013). Nanolithography. In K. Takahata (Ed.), InTech. Advances in Micro/Nano Electromechanical Systems and Fabrication Technologies. DOI: 10.5772/55527.

18 Kumar, S., Karmakar, S., Bramanti, A., Rinaldi, R., and Maruccio, G. (2011). Nanofabrication for Molecular Scale Devices. In Y. Masuda (Ed.), InTech. Nanofabrication. DOI: 10.5772/28491.

19 Marmiroli, B., & Amenitsch, H. (2012). X-ray lithography and small-angle X-ray scattering: a combination of techniques merging biology and materials science. European Biophysics Journal, 41(10), 851-861.

20 Mojarad, N., Gobrecht, J., & Ekinci, Y. (2015). Interference lithography at EUV and soft X-ray wavelengths: Principles, methods, and applications. Microelectronic Engineering, 143, 55-63.

21 Lu, C., & Lipson, R. H. (2010). Interference lithography: a powerful tool for fabricating periodic structures. Laser & Photonics Reviews, 4(4), 568-580.

22 Lan, H., and Ding, Y. (2010). Nanoimprint Lithography. In M. Wang(Ed.), Lithography, InTech. Retrieved from: http://www.intechopen.com/books/lithography/nanoimprint-lithography.

23 Chou, S. Y., Krauss, P. R., Zhang, W., Guo, L., & Zhuang, L. (1997). Sub-10 nm imprint lithography and applications. Journal of Vacuum Science & Technology B, 15(6), 2897-2904.

24 Con, C. (2011). Design and Characterization of Resist and Mold Materials for Electron-Beam and Nanoimprint Lithography. (MASc Dissertation, University of Waterloo).

25 Wang, M. (2010). Lithography. Intech.

26 Zhang, W., & Chou, S. Y. (2003). Fabrication of 60-nm transistors on 4-in. wafer using nanoimprint at all lithography levels. Applied physics letters,83(8), 1632-1634.

27 Balla, T., Spearing, S. M., & Monk, A. (2008). An assessment of the process capabilities of nanoimprint lithography. Journal of Physics D: Applied Physics,41(17), 174001.

28 Martini, I., Eisert, D., Kamp, M., Worschech, L., Forchel, A., & Koeth, J. (2000). Quantum point contacts fabricated by nanoimprint lithography.Applied Physics Letters, 77(14), 2237-2239.

29 Yu, Z., Schablitsky, S. J., & Chou, S. Y. (1999). Nanoscale GaAs metal-semiconductormetal photodetectors fabricated by nanoimprinting lithography.Appl. Phys. Lett, 64, 2381.

30 Lai, K. L., Leu, I. C., & Hon, M. H. (2009). Soft imprint lithography using swelling/deswelling characteristics of a polymer mold and a resist induced by a poor solvent. Journal of Micromechanics and Microengineering, 19(3), 037001.

31 Chou, S. Y., Krauss, P. R., & Renstrom, P. J. (1995). Imprint of sub-25 nm vias and trenches in polymers. Applied physics letters, 67(21), 3114-3116.

32 Guo, L. J. (2007). Nanoimprint lithography: methods and material requirements. Advanced Materials, 19(4), 495-513.

33 Canelas, D. A., Herlihy, K. P., & DeSimone, J. M. (2009). Top-down particle fabrication: control of size and shape for diagnostic imaging and drug delivery. Wiley Interdisciplinary Reviews: Nanomedicine and Nanobiotechnology, 1(4), 391-404.

34 Khang, D. Y., & Lee, H. H. (2004). Sub-100 nm patterning with an amorphous fluoropolymer mold. Langmuir, 20(6), 2445-2448.

35 Con, C., Zhang, J., Jahed, Z., Tsui, T. Y., Yavuz, M., & Cui, B. (2012). Thermal nanoimprint lithography using fluoropolymer mold. Microelectronic Engineering, 98, 246-249.

36 Gates, B. D., Xu, Q., Stewart, M., Ryan, D., Willson, C. G., & Whitesides, G. M. (2005). New approaches to nanofabrication: molding, printing, and other techniques. Chemical reviews, 105(4), 1171-1196.

37 Kim, C. S., Ahn, S. H., & Jang, D. Y. (2012). Review: Developments in micro/nanoscale fabrication by focused ion beams. Vacuum, 86(8), 1014-1035.

38 Wanzenboeck, H. D., and Waid, S. (2011). Focused Ion Beam Lithography. In Cui B. (Ed.), Recent Advances in Nanofabrication Techniques and Applications. DOI: 10.5772/22075.

39 Ward, B. W., Notte, J. A., & Economou, N. P. (2006). Helium ion microscope: A new tool for nanoscale microscopy and metrology. Journal of Vacuum Science & Technology B, 24(6), 2871-2874.

40 Hlawacek, G., Veligura, V., van Gastel, R., & Poelsema, B. (2014). Helium ion microscopy. Journal of Vacuum Science & Technology B, 32(2), 020801.

41 Iberi, V., Vlassiouk, I., Zhang, X. G., Matola, B., Linn, A., Joy, D. C., & Rondinone, A. J. (2015). Maskless lithography and in situ visualization of conductivity of graphene using helium ion microscopy. Scientific reports, 5.

42 Duan, X. R., Dong, J. Q., Yan, L. W., Ding, X. T., Yang, Q. W., Rao, J., ... & Lei, G. J. (2010). Preliminary results of ELMy H-mode experiments on the HL-2A tokamak. Nuclear Fusion, 50(9), 095011.

43 Grigorescu, A. E., & Hagen, C. W. (2009). Resists for sub-20-nm electron beam lithography with a focus on HSQ: state of the art. Nanotechnology, 20(29), 292001.

44 Mayadas, A. F., & Laibowitz, R. B. (1972). One-dimensional superconductors. Physical Review Letters, 28(3), 156.

45 Pala, N., & Karabiyik, M. (2012). Electron Beam Lithography (EBL). In Encyclopedia of Nanotechnology (pp. 718-740). Springer Netherlands.

46 Herriott, D. R., & Brewer, G. R. (1980). Electron-beam lithography machines. Electron-Beam Technology in Microelectronic Fabrication, 141-216.

47 Kraus, T. (2007). Assembly and printing of micro and nano objects. Cuvillier Verlag.

48 Dey, R. K., & Cui, B. (2014). Lift-off with solvent for negative resist using low energy electron beam exposure. Journal of Vacuum Science & Technology B,32(6), 06F507.

49 Tseng, A. A. (2008). Nanofabrication: fundamentals and applications. World Scientific.

50 Wu, C. S., Makiuchi, Y., and Chen, C-D. (2010). High-energy Electron Beam Lithography for Nanoscale Fabrication, Lithography, Michael Wang (Ed.), InTech, DOI: 10.5772/8179. Available from: http://www.intechopen.com/books/lithography/high-energy-electron-beam-lithography-for-nanoscale-fabrication.

51 Namatsu, H., Takahashi, Y., Yamazaki, K., Yamaguchi, T., Nagase, M., & Kurihara, K. (1998). Three-dimensional siloxane resist for the formation of nanopatterns with minimum linewidth fluctuations. Journal of Vacuum Science & Technology B, 16(1), 69-76.

52 Yamaguchi, T., Namatsu, H., Nagase, M., Yamazaki, K., & Kurihara, K. (1999). A new approach to reducing line-edge roughness by using a cross-linked positive-tone resist. Japanese Journal of Applied Physics, 38(12S), 7114.

53 Manfrinato, V. R., Zhang, L., Su, D., Duan, H., Hobbs, R. G., Stach, E. A., & Berggren, K. K. (2013). Resolution limits of electron-beam lithography toward the atomic scale. Nano letters, 13(4), 1555-1558.

54 Alexander P, Black R M, and Charlesby A. (1955). Radiobiology symposium liege. Proc. Royal Soc. (London) A320, 136.

55 Alexander P, Charlesby A, and Ross M. (1954). Proc. Royal Soc. (London) A223, 392.

56 Cord, B. M. (2009). Achieving sub-10-nm resolution using scanning electron beam lithography (Doctoral dissertation, Massachusetts Institute of Technology).

57 Cui, Z. (2009). Nanofabrication: principles, capabilities and limits. Springer Science & Business Media.

58 Hu, W. W., Sarveswaran, K., Lieberman, M., & Bernstein, G. H. (2004). Sub-10 nm electron beam lithography using cold development of poly (methylmethacrylate). Journal of Vacuum Science & Technology B, 22(4), 1711-1716.

59 Vieu, C., Carcenac, F., Pepin, A., Chen, Y., Mejias, M., Lebib, A., ... & Launois, H. (2000). Electron beam lithography: resolution limits and applications. Applied Surface Science, 164(1), 111-117.

60 Mohsin, M. A., & Cowie, J. M. (1988). Enhanced sensitivity in the electron beam resist poly (methyl methacrylate) using improved solvent developer. Polymer, 29(12), 2130-2135.

61 Yasin, S., Hasko, D. G., & Ahmed, H. (2002). Comparison of MIBK/IPA and water/IPA as PMMA developers for electron beam nanolithography. Microelectronic engineering, 61, 745-753.

62 Ikeura-Sekiguchi, H., Sekiguchi, T., & Koike, M. (2005). Characterization and degradation of ZEP520 resist film by TOF-PSID and NEXAFS. Journal of electron spectroscopy and related phenomena, 144, 453-455.

63 Yamaguchi, T., & Hamatsu, H. (2004). Impact of developers on roughness of dissolution front in electron-beam resists. Journal of Photopolymer Science and Technology, 17(4), 557-565.

64 Medeiros, D. R., Aviram, A., Guarnieri, C. R., Huang, W. S., Kwong, R., Magg, C. K., ... & Angelopoulos, M. (2001). Recent progress in electron-beam resists for advanced mask-making. IBM Journal of Research and Development, 45(5), 639-650.

65 ZEON Corporation Electronic Materials Division. (2 Oct. 2010). ZEP520A Technical Report.

66 Namatsu, H., Nagase, M., Kurihara, K., Iwadate, K., & Murase, K. (1995). 10-nm silicon lines fabricated in (110) silicon. Microelectronic engineering, 27(1), 71-74.

67 Yamaguchi, T., & Namatsu, H. (2004). Effect of developer molecular size on roughness of dissolution front in electron-beam resist. Journal of Vacuum Science & Technology B, 22(3), 1037-1043.

68 Mohammad, M. A., Koshelev, K., Fito, T., Zheng, D. A. Z., Stepanova, M., & Dew, S. (2012). Study of development processes for ZEP-520 as a high-resolution positive and negative tone electron beam lithography resist. Japanese Journal of Applied Physics, 51(6S), 06FC05.

69 Schirmer, M., Büttner, B., Syrowatka, F., Schmidt, G., Köpnick, T., & Kaiser, C. (2013, October). Chemical Semi-Amplified positive E-beam Resist (CSAR 62) for highest resolution. In 29th European Mask and Lithography Conference (pp. 88860D-88860D). International Society for Optics and Photonics.

70 Lercel, M. J., Tiberio, R. C., Chapman, P. F., Craighead, H. G., Sheen, C. W., Parikh, A. N., & Allara, D. L. (1993). Self-assembled monolayer electron-beam resists on GaAs and SiO2. Journal of Vacuum Science & Technology B, 11(6), 2823-2828.

71 Manako, S., Ochiai, Y., Yamamoto, H., Teshima, T., Fujita, J. I., & Nomura, E. (2000). High-purity, ultrahigh-resolution calixarene electron-beam negative resist. Journal of Vacuum Science & Technology B, 18(6), 3424-3427.

72 Fujita, J., Ohnishi, Y., Ochiai, Y., Nomura, E., & Matsui, S. (1996). Nanometer-scale resolution of calixarene negative resist in electron beam lithography. Journal of Vacuum Science & Technology B, 14(6), 4272-4276.

73 Tada, T., & Kanayama, T. (1996). Nanolithography using fullerene films as an electron beam resist. Japanese journal of applied physics, 35(1A), L63.

74 Tada, T., Kanayama, T., Robinson, A. P. G., Palmer, R. E., Allen, M. T., Preece, J. A., & Harris, K. D. M. (2000). A triphenylene derivative as a novel negative/positive tone resist of 10 nanometer resolution. Microelectronic engineering, 53(1), 425-428.

75 Williamson, F., & Shields, E. A. (2003, December). SU-8 as an electron beam lithography resist. In University/Government/Industry Microelectronics Symposium. Proceedings of the 15th Biennial (pp. 57-60). IEEE.

76 Aktary, M., Jensen, M. O., Westra, K. L., Brett, M. J., & Freeman, M. R. (2003). High-resolution pattern generation using the epoxy novolak SU-8 2000 resist by electron beam lithography. Journal of Vacuum Science & Technology B, 21(4), L5-L7.

77 Bilenberg, B., Jacobsen, S., Schmidt, M. S., Skjolding, L. H. D., Shi, P., Bøggild, P., ... & Kristensen, A. (2006). High resolution 100kV electron beam lithography in SU-8. Microelectronic Engineering, 83(4), 1609-1612.

78 Yang, J. K., Cord, B., Duan, H., Berggren, K. K., Klingfus, J., Nam, S. W., ... & Rooks, M. J. (2009). Understanding of hydrogen silsesquioxane electron resist for sub-5-nm-half-pitch lithography.

79 Muray, A., Isaacson, M., & Adesida, I. (1984). AlF3—A new very high resolution electron beam resist. Applied Physics Letters, 45(5), 589-591.

80 Kratschmer, E., & Isaacson, M. (1987). Progress in self-developing metal fluoride resists. Journal of Vacuum Science & Technology B, 5(1), 369-373.

81 Macaulay, J. M., Allen, R. M., Brown, L. M., & Berger, S. D. (1989). Nanofabrication using inorganic resists. Microelectronic Engineering, 9(1), 557-560.

82 Clendenning, S. B., Aouba, S., Rayat, M. S., Grozea, D., Sorge, J. B., Brodersen, P. M., ... & Ruda, H. E. (2004). Direct Writing of Patterned Ceramics Using Electron-Beam Lithography and Metallopolymer Resists.Advanced Materials, 16(3), 215-219.

83 Gonsalves, K. E., Merhari, L., Wu, H., & Hu, Y. (2001). Organic–inorganic nanocomposites: unique resists for nanolithography. Advanced Materials,13(10), 703-714.

84 Zhang, J., Cao, K., Wang, X. S., & Cui, B. (2015). Metal-carbonyl organometallic polymers, PFpP, as resists for high-resolution positive and negative electron beam lithography. Chemical Communications, 51(99), 17592-17595.

85 Zhang, J., Con, C., & Cui, B. (2014). Electron beam lithography on irregular surfaces using an evaporated resist. ACS nano, 8(4), 3483-3489.

86 Xia, Y., & Whitesides, G. M. (1998). Soft lithography. Annual review of materials science, 28(1), 153-184.

87 Ko, H. C., Stoykovich, M. P., Song, J., Malyarchuk, V., Choi, W. M., Yu, C. J., ... & Rogers, J. A. (2008). A hemispherical electronic eye camera based on compressible silicon optoelectronics. Nature, 454(7205), 748-753.

88 Murphy, M. P., Kim, S., & Sitti, M. (2009). Enhanced adhesion by gecko-inspired hierarchical fibrillar adhesives. ACS applied materials & interfaces,1(4), 849-855.

89 Zamarreno, C. R., Matias, I. R., & Arregui, F. J. (2012). Nanofabrication techniques applied to the development of novel optical fiber sensors based on nanostructured coatings. IEEE Sensors Journal, 12(8), 2699-2710.

90 Consales, M., Ricciardi, A., Crescitelli, A., Esposito, E., Cutolo, A., & Cusano, A. (2012). Lab-on-fiber technology: toward multifunctional optical nanoprobes. ACS nano, 6(4), 3163-3170.

91 Han, A., Kuan, A., Golovchenko, J., & Branton, D. (2012). Nanopatterning on nonplanar and fragile substrates with ice resists. Nano letters, 12(2), 1018-1021.

92 Johnson, T. W., Lapin, Z. J., Beams, R., Lindquist, N. C., Rodrigo, S. G., Novotny, L., & Oh, S. H. (2012). Highly reproducible near-field optical imaging with sub-20-nm resolution based on template-stripped gold pyramids. ACS nano, 6(10), 9168-9174.

93 Lindquist, N. C., Nagpal, P., Lesuffleur, A., Norris, D. J., & Oh, S. H. (2010). Three-dimensional plasmonic nanofocusing. Nano letters, 10(4), 1369-1373.

94 Treutlein, P., Hunger, D., Camerer, S., Hänsch, T. W., & Reichel, J. (2007). Bose-Einstein condensate coupled to a nanomechanical resonator on an atom chip. Physical Review Letters, 99(14), 140403.

95 Bleszynski-Jayich, A. C., Shanks, W. E., Peaudecerf, B., Ginossar, E., Von Oppen, F., Glazman, L., & Harris, J. G. E. (2009). Persistent currents in normal metal rings. Science, 326(5950), 272-275.

96 Tseng, S. C., Peng, W. Y., Hsieh, Y. F., Lee, P. J., & Lai, W. L. (2010). Electron beam lithography on cylindrical roller. Microelectronic Engineering, 87(5), 943-946.

97 Ahn, S. H., & Guo, L. J. (2008). High-speed roll-to-roll nanoimprint lithography on flexible plastic substrates. Advanced materials, 20(11), 2044-2049.

98 Li, Z., Gu, Y., Wang, L., Ge, H., Wu, W., Xia, Q., ... & Williams, R. S. (2009). Hybrid nanoimprint− soft lithography with sub-15 nm resolution. Nano letters, 9(6), 2306-2310.

99 Linden, J., Thanner, C., Schaaf, B., Wolff, S., Lägel, B., & Oesterschulze, E. (2011). Spray coating of PMMA for pattern transfer via electron beam lithography on surfaces with high topography. Microelectronic Engineering, 88(8), 2030-2032.

100 Yamazaki, K., & Yamaguchi, H. (2012). Electron beam lithography on vertical side faces of micrometer-order Si block. Journal of Vacuum Science & Technology B, 30(4), 041601.

101 Peterson, I. R. (1983). Langmuir-Blodgett electron-beam resists. IEE Proceedings I-Solid-State and Electron Devices, 130(5), 252-255.

102 Carr, D. W., Lercel, M. J., Whelan, C. S., Craighead, H. G., Seshadri, K., & Allara, D. L. (1997). High-selectivity pattern transfer processes for self-assembled monolayer electron beam resists. Journal of Vacuum Science & Technology A, 15(3), 1446-1450.

103 Gölzhäuser, A., Geyer, W., Stadler, V., Eck, W., Grunze, M., Edinger, K., ... & Hinze, P. (2000). Nanoscale patterning of self-assembled monolayers with electrons. Journal of Vacuum Science & Technology B, 18(6), 3414-3418.

104 Pedersen, R. H., Hamzah, M., Thoms, S., Roach, P., Alexander, M. R., & Gadegaard, N. (2010). Electron beam lithography using plasma polymerized hexane as resist. Microelectronic Engineering, 87(5), 1112-1114.

105 Kelkar, P. S., Beauvais, J., Lavallee, E., Drouin, D., Cloutier, M., Turcotte, D., ... & Aimez, V. (2004). Nano patterning on optical fiber and laser diode facet with dry resist. Journal of Vacuum Science & Technology A, 22(3), 743-746.

106 Lavallée, E., Beauvais, J., Drouin, D., Kelkar, P., Yang, P., Turcotte, D., Cloutier, M., Legario, R. (2003). Evaporated Electron Beam Lithography Resist for Non-Planar Surfaces. In Microprocesses and Nanotechnology Conference. Digest of Papers. pp 152-153.

107 Awad, Y., Lavallée, E., Lau, K. M., Beauvais, J., Drouin, D., Cloutier, M., ... & Kelkar, P. (2004). Arrays of holes fabricated by electron-beam lithography combined with image reversal process using nickel pulse reversal plating.Journal of Vacuum Science & Technology A, 22(3), 1040-1043.

108 King, G. M., Schürmann, G., Branton, D., & Golovchenko, J. A. (2005). Nanometer patterning with ice. Nano letters, 5(6), 1157-1160.

109 Gardener, J. A., & Golovchenko, J. A. (2012). Ice-assisted electron beam lithography of graphene. Nanotechnology, 23(18), 185302.

110 Bahlke, M. E., Mendoza, H. A., Ashall, D. T., Yin, A. S., & Baldo, M. A. (2012). Dry lithography of large-area, thin-film organic semiconductors using frozen CO2 resists. Advanced Materials, 24(46), 6136-6140.

111 Pennelli, G., Totaro, M., & Piotto, M. (2012). Selective doping of silicon nanowires by means of electron beam stimulated oxide etching. Nano letters,12(2), 1096-1101.

112 Ma, S., Con, C., Yavuz, M., & Cui, B. (2011). Polystyrene negative resist for high-resolution electron beam lithography. Nanoscale research letters, 6(1), 1.

113 Con, C., Dey, R., Ferguson, M., Zhang, J., Mansour, R., Yavuz, M., & Cui, B. (2012). High molecular weight polystyrene as very sensitive electron beam resist. Microelectronic Engineering, 98, 254-257.

114 Con, C., Arwa, S. A., Yavuz, M., & Cui, B. (2013). Dry thermal development of negative electron beam resist polystyrene. Adv. Nano Res, 1, 105-109.

115 Gerbedoen, J. C., Aliane, A., Giguère, A., Drouin, D., Ares, R., & Aimez, V. (2013). All evaporation submicron lift-off lithography process with negative e-beam QSR-5 resist. Microelectronic Engineering, 103, 123-125.

116 Beyler, C. L., & Hirschler, M. M. (2002). Thermal decomposition of polymers. SFPE handbook of fire protection engineering, 2, 110-131.

117 Dey, R. K., & Cui, B. (2013). Effect of molecular weight distribution on e-beam exposure properties of polystyrene. Nanotechnology, 24(24), 245302.

118 Abbas, A. S., Yavuz, M., & Cui, B. (2014). Polycarbonate electron beam resist using solvent developer. Microelectronic Engineering, 113, 140-142.

119 Kashyap, R. (1999). Fiber bragg gratings. Academic press. pp 15-16.

120 Xu, Q., Bao, J., Rioux, R. M., Perez-Castillejos, R., Capasso, F., & Whitesides, G. M. (2007). Fabrication of large-area patterned nanostructures for optical applications by nanoskiving. Nano letters, 7(9), 2800-2805.

121 Paul, K. E., Zhu, C., Love, J. C., & Whitesides, G. M. (2001). Fabrication of mid-infrared frequency-selective surfaces by soft lithography. Applied optics,40(25), 4557-4561.

122 Kneipp, K., Kneipp, H., Itzkan, I., Dasari, R. R., & Feld, M. S. (2002). Surface-enhanced Raman scattering and biophysics. Journal of Physics: Condensed Matter, 14(18), R597.

123 Muskens, O. L., Diedenhofen, S. L., Kaas, B. C., Algra, R. E., Bakkers, E. P., Gómez Rivas, J., & Lagendijk, A. (2009). Large photonic strength of highly tunable resonant nanowire materials. Nano letters, 9(3), 930-934.

124 Kang, S., Joe, H. E., Kim, J., Jeong, Y., Min, B. K., & Oh, K. (2011). Subwavelength plasmonic lens patterned on a composite optical fiber facet for quasi-one-dimensional Bessel beam generation. Applied Physics Letters, 98(24), 241103.

125 Liu, Y., Xu, H., Stief, F., Zhitenev, N., & Yu, M. (2011). Far-field superfocusing with an optical fiber based surface plasmonic lens made of nanoscale concentric annular slits. Optics express, 19(21), 20233-20243.

126 Wang, H., Zhou, W., Cui, Y., Wang, G., & Shum, P. P. (2013). Focused ion beam nanoscale patterned transmission-enhanced fiber-optic tips. Journal of nanoscience and nanotechnology, 13(7), 4581-4586.

127 Jia, P., Jiang, H., Sabarinathan, J., & Yang, J. (2013). Plasmonic nanohole array sensors fabricated by template transfer with improved optical performance. Nanotechnology, 24(19), 195501.

128 Zhang, J., Shokouhi, B., & Cui, B. (2012). Tilted nanostructure fabrication by electron beam lithography. Journal of Vacuum Science & Technology B, 30(6), 06F302.

129 Dey, R. K., & Cui, B. (2014). Electron beam lithography with feedback using in situ self-developed resist. Nanoscale research letters, 9(1), 1.

130 Burek, M. J., de Leon, N. P., Shields, B. J., Hausmann, B. J., Chu, Y., Quan, Q., ... & Lončar, M. (2012). Free-standing mechanical and photonic nanostructures in single-crystal diamond. Nano letters, 12(12), 6084-6089.

131 Takahashi, S., Suzuki, K., Okano, M., Imada, M., Nakamori, T., Ota, Y., ... & Noda, S. (2009). Direct creation of three-dimensional photonic crystals by a top-down approach. Nature materials, 8(9), 721-725.

132 Yamazaki, K., & Yamaguchi, H. (2008). Flexible Nanofabrication in Three-Dimensional Electron-Beam Lithography Enhanced by Suppression of Proximity Effect. Applied physics express, 1(9), 097001.

133 Khorasaninejad, M., Walia, J., & Saini, S. S. (2012). Enhanced first-order Raman scattering from arrays of vertical silicon nanowires. Nanotechnology, 23(27), 275706.

134 Morton, K. J., Nieberg, G., Bai, S., & Chou, S. Y. (2008). Wafer-scale patterning of sub-40 nm diameter and high aspect ratio (>50:1) silicon pillar arrays by nanoimprint and etching. Nanotechnology, 19(34), 345301.

135 Henry, M. D., Walavalkar, S., Homyk, A., & Scherer, A. (2009). Alumina etch masks for fabrication of high-aspect-ratio silicon micropillars and nanopillars. Nanotechnology, 20(25), 255305.

136 Wu, B., Kumar, A., & Pamarthy, S. (2010). High aspect ratio silicon etch: a review. Journal of applied physics, 108(5), 051101.

137 Mirza, M. M., Zhou, H., Velha, P., Li, X., Docherty, K. E., Samarelli, A., ... & Paul, D. J. (2012). Nanofabrication of high aspect ratio (~50:1) sub-10 nm silicon nanowires using inductively coupled plasma etching. Journal of Vacuum Science & Technology B, 30(6), 06FF02.

138 Mao, P., & Han, J. (2009). Massively-parallel ultra-high-aspect-ratio nanochannels as mesoporous membranes. Lab on a Chip, 9(4), 586-591.

139 Con, C., Zhang, J., & Cui, B. (2014). Nanofabrication of high aspect ratio structures using an evaporated resist containing metal. Nanotechnology, 25(17), 175301.

140 Bilenberg, B., Schøler, M., Shi, P., Schmidt, M. S., Bøggild, P., Fink, M., ... & Kristensen, A. (2006). Comparison of high resolution negative electron beam resists. Journal of Vacuum Science & Technology B, 24(4), 1776-1779.

141 Muray, A., Scheinfein, M., Isaacson, M., & Adesida, I. (1985). Radiolysis and resolution limits of inorganic halide resists. Journal of Vacuum Science & Technology B, 3(1), 367-372.

142 Kratschmer, E., & Isaacson, M. (1986). Nanostructure fabrication in metals, insulators, and semiconductors using self-developing metal inorganic resist.Journal of Vacuum Science & Technology B, 4(1), 361-364.

143 Ramanathan, M., & Darling, S. B. (2013). Nanofabrication with metallopolymers-recent developments and future perspectives. Polymer International, 62(8), 1123-1134.

144 Abbas, A. S., Alqarni, S., Shokouhi, B. B., Yavuz, M., & Cui, B. (2014). Water soluble and metal-containing electron beam resist poly (sodium 4-styrenesulfonate). Materials Research Express, 1(4), 045102.

145 Grenci, G., Della Giustina, G., Pozzato, A., Brusatin, G., & Tormen, M. (2011). Boehmite filled hybrid sol–gel system as directly writable hard etching mask for pattern transfer. Microelectronic Engineering, 88(8), 1964-1967.

146 Grenci, G., Della Giustina, G., Pozzato, A., Zanchetta, E., Tormen, M., & Brusatin, G. (2012). Negative hybrid sol–gel resist as hard etching mask for pattern transfer with dry etching. Microelectronic Engineering, 98, 134-137.

147 Tseng, Y. C., Peng, Q., Ocola, L. E., Czaplewski, D. A., Elam, J. W., & Darling, S. B. (2011). Etch properties of resists modified by sequential infiltration synthesis. Journal of Vacuum Science & Technology B, 29(6), 06FG01.

148 Tseng, Y. C., Peng, Q., Ocola, L. E., Elam, J. W., & Darling, S. B. (2011). Enhanced block copolymer lithography using sequential infiltration synthesis. The Journal of Physical Chemistry C, 115(36), 17725-17729.

149 Tseng, Y. C., Mane, A. U., Elam, J. W., & Darling, S. B. (2012). Enhanced lithographic imaging layer meets semiconductor manufacturing specification a decade early. Advanced Materials, 24(19), 2608-2613.

150 Peng, Q., Tseng, Y. C., Darling, S. B., & Elam, J. W. (2011). A route to nanoscopic materials via sequential infiltration synthesis on block copolymer templates. Acs Nano, 5(6), 4600-4606.

151 Yeo, B. S., Stadler, J., Schmid, T., Zenobi, R., & Zhang, W. (2009). Tip-enhanced Raman Spectroscopy–Its status, challenges and future directions.Chemical Physics Letters, 472(1), 1-13.

152 Ku, H. Y., & Scala, L. C. (1969). Polymeric electron beam resists. Journal of The Electrochemical Society, 116(7), 980-985.

153 Liu, Y., Meng, C., Zhang, A. P., Xiao, Y., Yu, H., & Tong, L. (2011). Compact microfiber Bragg gratings with high-index contrast. Optics letters, 36(16), 3115-3117.

154 Kontziampasis, D., Boulousis, G., Smyrnakis, A., Ellinas, K., Tserepi, A., & Gogolides, E. (2014). Biomimetic, antireflective, superhydrophobic and oleophobic PMMA and PMMA-coated glass surfaces fabricated by plasma processing. Microelectronic Engineering, 121, 33-38.

155 Stratakis, E., Ranella, A., & Fotakis, C. (2011). Biomimetic micro/nanostructured functional surfaces for microfluidic and tissue engineering applications. Biomicrofluidics, 5(1), 013411.

156 Tawfick, S., De Volder, M., Copic, D., Park, S. J., Oliver, C. R., Polsen, E. S., ... & Hart, A. J. (2012). Engineering of Micro-and Nanostructured Surfaces with Anisotropic Geometries and Properties. Advanced Materials, 24(13), 1628-1674.

157 Manabe, K., Nishizawa, S., Kyung, K. H., & Shiratori, S. (2014). Optical phenomena and antifrosting property on biomimetics slippery fluid-infused antireflective films via layer-by-layer comparison with superhydrophobic and antireflective films. ACS applied materials & interfaces, 6(16), 13985-13993.

158 Taguchi, T., Hayashi, H., Fujii, A., Tsuda, K., Yamada, N., Minoura, K., ... & Itoh, Y. (2010, May). 80.3: Distinguished Paper: Ultra-Low-Reflective 60-in. LCD with Uniform Moth-Eye Surface for Digital Signage. In SID Symposium Digest of Technical Papers (Vol. 41, No. 1, pp. 1196-1199). Blackwell Publishing Ltd.

159 Checco, A., Rahman, A., & Black, C. T. (2014). Robust Superhydrophobicity in Large-Area Nanostructured Surfaces Defined by Block-Copolymer Self Assembly. Advanced Materials, 26(6), 886-891.

160 Nosonovsky, M., & Bhushan, B. (2009). Superhydrophobic surfaces and emerging applications: non-adhesion, energy, green engineering. Current Opinion in Colloid & Interface Science, 14(4), 270-280.

161 Kim, T. I., Jeong, H. E., Suh, K. Y., & Lee, H. H. (2009). Stooped Nanohairs: Geometry-Controllable, Unidirectional, Reversible, and Robust Gecko-like Dry Adhesive. Advanced Materials, 21(22), 2276-2281.

162 Murphy, M. P., Aksak, B., & Sitti, M. (2009). Gecko-Inspired Directional and Controllable Adhesion. Small, 5(2), 170-175.

163 Jeong, H. E., & Suh, K. Y. (2009). Nanohairs and nanotubes: efficient structural elements for gecko-inspired artificial dry adhesives. Nano Today, 4(4), 335-346.

164 Kim, S., Spenko, M., Trujillo, S., Heyneman, B., Santos, D., & Cutkosky, M. R. (2008). Smooth vertical surface climbing with directional adhesion. IEEE Transactions on robotics, 24(1), 65-74.

165 Autumn, K., Liang, Y. A., Hsieh, S. T., Zesch, W., Chan, W. P., Kenny, T. W., ... & Full, R. J. (2000). Adhesive force of a single gecko foot-hair. Nature, 405(6787), 681-685.

166 Parness, A., Soto, D., Esparza, N., Gravish, N., Wilkinson, M., Autumn, K., & Cutkosky, M. (2009). A microfabricated wedge-shaped adhesive array displaying gecko-like dynamic adhesion, directionality and long lifetime. Journal of the Royal Society Interface, 6(41), 1223-1232.

167 Huber, G., Mantz, H., Spolenak, R., Mecke, K., Jacobs, K., Gorb, S. N., & Arzt, E. (2005). Evidence for capillarity contributions to gecko adhesion from single spatula nanomechanical measurements. Proceedings of the National Academy of Sciences of the United States of America, 102(45), 16293-16296.

168 Yao, H., & Gao, H. (2006). Mechanics of robust and releasable adhesion in biology: Bottom–up designed hierarchical structures of gecko. Journal of the Mechanics and Physics of Solids, 54(6), 1120-1146.

169 RAUT, H. K. (2014). Studies on nanostructured anti-reflective coatings (Doctoral dissertation, National University of Singapore).

170 Wilson, S. J., & Hutley, M. C. (1982). The optical properties of 'moth eye' antireflection surfaces. Journal of Modern Optics, 29(7), 993-1009.

171 Huang, Y. F., Chattopadhyay, S., Jen, Y. J., Peng, C. Y., Liu, T. A., Hsu, Y. K., ... & Lee, C. S. (2007). Improved broadband and quasi-omnidirectional anti-reflection properties with biomimetic silicon nanostructures. Nature nanotechnology, 2(12), 770-774.

172 Dobrowolski, J. A., Poitras, D., Ma, P., Vakil, H., & Acree, M. (2002). Toward perfect antireflection coatings: numerical investigation. Applied optics, 41(16), 3075-3083.

173 Poitras, D., & Dobrowolski, J. A. (2004). Toward perfect antireflection coatings. 2. Theory. Applied optics, 43(6), 1286-1295.

174 Kanamori, Y., Ishimori, M., & Hane, K. (2002). High efficient light-emitting diodes with antireflection subwavelength gratings. IEEE Photonics Technology Letters, 14(8), 1064-1066.

175 Kanamori, Y., Hane, K., Sai, H., & Yugami, H. (2001). 100 nm period silicon antireflection structures fabricated using a porous alumina membrane mask. Applied Physics Letters, 78(2), 142-143.

176 Ha, J. M., Yoo, S. H., Cho, J. H., Cho, Y. H., & Cho, S. O. (2014). Enhancement of antireflection property of silicon using nanostructured surface combined with a polymer deposition. Nanoscale research letters, 9(9), 1-7.

177 Kim, J. B., Yeo, C. I., Lee, Y. H., Ravindran, S., & Lee, Y. T. (2014). Broadband antireflective silicon nanostructures produced by spin-coated Ag nanoparticles. Nanoscale research letters, 9(1), 1-7.

178 Leung, S. F., Zhang, Q., Xiu, F., Yu, D., Ho, J. C., Li, D., & Fan, Z. (2014). Light management with nanostructures for optoelectronic devices. The journal of physical chemistry letters, 5(8), 1479-1495.

179 Lin, Y. R., Lai, K. Y., Wang, H. P., & He, J. H. (2010). Slope-tunable Si nanorod arrays with enhanced antireflection and self-cleaning properties. Nanoscale, 2(12), 2765-2768.

180 Kislyuk, V. V., & Dimitriev, O. P. (2008). Nanorods and nanotubes for solar cells. Journal of nanoscience and nanotechnology, 8(1), 131-148.

181 Gao, Y., Shi, T., Tan, X., & Liao, G. (2014). A Novel Method to Fabricate Silicon Tubular Gratings with Broadband Antireflection and Super-Hydrophobicity. Journal of nanoscience and nanotechnology, 14(6), 4469-4474.

182 Li, X. (2012). Metal assisted chemical etching for high aspect ratio nanostructures: a review of characteristics and applications in photovoltaics. Current Opinion in Solid State and Materials Science, 16(2), 71-81.

183 Theunissen, M. J. J., Appels, J. A., & Verkuylen, W. H. C. G. (1970). Application of preferential electrochemical etching of silicon to semiconductor device technology. Journal of The Electrochemical Society, 117(7), 959-965.

184 Theiß, W. (1997). Optical properties of porous silicon. Surface Science Reports, 29(3), 91-192.

185 Menna, P., Di Francia, G., & La Ferrara, V. (1995). Porous silicon in solar cells: a review and a description of its application as an AR coating. Solar Energy Materials and Solar Cells, 37(1), 13-24.

186 King, D. L., & Buck, M. E. (1991, October). Experimental optimization of an anisotropic etching process for random texturization of silicon solar cells. In *Photovoltaic Specialists Conference*. Conference Record of the Twenty Second IEEE (pp. 303-308). IEEE.

187 Vazsonyi, E., De Clercq, K., Einhaus, R., Van Kerschaver, E., Said, K., Poortmans, J., ... & Nijs, J. (1999). Improved anisotropic etching process for industrial texturing of silicon solar cells. Solar energy materials and solar cells, 57(2), 179-188.

188 Rykaczewski, K., Hildreth, O. J., Wong, C. P., Fedorov, A. G., & Scott, J. H. J. (2011). Guided three-dimensional catalyst folding during metal-assisted chemical etching of silicon. Nano letters, 11(6), 2369-2374.

189 Yeo, C. I., Song, Y. M., Jang, S. J., & Lee, Y. T. (2011). Wafer-scale broadband antireflective silicon fabricated by metal-assisted chemical etching using spin-coating Ag ink. Optics express, 19(105), A1109-A1116.

190 Tsujino, K., Matsumura, M., & Nishimoto, Y. (2006). Texturization of multicrystalline silicon wafers for solar cells by chemical treatment using metallic catalyst. Solar energy materials and solar cells, 90(1), 100-110.

191 Mehran, M., Mohajerzadeh, S., Sanaee, Z., & Abdi, Y. (2010). Nanograss and nanostructure formation on silicon using a modified deep reactive ion etching. Applied Physics Letters, 96(20), 203101.

192 Gharghi, M., & Sivoththaman, S. (2006). Formation of nanoscale columnar structures in silicon by a maskless reactive ion etching process. Journal of Vacuum Science & Technology A, 24(3), 723-727.

193 Gogolides, E., Constantoudis, V., Kokkoris, G., Kontziampasis, D., Tsougeni, K., Boulousis, G., ... & Tserepi, A. (2011). Controlling roughness: from etching to nanotexturing and plasma-directed organization on organic and inorganic materials. Journal of Physics D: Applied Physics, 44(17), 174021.

194 Wang, S., Yu, X. Z., & Fan, H. T. (2007). Simple lithographic approach for subwavelength structure antireflection. Applied Physics Letters, 91(6), 061105.

195 Lin, G. R., Chang, Y. C., Liu, E. S., Kuo, H. C., & Lin, H. S. (2007). Low refractive index Si nanopillars on Si substrate. Applied physics letters, 90(18), 181923.

196 Scriven, L. E. (1988). Physics and applications of dip coating and spin coating. In MRS proceedings (Vol. 121, p. 717). Cambridge University Press.

197 Bornside, D. E., Macosko, C. W., and Scriven, L. E. (1987). Modeling of Spin Coating. Journal of Imaging Technology. 13, 122.

198 Walheim, S., Schäffer, E., Mlynek, J., & Steiner, U. (1999). Nanophase-separated polymer films as high-performance antireflection coatings. Science, 283(5401), 520-522.

199 Leem, J. W., Chung, K. S., & Yu, J. S. (2012). Antireflective properties of disordered Si SWSs with hydrophobic surface by thermally dewetted Pt nanomask patterns for Si-based solar cells. Current Applied Physics, 12(1), 291-298.

200 Nagel, H., Aberle, A. G., & Hezel, R. (1999). Optimised antireflection coatings for planar silicon solar cells using remote PECVD silicon nitride and porous silicon dioxide. Progress in Photovoltaics: Research and Applications, 7(4), 245-260.

201 Park, C., Yoon, J., & Thomas, E. L. (2003). Enabling nanotechnology with self assembled block copolymer patterns. Polymer, 44(22), 6725-6760.

202 Robbie, K., & Brett, M. J. (1997). Sculptured thin films and glancing angle deposition: Growth mechanics and applications. Journal of Vacuum Science & Technology A, 15(3), 1460-1465.

203 Michalcik, Z., Horakova, M., Spatenka, P., Klementova, S., Zlamal, M., & Martin, N. (2012). Photocatalytic activity of nanostructured titanium dioxide thin films. International Journal of Photoenergy, 2012.

204 Min, W. L., Betancourt, A. P., Jiang, P., & Jiang, B. (2008). Bioinspired broadband antireflection coatings on GaSb. Applied Physics Letters, 92(14), 141109.

205 Yu, B., Sun, P., Chen, T., Jin, Q., Ding, D., Li, B., & Shi, A. C. (2006). Confinement-induced novel morphologies of block copolymers. Physical review letters, 96(13), 138306.

206 Syu, H. J., Shiu, S. C., & Lin, C. F. (2012). Silicon nanowire/organic hybrid solar cell with efficiency of 8.40%. Solar energy materials and solar cells, 98, 267-272.

207 Askar, K., Phillips, B. M., Fang, Y., Choi, B., Gozubenli, N., Jiang, P., & Jiang, B. (2013). Self-assembled self-cleaning broadband anti-reflection coatings. Colloids and Surfaces A: Physicochemical and Engineering Aspects, 439, 84-100.

208 Nakanishi, T., Hiraoka, T., Fujimoto, A., Saito, S., & Asakawa, K. (2006). Nano-patterning using an embedded particle monolayer as an etch mask. Microelectronic engineering, 83(4), 1503-1508.

209 Chen, H. L., Chuang, S. Y., Lin, C. H., & Lin, Y. H. (2007). Using colloidal lithography to fabricate and optimize sub-wavelength pyramidal and honeycomb structures in solar cells. Optics Express, 15(22), 14793-14803.

210 Sun, C. H., Jiang, P., & Jiang, B. (2008). Broadband moth-eye antireflection coatings on silicon. Applied Physics Letters, 92(6), 061112.

211 Li, Y., Zhang, J., Zhu, S., Dong, H., Jia, F., Wang, Z., ... & Xu, W. (2009). Biomimetic surfaces for high-performance optics. Advanced Materials,21(46), 4731-4734.

212 Pearton, S. J., & Norton, D. P. (2005). Dry etching of electronic oxides, polymers, and semiconductors. Plasma Processes and Polymers, 2(1), 16-37.

213 Li, Y., Zhang, J., & Yang, B. (2010). Antireflective surfaces based on biomimetic nanopillared arrays. Nano Today, 5(2), 117-127.

214 De Gennes, P. G., Brochard-Wyart, F., & Quéré, D. (2013). Capillarity and wetting phenomena: drops, bubbles, pearls, waves. Springer Science & Business Media.

215 Thiruvengadathan, R., Korampally, V., Ghosh, A., Chanda, N., Gangopadhyay, K., & Gangopadhyay, S. (2013). Nanomaterial processing using self-assembly-bottom-up chemical and biological approaches. Reports on Progress in Physics, 76(6), 066501.

216 Park, M., Harrison, C., Chaikin, P. M., Register, R. A., & Adamson, D. H. (1997). Block copolymer lithography: periodic arrays of~ 1011 holes in 1 square centimeter. Science, 276(5317), 1401-1404.

217 Bates, F. (1991). Polymer-polymer phase behavior. Science, 251(4996), 898-905.

218 Hamley, I. W. (1998). The physics of block copolymers (Vol. 19). New York: Oxford University Press.

219 Deng, T., Chen, C., Honeker, C., & Thomas, E. L. (2003). Two-dimensional block copolymer photonic crystals. Polymer, 44(21), 6549-6553.

220 Purwaningsih, L. (2011). Fabrication of nano-structured materials and their applications (No. RWTH-CONV-125494). Lehrstuhl für Textilchemie und Makromolekulare Chemie.

221 Gao, Z., & Eisenberg, A. (1993). A model of micellization for block copolymers in solutions. Macromolecules, 26(26), 7353-7360.

222 Gohy, J. F. (2005). Block copolymer micelles. In Block copolymers II (pp. 65-136). Springer Berlin Heidelberg.

223 Kästle, G., Boyen, H. G., Weigl, F., Lengl, G., Herzog, T., Ziemann, P., ... & Möller, M. (2003). Micellar nanoreactors—Preparation and characterization of hexagonally ordered arrays of metallic nanodots. Advanced Functional Materials, 13(11), 853-861.

224 Lohmueller, T., Bock, E., & Spatz, J. P. (2008). Synthesis of Quasi-Hexagonal Ordered Arrays of Metallic Nanoparticles with Tuneable Particle Size. Advanced Materials, 20(12), 2297-2302.

225 Lohmueller, T., Brunner, R., & Spatz, J. P. (2010). Improved properties of optical surfaces by following the example of the Moth eye. Biomimetics Learning From Nature.

226 Con, C., Aydinoglu, F., & Cui, B. (2015). High resolution nanofabrication using self-assembly of metal salt-polymer nanocomposite film. Journal of Vacuum Science & Technology B, 33(6), 06F304.

227 Kontziampasis, D., Boulousis, G., Smyrnakis, A., Ellinas, K., Tserepi, A., & Gogolides, E. (2014). Biomimetic, antireflective, superhydrophobic and oleophobic PMMA and PMMA-coated glass surfaces fabricated by plasma processing. Microelectronic Engineering, 121, 33-38.

228 Hulteen, J. C., & Van Duyne, R. P. (1995). Nanosphere lithography: a materials general fabrication process for periodic particle array surfaces. Journal of Vacuum Science & Technology A, 13(3), 1553-1558.

229 Jansen, H. V., De Boer, M. J., Unnikrishnan, S., Louwerse, M. C., & Elwenspoek, M. C. (2009). Black silicon method X: a review on high speed and selective plasma etching of silicon with profile control: an in-depth comparison between Bosch and cryostat DRIE processes as a roadmap to next generation equipment. Journal of Micromechanics and Microengineering, 19(3), 033001.

230 Kontziampasis, D., Constantoudis, V., & Gogolides, E. (2012). Plasma directed organization of nanodots on polymers: effects of polymer type and etching time on morphology and order. Plasma Processes and Polymers, 9(9), 866-872.

231 Vourdas, N., Kontziampasis, D., Kokkoris, G., Constantoudis, V., Goodyear, A., Tserepi, A., ... & Gogolides, E. (2010). Plasma directed assembly and organization: bottom-up nanopatterning using top-down technology. Nanotechnology, 21(8), 085302.

232 Liu, W., Ferguson, M., Yavuz, M., & Cui, B. (2012). Porous TEM windows fabrication using CsCl self-assembly. Journal of Vacuum Science & Technology B, 30(6), 06F201.

233 Con C, and Cui B. (May 2015). Ultra high resolution nanofabrication using self assembly of salt-polymer nanocomposite film. Poster presented at 59th EIPBN, San Diego, CA, USA.

234 Thomasson, P., Tyagi, O. S., & Knözinger, H. (1999). Characterization of the basicity of modified MgO-catalysts. Applied Catalysis A: General, 181(1), 181-188.

235 Ruckenstein, E., & Hu, Y. H. (1999). Methane partial oxidation over NiO/MgO solid solution catalysts. Applied Catalysis A: General, 183(1), 85-92.

236 Janković, B., Mentus, S., & Jelić, D. (2009). A kinetic study of non-isothermal decomposition process of anhydrous nickel nitrate under air atmosphere. Physica B: Condensed Matter, 404(16), 2263-2269.

237 Brockner, W., Ehrhardt, C., & Gjikaj, M. (2007). Thermal decomposition of nickel nitrate hexahydrate, Ni (NO 3) 2· 6H 2 O, in comparison to Co (NO 3) 2· 6H 2 O and Ca (NO 3) 2· 4H 2 O. Thermochimica Acta, 456(1), 64-68.

238 Gadalla, A. M., & Yu, H. F. (1991). Thermal behaviour of Ni (II) nitrate hydrate and its aerosols. Journal of Thermal Analysis and Calorimetry, 37(2), 319-331.

239 Elmasry, M. A. A., Gaber, A., & Khater, E. M. H. (1998). Thermal decomposition of Ni (II) and Fe (III) nitrates and their mixture. Journal of thermal analysis and calorimetry, 52(2), 489-495.

240 Estellé, J., Salagre, P., Cesteros, Y., Serra, M., Medina, F., & Sueiras, J. E. (2003). Comparative study of the morphology and surface properties of nickel oxide prepared from different precursors. Solid State Ionics, 156(1), 233-243.

241 Balazs, A. C., Emrick, T., & Russell, T. P. (2006). Nanoparticle polymer composites: where two small worlds meet. Science, 314(5802), 1107-1110.

242 Tang, E., Cheng, G., & Ma, X. (2006). Preparation of nano-ZnO/PMMA composite particles via grafting of the copolymer onto the surface of zinc oxide nanoparticles. Powder Technology, 161(3), 209-214.

243 Saffih, F., Con, C., Alshammari, A., Yavuz, M., & Cui, B. (2014). Fabrication of silicon nanostructures with large taper angle by reactive ion etching. Journal of Vacuum Science & Technology B, 32(6), 06FI04.